NATIONAL ACADEMY OF SCIENCES OF UKRAINE ● G. V. KURDYUMOV INSTITUTE FOR METAL PHYSICS

AN INTERNATIONAL RESEARCH JOURNAL

METALLOPHYSICS AND ADVANCED TECHNOLOGIES

(Metallofizika i Noveishie Tekhnologii)

FOUNDED IN SEPTEMBER, 1979

Volume 47, No. 1; January 2025

CONTENTS

CONTENTS, No. 1 (Vol. 47)

Scientific Editors of Issue—*O. S. Gatsenko, V. A. Tatarenko*
Executive Managing Editor—*O. S. Gatsenko*
Editors—*L. I. Makarenko, M. V. Manilo, I. V. Zagorulko*
The artwork for direct reproduction is made by computer group of EPD of the G. V. Kurdyumov Institute for Metal Physics, N.A.S. of Ukraine

Editorial Office Address:
G. V. Kurdyumov Institute for Metal Physics, N.A.S. of Ukraine, EPD—'MNT',
36 Academician Vernadsky Boulevard, UA-03142 Kyiv, Ukraine
Telephone: +380 44 4249042. Fax: +380 44 4242561. E-mail: mfint@imp.kiev.ua
Media Identifier R30-03171

Approved for publication by the Academic Council of the G. V. Kurdyumov Institute for Metal Physics of the National Academy of Sciences of Ukraine
Published in English or Ukrainian languages according to resolution of Editorial Board of the journal

Printed by Publishing House 'Akademperiodyka', of the NAS of Ukraine
4 Tereshchenkivs'ka Str., UA-01024 Kyiv, Ukraine
Registration Certificate of Publishing Subject: ДК № 544 on 27.07.2001

Journal website: http://mfint.imp.kiev.ua
Journal DOI: https://doi.org/10.15407/mfint

Issue DOI: https://doi.org/10.15407/mfint.47.01

НАЦІОНАЛЬНА АКАДЕМІЯ НАУК УКРАЇНИ ● ІНСТИТУТ МЕТАЛОФІЗИКИ ім. Г. В. Курдюмова

МЕТАЛОФІЗИКА ТА НОВІТНІ ТЕХНОЛОГІЇ

МІЖНАРОДНИЙ НАУКОВИЙ ЖУРНАЛ
ЗАСНОВАНИЙ У ВЕРЕСНІ 1979 р.

Том 47, № 1; січень, 2025

ЗМІСТ

Наукові редактори випуску: *О. С. Гаценко, В. А. Татаренко*
Відповідальний секретар редакційної колегії *О. С. Гаценко*
Редактор-коректор *О. С. Гаценко*
Технічні редактори: *І. В. Загорулько, Л. І. Макаренко, М. В. Маніло*
Художні редактори: *І. В. Загорулько, Л. І. Макаренко, М. В. Маніло*
Оригінал-макет для прямого репродукування виготовлено комп'ютерною групою РВВ Інституту металофізики ім. Г. В. Курдюмова НАН України

Адреса редакції:
Інститут металофізики ім. Г. В. Курдюмова НАН України, РВВ—Редакція «МНТ»
бульв. Акад. Вернадського, 36; 03142 Київ, Україна
Тел.: +380 44 4249042; факс: +380 44 4242561
Ел. пошта: mfint@imp.kiev.ua
Ідентифікатор медіа R30-03171

Затверджено до друку вченою радою Інституту металофізики ім. Г. В. Курдюмова НАН України
Друкується за постановою редакційної колегії журналу англійською або українською мовами

Підписано до друку 30.01.2025 р. Формат 70 × 100/16.
Ум. друк. арк. 10,64. Обл.-вид. арк. 9,79.
Тираж 54 пр. Зам. № 7578 від 13.02.2025 р.

Віддруковано ВД «Академперіодика» НАН України
вул. Терещенківська, 4; 01024 Київ, Україна
Свідоцтво суб'єкта видавничої справи ДК № 544 від 27.07.2001 р.

Сайт журналу: http://mfint.imp.kiev.ua
DOI (журналу): https://doi.org/10.15407/mfint
DOI (випуску): https://doi.org/10.15407/mfint.47.01

INFORMATION (GUIDELINES) FOR CONTRIBUTORS

Submission of Manuscripts: Manuscripts should be sent by e-mail (mfint@imp.kiev.ua). Additionally, they can be sent by regular mail to Executive Managing Editor, Editorial Office, G. V. Kurdyumov Institute for Metal Physics, N.A.S. of Ukraine, 36 Academician Vernadsky Boulevard, UA-03142 Kyiv, Ukraine. Manuscripts may also be submitted to a member of the Editorial Advisory Board or to the appropriate Regional Editor who is familiar with the research presented.
Submission of a paper to '*Metallophysics and Advanced Technologies*' (transliteration: '*Metallofizika i Noveishie Tekhnologii*', *i.e.*, '*MfNT*') will be taken to imply that it represents original work not previously published, that it is not being considered for publication elsewhere, and that, if accepted for publication, it will not be republished without the consent of the Editors and Publisher. It is a condition of acceptance by the Editor of a manuscript for publication that the Publishers acquire automatically the copyright in the manuscript throughout the world. Journal '*MfNT*' supports the generally accepted principles described in documents on publication ethics and unacceptable practices, which are presented on the journal website.
Scope of the Journal: *Electronic Structure and Properties, Crystal-Lattice Defects, Phase Transformations, Physics of Strength and Plasticity, Metallic Surfaces and Films, Structure and Properties of Nanoscale and Mesoscopic Materials, Amorphous and Liquid States, Interactions of Radiation and Particles with Condensed Matter, Materials in Extremal Conditions, Reactor and Aerospace Metals Science, Medical Metals Science, New Metallic Materials and Synthetic Metals, Metal-Containing Smart Materials, Physical and Technical Basis of Experiment and Diagnostics, Articles under Discussion*.
Language: The language of publication may be English (preferably) or Ukrainian.
Abstract: Each paper requires an abstract of 200–250 words summarizing the significant coverage and findings (the use of mathematical symbols and expressions in abstract is not recommended).
Keywords and PACS numbers: 5–7 keywords and PACS numbers reflecting the content of the contribution should be supplied (see 'Physics and Astronomy Classification Scheme 2010').
Manuscript Preparation: Papers should be formatted according to the template, which can be downloaded from the Journal's website. The length of **research papers** should not in general exceed 5000 words and 10 figures; **review articles** should not exceed 10000 words and 30 figures, including tables and diagrams. Authors are urged to arrange the subject matter clearly under headings such as: 1. Introduction, 2. Experimental/Theoretical Details, 3. Results, 4. Discussion, 5. Conclusion, References. Subsections should be identified with section and subsection numbers (such as 6.1. Second-Value Subheading).
References and Notes: Notes are indicated in the text by consecutive superior Arabic numbers (without parentheses). References should be numbered consecutively (in square brackets) throughout the text. The full list should be collected and typed at the end of the paper in numerical order. Listed references should be completed in all details including **DOI** (if available) but excluding article titles in journals. **All authors'** initials should precede their names. Examples of references preparation:

1. S. O. Firstov and T. G. Rogul, *Metallofiz. Noveishie Tekhnol.*, **44**, No. 1: 127 (2022) (in Ukrainian). https://doi.org/10.15407/mfint.44.01.0127
2. V. B. Tarelnyk, O. P. Gaponova, and Ye. V. Konoplianchenko, *Prog. Phys. Met.*, **23**, No. 1: 27 (2022). https://doi.org/10.15407/ufm.23.01.027
3. A. Meisel, G. Leonhardt, and R. Szargan, *Röntgenspektren und Chemische Bindung* [X-Ray Spectra and Chemical Bond] (Leipzig: Akademische Verlagsgesellschaft Geest & Portig K.-G.: 1977) (in German).
4. J. M. Ziman, *Printsipy Teorii Tverdogo Tela* [Principles of the Theory of Solids] (Moscow: Mir: 1974) (Russian translation).
5. M. A. Stucke, D. M. Dimiduk, and D. M. Hazzledine, *High Temperature Ordered Intermetallic Alloys. V* (Eds. I. Baker and R. Darolia) (Pittsburgh, PA, USA: MRS: 1993), p. 471.
6. *Handbook of Mathematical Functions with Formulas, Graphs and Mathematical Tables* (Eds. M. Abramowitz and I. A. Stegun), Nat'l Bureau of Standards. Appl. Math. Ser. Vol. **55** (Washington, D.C.: U.S. Govt. Printing Office: 1964).
7. B. B. Karpovych and O. B. Borovkoff, *Proc. of Symp. 'Micromaterials Engineering' (Dec. 25–31, 1999)* (Kyiv: RVV IMF: 2000), vol. **2**, p. 113 (in Russian).
8. A. E. Krug, *Abstr. Int. Conf. Phys. Phenomena (Dec. 25–31, 1991, Alushta)* (Kharkiv: 1991), p. 12.
9. T. M. Radchenko, *Vplyv Uporyadkuvannya Defektnoyi Struktury на Transportni Vlastyvosti Zmishanykh Krystaliv* [Influence of Ordering of the Defect Structure on Transport Properties of the Mixed Crystals] (Thesis of Disser. for the Degree of Dr. Phys.-Math. Sci.) (Kyiv: G. V. Kurdyumov Institute for Metal Physics, N.A.S.U.: 2015) (in Ukrainian). https://doi.org/10.13140/RG.2.2.35430.22089

10. E. M. Gololobov, V. B. Shipilo, N. I. Sedrenok, and A. I. Dudyak, *Sposob Polucheniya Karbonitridov Metallov* [Production Method of Metal Carbonitrides], Authors' Certificate 722341 SSSR (Publ. November 21, 1979) (in Russian).
11. V. G. Trubachev, K. V. Chuistov, V. N. Gorshkov, and A. E. Perekos, *Sposob Polucheniya Metallicheskikh Poroshkov* [The Technology of Metallic Powder Production]: Patent 1639892 SU. MKI, B22 F9/02, 9/14 (Otkrytiya i Izobreteniya, **34**, No. 13: 11) (1991) (in Russian).
12. Yu. M. Koval' and V. V. Nemoshkalenko, *O Prirode Martensitnykh Prevrashcheniy* [On the Nature of Martensitic Transformations] (Kyiv: 1998) (Prepr./N.A.S. of Ukraine. Inst. for Metal Physics. No. 1, 1998) (in Russian).

Journal title abbreviations should conform to generally accepted styles:
https://www.cas.org/support/documentation/references/corejournals;
https://cdn.journals.aps.org/files/rmpguapb.pdf;
https://images.webofknowledge.com/WOK46P9/help/WOS/A_abrvjt.html;
https://mathscinet.ams.org/msnhtml/serials.pdf.

Equations and Formulae: Formulas in the text should be inserted by **MathType**, fully compatible with MS Office. Vectors should be typed in bold without arrows above. Note that complicated formulae, mathematical expressions or (de)notations are not recommended in the title, abstract, and keywords.

Tables: Number tables consecutively with Arabic numerals and give a clear descriptive caption at the top.

Figures: All figures should be numbered with consecutive Arabic numbers, have descriptive captions and be mentioned in the text. Keep figures separate at the end of the text and clearly label each figure with author's name and figure number. The labels at axis should contain the designation (or notation) of quantities and their units.

Preparation: Figures submitted must be of a high enough standard for reproduction with 300–600 dpi resolution (including half-tone illustrations). Redrawing or retouching of unusable figures will be charged to the authors.

Colour Plates: Whenever, the use of colour is an integral part of the research, or where the work is generated in colour, the Journal will publish (in paper version) the colour illustrations with charge to the author. Reprints in colour will carry a surcharge. Please write to the Publisher for details.

Submission of Electronic Text: Authors should submit the electronic version of their paper by e-mail to the Editorial Office. The text file should be saved in the native formats of the MS Word with a name consisting the name of the first author, for example, Hotovchenko.docx. The electronic form of figures (in TIF, EPS, JPG, PNG formats preferably and with name consisting the name of the first author also, for example, Hotovchenko_fig2a.jpg) should be planned so that they reduce to 12.7 cm column width (or less), and keep them separated from the text file. It is desirable to submit additionally all the **figures** within the format of the program, in which they were created.

Proofs: Contributors will receive page proofs for correction by e-mail as a PDF document. These must be returned to Kyiv office (mfint@imp.kiev.ua with subject beginning by word 'mfint') within 5 days of receipt.

Page Charges: There are no page charges to individuals or institutions.

Reprints: Authors can freely download a PDF version of their published article from journal website: https://mfint.imp.kiev.ua. The printed issues may be ordered by completing the appropriate form sent with proofs and prepaid by authors under the terms as for subscription.

Further Information: All questions arising during the **peer review** or after acceptance of manuscripts, especially those relating to reprints, should be directed to G. V. Kurdyumov Institute for Metal Physics, N.A.S. of Ukraine, Executive Managing Editor, Editorial Office, 36 Academician Vernadsky Blvd., UA-03142 Kyiv, Ukraine;
Fax: +380 44 4242561, e-mail: mfint@imp.kiev.ua (with subject beginning by word 'mfint').

We ask the authors to apply with their manuscript Copyright Transfer Agreement form.

Copyright Transfer Agreement

We, the undersigned authors of the manuscript '_____', transfer to the Founders, Publisher, and Editorial Board of the Journal 'Metallophysics and Advanced Technologies' (according to agreements between them) the right to publish this manuscript in original language or in translation to the other languages. We confirm that publication of this manuscript **will not** infringe a copyright of other persons or organizations and publication ethics.

Author(s):_____
(Last Name, First Name, Affiliation)

Correspondence Address:_____

Phone and e-mail: _____

_____ _____
(Signature) *(Date)*

ІНФОРМАЦІЯ (ПРАВИЛА) ДЛЯ АВТОРІВ

Науковий журнал «Металофізика та новітні технології» (МфНТ) щомісяця публікує статті, які раніше ще не публікувалися та не перебувають на розгляді для опублікування в інших виданнях. Статті мають містити результати експериментальних і теоретичних досліджень в області фізики та технологій металів, стопів і сполук з металічними властивостями; рецензії на монографії; інформацію про конференції, семінари; відомості з історії металофізики; рекламу нових технологій, матеріялів, приладів. Журнал дотримується загальноприйнятих принципів, зазначених на його сайті в документах з публікаційної етики та щодо неприйнятних практик.

Тематика журналу: *Електронні структура та властивості, Дефекти кристалічної ґратниці, Фазові перетворення, Фізика міцности та пластичности, Металічні поверхні та плівки, Будова та властивості наномасштабних і мезоскопічних матеріялів, Аморфний і рідкий стани, Взаємодії випромінення та частинок із конденсованою речовиною, Матеріяли в екстремальних умовах, Реакторне й авіакосмічне металознавство, Медичне металознавство, Нові металеві матеріяли та синтетичні метали, Металовмісні смарт-матеріяли, Фізико-технічні основи експерименту та діягностики, Дискусійні повідомлення*.

Статті публікуються однією з двох мов: англійською (віддається перевага) або українською.

Статті, в оформленні яких не дотримано наступних правил для опублікування в МфНТ, повертаються авторам без розгляду по суті. (Датою надходження вважається день повторного надання статті після дотримання зазначених нижче правил.)

1. Стаття має бути підписаною всіма авторами (із зазначенням їхніх адрес електронної пошти); слід вказати прізвище, ім'я та по батькові автора, з яким редакція буде вести листування, його поштову адресу, номери телефону та факсу й адресу електронної пошти.

2. Виклад матеріялу має бути чітким, **структурованим** (розділами, наприклад, «1. Вступ», «2. Експериментальна/Теоретична методика», «3. Результати та їх обговорення», «4. Висновки», «Цитована література»), стислим, без довгих преамбул, відхилень і повторів, а також без дублювання в тексті даних таблиць, рисунків і підписів до них. Анотація та розділ «Висновки» мають не дублювати один одного. Числові дані слід наводити в загальноприйнятих одиницях.

3. Об'єм оригінальної (неоглядової) статті має бути не більше 5000 слів (з урахуванням основного тексту, таблиць, підписів до рисунків, списку використаних джерел) і 10 рисунків. **Об'єм оглядової статті** — до 10000 слів та 30 рисунків.

4. За потреби до редакції може надаватися друкований (А4, подвійний інтервал) примірник рукопису з ілюстраціями.

5. До редакції обов'язково надається (по **e-mail**) файл статті, набраний у текстовому редакторі Microsoft Word, з назвою, що складається з прізвища першого автора (латиницею), наприклад, Hotovchenko.docx.

6. Електронна версія рукопису та його друкований варіянт (в разі його надання) мають бути ідентичними. Вони мають оформлюватися за шаблоном, який можна завантажити з сайту журналу, і містити 5–7 **індексів PACS** в редакції 'Physics and Astronomy Classification Scheme 2010'. Тексти статей мають також містити **назву статті**, **список авторів**, **повні назви** та **поштові адреси установ**, в яких вони працюють, **анотацію статті** (200–250 слів), **5–7 ключових слів** двома мовами (**англійською** та **українською**), а заголовки таблиць і підписи до рисунків мають подаватися **як мовою рукопису, так і англійською мовою**; англомовна анотація може бути представленою в більш розгорнутому варіянті (до 500 слів). Назва статті, її анотація та ключові слова мають не містити складні формули, математичні вирази чи позначення.

7. Електронні версії рисунків мають бути представленими у вигляді окремих файлів (у форматах TIF, EPS, JPG, PNG з розріженням у 300–600 dpi) з назвами, що складаються з прізвища першого автора (латиницею) та номера рисунка, наприклад, Hotovchenko_fig2a.jpg. Додатково рисунки надаються у форматі програми, в якій вони створювалися.

8. Написи на рисунках (особливо на півтонових) слід по можливості замінити літерними позначеннями (набраними на контрастному фоні), а криві позначити цифрами або різними типами ліній/маркерів, які мають бути роз'ясненими в підписах до рисунків або в тексті. На графіках усі лінії/маркери мають бути достатньої товщини/розміру для якісного відтворення їх у зменшеному в 2–3 рази вигляді (рекомендована початкова ширина рисунка — 12,7 см). Світлини мають бути чіткими та контрастними, а написи та позначення мають не закривати істотні деталі (для чого можна використовувати стрілки). Замість зазначення в підтекстовці збільшення під час зйомки бажано проставити масштаб (на контрастному фоні) на одній з ідентичних світлин. На графіках підписи до осей, **виконані мовою статті**, мають містити позначення (або найменування) величин, що відкладаються вздовж осей, і відділені комою їхні одиниці вимірювання.

9. Формули в текст треба вставляти за допомогою редактора формул **MathType**, сумісного з MS Office. **Вектори** слід набирати напівтовстим шрифтом без стрілок зверху.

10. Рисунки, таблиці, формули, а також підрядкові **примітки (виноски)** мають нумеруватися поспіль по всій статті.

11. Посилання на літературні джерела слід давати у вигляді порядкового номера, надрукованого в рядок у квадратних дужках. Список цитованої літератури складається почергово за першою згадкою джерела. Приклади оформлення посилань наведено нижче (просимо звернути увагу на порядок розташування ініціалів і прізвищ авторів, бібліографічних відомостей і на розділові знаки, а також на необхідність зазначення **всіх** співавторів цитованої роботи та її ідентифікатора **DOI**, якщо він є):

1. S. O. Firstov and T. G. Rogul, *Metallofiz. Noveishie Tekhnol.*, **44**, No. 1: 127 (2022) (in Ukrainian). https://doi.org/10.15407/mfint.44.01.0127
2. V. B. Tarelnyk, O. P. Gaponova, and Ye. V. Konoplianchenko, *Prog. Phys. Met.*, **23**, No. 1: 27 (2022). https://doi.org/10.15407/ufm.23.01.027
3. A. Meisel, G. Leonhardt, and R. Szargan, *Röntgenspektren und Chemische Bindung* [X-Ray Spectra and Chemical Bond] (Leipzig: Akademische Verlagsgesellschaft Geest & Portig K.-G.: 1977) (in German).
4. J. M. Ziman, *Printsipy Teorii Tverdogo Tela* [Principles of the Theory of Solids] (Moscow: Mir: 1974) (Russian translation).
5. M. A. Stucke, D. M. Dimiduk, and D. M. Hazzledine, *High Temperature Ordered Intermetallic Alloys. V* (Eds. I. Baker and R. Darolia) (Pittsburgh, PA, USA: MRS: 1993), p. 471.
6. *Handbook of Mathematical Functions with Formulas, Graphs and Mathematical Tables* (Eds. M. Abramowitz and I. A. Stegun), Nat'l Bureau of Standards. Appl. Math. Ser. Vol. **55** (Washington, D.C.: U.S. Govt. Printing Office: 1964).
7. B. B. Karpovych and O. B. Borovkoff, *Proc. of Symp. 'Micromaterials Engineering' (Dec. 25–31, 1999)* (Kyiv: RVV IMF: 2000), vol. **2**, p. 113 (in Russian).
8. A. Eh. Krug, *Abstr. Int. Conf. Phys. Phenomena (Dec. 25–31, 1991, Alushta)* (Kharkiv: 1991), p. 12.
9. T. M. Radchenko, *Vplyv Uporyadkuvannya Defektnoyi Struktury na Transportni Vlastyvosti Zmishanykh Krystaliv* [Influence of Ordering of the Defect Structure on Transport Properties of the Mixed Crystals] (Thesis of Disser. for the Degree of Dr. Phys.-Math. Sci.) (Kyiv: G. V. Kurdyumov Institute for Metal Physics, N.A.S.U.: 2015) (in Ukrainian). https://doi.org/10.13140/RG.2.2.35430.22089
10. E. M. Gololobov, V. B. Shipilo, N. I. Sedrenok, and A. I. Dudyak, *Sposob Polucheniya Karbonitridov Metallov* [Production Method of Metal Carbonitrides], Authors' Certificate 722341 SSSR (Publ. November 21, 1979) (in Russian).
11. V. G. Trubachev, K. V. Chuistov, V. N. Gorshkov, and A. E. Perekos, *Sposob Polucheniya Metallicheskikh Poroshkov* [The Technology of Metallic Powder Production]: Patent 1639892 SU. MKI, B22 F9/02, 9/14 (Otkrytiya i Izobreteniya, **34**, No. 13: 11) (1991) (in Russian).
12. Yu. M. Koval' and V. V. Nemoshkalenko, *O Prirode Martensitnykh Prevrashcheniy* [On the Nature of Martensitic Transformations] (Kyiv: 1998) (Prepr./N.A.S. of Ukraine. Inst. for Metal Physics. No. 1, 1998) (in Russian).

Слід використовувати загальноприйняті скорочення назв журналів:
https://www.cas.org/support/documentation/references/corejournals;
https://cdn.journals.aps.org/files/rmpguapb.pdf;
https://images.webofknowledge.com/WOK46P9/help/WOS/A_abrvjt.html;
https://mathscinet.ams.org/msnhtml/serials.pdf.

Необхідною вимогою є також надання авторами додаткового списку цитованої літератури (**References**) в **латинській транслітерації** (система **BGN/PCGN**; рекомендовані транслітератори: http://www.slovnyk.ua/services/translit.php; http://ru.translit.net/?account=bgn).

Після транслітерованих назв книг, дисертацій, патентів та ін. слід у квадратних дужках наводити їхній англомовний переклад (див. приклади вище). При транслітерації статей з МфНТ слід використовувати написання П.І.Б. авторів, наведені **лише** в англомовному змісті відповідного випуску, і **офіційну** транслітеровану назву журналу (див. також першу сторінку кожної статті та сайт).

12. Коректура авторам надсилається електронною поштою у вигляді pdf-файлу після завершення етапу **рецензування**. На перевірку коректури авторам відводяться 5 робочих днів. Після закінчення зазначеного терміну стаття автоматично направляється до друку. Виправлення слід відмітити та прокоментувати в самому pdf-файлі або оформити у вигляді переліку виправлень (підписаного уповноваженим представником колективу авторів) і переслати електронною поштою на адресу редакції.

Електронний варіянт статті надсилається на e-mail: mfint@imp.kiev.ua (з темою, що починається словом 'mfint'). Друкована версія рукопису (якщо у ній є потреба) надсилається за адресою: **Інститут металофізики ім. Г. В. Курдюмова НАН України, редакція МфНТ; бульвар Акад. Вернадського, 36; 03142 Київ, Україна** або відповідному реґіональному редактору (див. сайт).

Автори можуть вільно завантажити pdf-файли опублікованих статей з сайту журналу (https://mfint.imp.kiev.ua), а також замовити друковані примірники випуску журналу зі своєю статтею, надіславши до редакції журналу **разом з коректурою відповідну заявку та квитанцію про оплату** друку необхідної кількості примірників випуску на умовах, аналогічних передплатним.

Відповідно до угод між редакцією МфНТ, засновниками та видавцем журналу, редакція вважає, що автори, надсилаючи їй рукопис статті, передають засновникам, видавцю та редколеґії право опублікувати цей рукопис мовою ориґіналу та в перекладі іншими мовами, і просить авторів відразу прикладати до рукопису «Угоду про передачу авторського права».

Угода про передачу авторського права

Ми, що нижче підписалися, автори рукопису «_____», передаємо засновникам, видавцю та редколеґії журналу «Металофізика та новітні технології» (згідно з угодами між ними) право опублікувати цей рукопис мовою ориґіналу та в перекладі іншими мовами. Ми підтверджуємо, що ця публікація **не** порушує авторського права інших осіб або організацій і принципів наукової етики. При цьому за авторами зберігаються всі інші права як власників цього рукопису.

Підписи авторів: _____ (П.І.Б., дата, адреса, тел., e-mail)

Metallophysics and Advanced Technologies
Металофіз. новітні технол.
Metallofiz. Noveishie Tekhnol.
2025, vol. 47, No. 1, pp. 1–7
https://doi.org/10.15407/mfint.47.01.0001
Reprints available directly from the publisher

PACS numbers: 71.15.Ap, 71.15.Mb, 71.20.-b, 72.15.Eb, 81.05.Bx, 81.05.Ea, 81.05.Zx

Зонна структура нітриду Алюмінію та його твердих розчинів із Маґнієм і Оксиґеном

В. М. Уваров, М. П. Мельник, Ю. В. Кудрявцев, М. В. Уваров,
Е. М. Руденко, М. В. Немошкаленко

Інститут металофізики ім. Г. В. Курдюмова НАН України,
бульв. Академіка Вернадського, 36,
03142 Київ, Україна

За допомогою зонних розрахунків в рамках повнопотенціяльного лінеаризованого методу приєднаних пласких хвиль (FLAPW-методу) одержано інформацію про енергетичну зонну структуру $E(\mathbf{k})$ нітриду Алюмінію та його твердих розчинів з Оксиґеном і Маґнієм. Встановлено, що енергетична зонна структура цих розчинів вказує на їхній металічний стан.

Ключові слова: зонні розрахунки, електронна будова, нітрид Алюмінію, тверді розчини.

Using the band-structure calculations within the FLAPW (the full-potential linearized augmented-plane-wave) method, information about the energy band structure $E(\mathbf{k})$ of aluminium nitride and its solid solutions with oxygen and magnesium is obtained. As established, the energy band structure of these solutions indicates their metallic state.

Key words: band-structure calculations, electronic structure, aluminium nitride, solid solutions.

Corresponding author: Viktor Mykolayovych Uvarov
E-mail: uvarov@imp.kiev.ua

G. V. Kurdyumov Institute for Metal Physics, NAS of Ukraine,
36 Academician Vernadsky Blvd., UA-03142 Kyiv, Ukraine

Citation: V. M. Uvarov, M. P. Mel'nyk, Yu. V. Kudryavtsev, M. V. Uvarov, E. M. Rudenko, and M. V. Nemoshkalenko, Band Structure of Aluminium Nitride and Its Solid Solutions with Magnesium and Oxygen, *Metallofiz. Noveishie Tekhnol.*, **47**, No. 1: 1–7 (2025).DOI: 10.15407/mfint.47.01.0001

(Отримано 27 вересня 2024 р.; остаточн. варіянт — 14 листопада 2024 р.)

1. ВСТУП

Унікальні властивості нітриду Алюмінію AlN зробили його достатньо перспективним для застосування у новітніх технологіях. Це — електронна кераміка, що характеризується значним електроопором [1], гарною діелектричною міцністю [2], значною твердістю [3] і коефіцієнтом теплового розширення (КТР), близьким до КТР кремнію [4]. Крім того, він є стійким щодо окиснення та зношування, має значну теплопровідність, порівнянну з теплопровідністю високопровідних металів, таких як алюміній [5]. Ці властивості зберігаються у плівках AlN [6, 7]. Згадані характеристики роблять AlN ідеальним кандидатом для використання в підкладинках для мікроелектроніки.

Нітрид Алюмінію є ізолятором з широкою забороненою зоною. У спектрах оптичного поглинання AlN-плівок мікронної товщини ідентифіковано кілька компонент [8], включаючи енергії 4,5 еВ і 4,8 еВ, а також пік з максимальною інтенсивністю при 6,2 еВ. Також зареєстровано низькоенергетичний пік при 2,8 еВ в одному з досліджень [9]. Низькоенергетичні особливості спектрів часто пов'язують з домішками, які пов'язані з киснем, тоді як компонента з максимальною інтенсивністю при 6,2 еВ приписується збудженню валентних електронів у зону провідности AlN (див. [8] і посилання там). Це значення в даний момент прийнято як експериментально визначена ширина забороненої зони нітриду Алюмінію.

Залежно від використовуваних квантово-механічних методів розрахунку, енергії прямої забороненої зони для AlN варіюються від 2,35 еВ до 5,31 еВ [10–13]. В одному з досліджень [14] з використанням напівемпіричної методи сильного зв'язку для неї було одержано значення 6,2 еВ.

Зонна структура $E(\mathbf{k})$ твердих розчинів нітриду Алюмінію з Оксиґеном і Маґнієм свідчить [15], що нітрид Алюмінію є ізолятором, тоді як більшість його оксидів представлено металами.

В даній роботі розраховується зонна структура твердих розчинів нітриду Алюмінію з Оксиґеном і Маґнієм з метою встановлення їхніх електропровідних властивостей.

2. МЕТОДИКА ПРОВЕДЕННЯ РОЗРАХУНКІВ

В роботі проведено зонні розрахунки електронної будови нітриду Алюмінію та його твердих розчинів — моделів з Оксиґеном і Маґнієм. Елементарні комірки досліджуваних сполук пронумеровано ве-

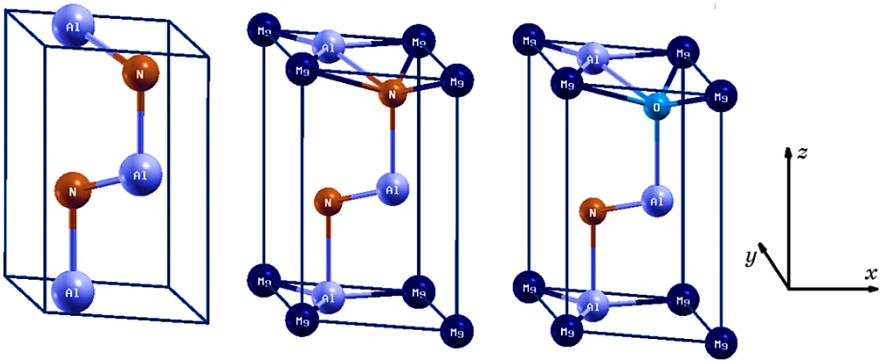

Рис. 1. Елементарні комірки нітриду Алюмінію ($K = 1$) та його сполук із Маґнієм ($K = 2$), а також із Маґнієм і Оксиґеном ($K = 3$). Система координат є однаковою для всіх комірок. Тут і далі на рисунках K позначає атомну конфіґурацію.

Fig. 1. Conventional cells of aluminium nitride ($K = 1$) and its compounds with magnesium ($K = 2$), as well as with magnesium and oxygen ($K = 3$). The coordinate system is the same for all cells. Here and further in the figures, K denotes the atomic configuration.

личинами $K = 1–3$ (K — атомна конфіґурація) і наведено на рис. 1. Структура $K = 1$ базового нітриду Алюмінію належить до гексагональної синґонії з симетрією $P63mc$ (просторова група № 186) [16]. Твердий розчин з додаванням Маґнію на рис. 1 представлено елементарною коміркою $K = 2$, тоді як похідна від неї $K = 3$ моделює розчин із заміщенням атомами Оксиґену атомів у самому «тілі» AlN.

Зонні розрахунки виконані в LAPW-наближенні [17] з ґрадієнтною апроксимацією електронної густини (GGA — generalized gradient approximation) в формі [18]. Для розрахунку характеристик електронної структури сполук використано скалярно-релятивістський варіянт LAPW-методи [19].

ТАБЛИЦЯ 1. Положення атомів у структурі стопу Al_2N_2Mg в частках ребер елементарної комірки ($K = 2$).

TABLE 1. The positions of atoms inside the Al_2N_2Mg-alloy structure in the fractions of the unit-cell edges ($K = 2$).

	x	y	z
Al_1	1/3	2/3	0,0
Al_2	2/3	1/3	0,5
N_1	1/3	2/3	0,381
N_2	2/3	1/3	0,881
Mg	0,0	0,0	0,0

Положення компонентів атомів у структурі досліджуваних сполук задавалися з використанням операцій симетрії примітивної гексагональної ґратниці H і даних, наведених у табл. 1. Тут координати атомів Алюмінію та Нітроґену з індексами 1 і 2 відображають структуру AlN. Структура стопу з Оксиґеном Al_2NOMg ($K = 3$) моделювалася шляхом заміщення атомів Нітроґену N атомами Оксиґену O в комірці $K = 2$.

Радіюси MT (muffin-tin) атомних сфер вибиралися з міркувань мінімізації розмірів міжсферної области II в модифікації $K = 1$, яка має найменший об'єм елементарної комірки. Для всіх просторових конфіґурацій і всіх атомів ці радіюси склали 1,69 Бора (1 Бор = $5{,}2918 \cdot 10^{-11}$ м). Під час розрахунків характеристик електронної будови всіх сполук використовувалося 168 точок у незвідних частинах їхніх Бріллюенових зон. Добуток радіюса MT-сфери (R_{mt}) і максимального значення хвильового вектора пласких хвиль (K_{max}) вибрано рівним сімом, а максимальне значення квантового числа — $l = 10$ для парціяльних хвиль всередині сфер і $l = 4$ в обчисленнях non-muffin-tin-матричних елементів.

Оскільки в літературі відсутня інформація про значення параметрів гексагональних ґратниць, які належать до твердих розчинів нітриду Алюмінію, то їх було розраховано з використанням процедури мінімізації просторової структури [19].

3. ОБГОВОРЕННЯ ОДЕРЖАНИХ РЕЗУЛЬТАТІВ

Структури енергетичних зон $E(\mathbf{k})$ нітриду Алюмінію AlN наведено на рис. 2. Видно, що сам нітрид Алюмінію ($K = 1$) представлений ізолятором. Заборонена зона енергій (E_{Gap}) у структурі нітриду Алюмінію становить 4,2 еВ, є прямою та зосередженою в точці Γ Бріллюенової зони. Одержане значення E_{Gap} виявилося помітно меншим за експериментально визначене 6,2 еВ і відображає загальну тенденцію занижених її величин, яких одержано в зонних розрахунках (див. Вступ). Однією з можливих причин цього можна вказати на той факт, що більшість зонних розрахунків не описують коректно збуджені кінцеві стани електронів, які проявляються в експериментах.

Внески електронних станів атомів у загальну структуру $E(\mathbf{k})$ для верхніх валентних і нижніх вакантних зон виявляються в значній мірі різними. В стелі валентної зони (точка Γ) переважають електронні стани атомів Нітроґену. Їхня симетрія пов'язана з N2p-електронами. Дно смуги провідности нітриду Алюмінію у точці Γ сформовано гібридизованими станами як атомів Нітроґену, так і атомами Алюмінію. Симетрію цих станів в основному зумовлено s-електронами атомів обох сортів.

Внесення в кристалічну ґратницю нітриду Алюмінію AlN атомів

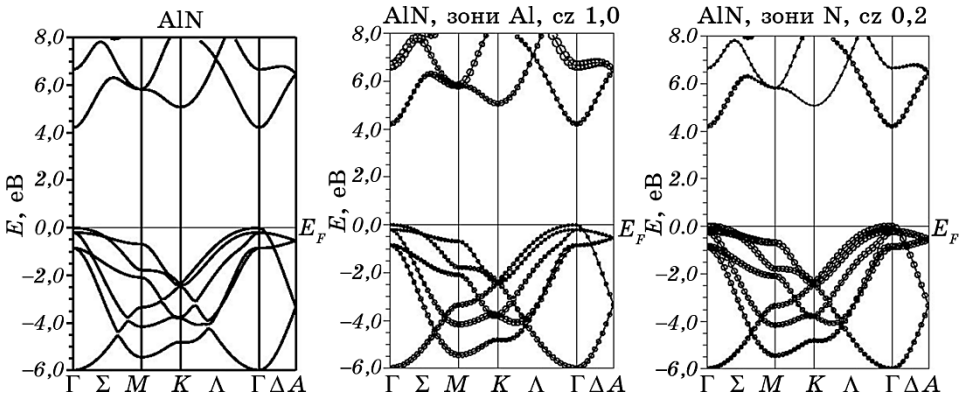

Рис. 2. Енергетична зонна структура $E(\mathbf{k})$ нітриду Алюмінію AlN. Радіюси кружків пропорційні внескам електронних станів атомів у загальну структуру $E(\mathbf{k})$. Обрані параметри припасування circle size (cz) уможливили побудувати наочно-порівняльну картину розподілів енергій у оберненому просторі **k**-векторів. У реальності за однакових значень cz радіюси кружків у спектрі станів атомів Нітроґену мають бути збільшені в 5 разів. Тут і на рис. 3 E_F — положення Фермі-рівня.

Fig. 2. The energy band structure $E(\mathbf{k})$ of aluminium nitride AlN. The radii of the circles are proportional to the contributions of the electron states of atoms to the overall structure $E(\mathbf{k})$. The selected fitting parameters for circle size (cz) allowed for the construction of a visually comparable depiction of energy distributions in the reciprocal space of **k**-vectors. In reality, at identical values of cz, the radii of the circles in the spectrum of nitrogen-atom states should be increased by a factor of 5. Here and in Fig. 3, E_F denotes the Fermi-level position.

Маґнію й Оксиґену приводить до істотних змін у структурах $E(\mathbf{k})$ (рис. 3). Це проявляється у відсутності в їхньому складі заборонених енергетичних зон, які відокремлюють валентні та вакантні електронні стани. Остання обставина явно вказує на те, що твердий розчин нітриду Алюмінію з Маґнієм Al_2N_2Mg і його окиснена форма Al_2NOMg є металічними.

Проте, пряма енергетична щілина, локалізована в інтервалі Λ–Γ Бріллюенової зони, присутня в спектрі $E(\mathbf{k})$ оксиду Al_2NOAl (рис. 3). Її значення визначається як $E_{\text{Gap1}} = 0{,}25$ еВ. Щілина меншої величини $E_{\text{Gap2}} = 0{,}23$ еВ є непрямою, що відповідає електронним переходам між точками Бріллюенової зони $K \to \Lambda$–Γ за участю фононів. У випадку практичної реалізації оксиду, що обговорюється, з алюмінієм малі значення цих щілин можуть вказувати на напівпровідникові властивості обговорюваного оксиду з алюмінієм за рахунок підвищеної ймовірности збудження валентних електронів у смугу провідности.

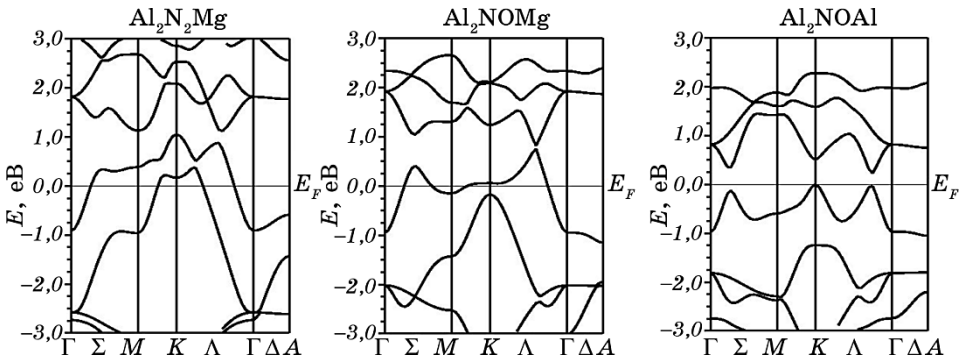

Рис. 3. Енергетична зонна структура твердих розчинів нітриду Алюмінію з Маґнієм Al_2N_2Mg (структура $K = 2$), Оксиґеном і Маґнієм Al_2NOMg ($K = 3$), Оксиґеном і Алюмінієм Al_2NOAl [15] (аналог $K = 3$ на рис. 1).

Fig. 3. The energy band structure of solid solutions of aluminium nitride with magnesium Al_2N_2Mg (structure $K = 2$), with oxygen and magnesium Al_2NOMg ($K = 3$), and with oxygen and aluminium Al_2NOAl [15] (analogous to $K = 3$ in Fig. 1).

4. ВИСНОВКИ

1. Нітрид Алюмінію є ізолятором із розрахованою прямою енергетичною щілиною величиною у 4,2 еВ, розташованою в точці Γ Бріллюенової зони. В стелі валентної зони переважають електронні стани атомів Нітроґену, пов'язані з N2*p*-електронами. Дно смуги провідности нітриду Алюмінію сформовано переважно гібридизованими *s*-станами атомів обох сортів.
2. Внесення в кристалічну ґратницю нітриду Алюмінію AlN атомів Маґнію й Оксиґену приводить до відсутности в структурі $E(\mathbf{k})$ заборонених енергетичних зон, що відокремлюють валентні та вакантні електронні стани. Остання обставина вказує на те, що твердий розчин нітриду Алюмінію з Маґнієм Al_2N_2Mg та його окиснена форма Al_2NOMg є металічними.
3. У спектрі $E(\mathbf{k})$ оксиду Al_2NOAl є пряма енергетична щілина величиною $E_{\text{Gap1}} = 0{,}25$ еВ, локалізована в інтервалі Λ–Γ Бріллюенової зони. Щілина меншої величини $E_{\text{Gap2}} = 0{,}23$ еВ є непрямою та відповідає електронним переходам між точками Бріллюенової зони $K \to \Lambda$–Γ за участю фононів. У випадку практичної синтези оксиду Al_2NOAl малі значення цих щілин можуть вказувати на його напівпровідникові властивості за рахунок підвищеної ймовірности збудження валентних електронів у смугу провідности.

ЦИТОВАНА ЛІТЕРАТУРА—REFERENCES

1. A. W. Weimer, G. A. Cochran, G. A. Eisman, J. P. Henley, B. D. Hook, L. K. Mills, T. A. Guiton, A. K. Knudsen, N. R. Nicholas, J. E. Volmering, and W. G. Moore, *J. Am. Ceram. Soc.*, **77**, Iss. 1: 3 (1994).
2. A. V. Virkar, T. B. Jackson, and R. A. Cutler, *J. Am. Ceram. Soc.*, **72**: 2031 (1989).
3. T. J. Mroz Jr., *Ceram. Bull.*, **71**: 782 (1992).
4. P. T. B. Shaffer and T. J. Mroz Jr., *Aluminum Nitride* (Advanced Refractory Technology: 1991).
5. A. Glen, R. A. Slack, R. Tanzilli, O. Pohl, and J. W. Vandersande, *J. Phys. Chem. Solids*, **48**: 141 (1987).
6. O. Ye. Pogorelov, O. V. Filatov, E. M. Rudenko, I. V. Korotash, and M. V. Dyakin, *Progress in Physics of Metals*, **24**, No. 2: 239 (2023).
7. E. M. Rudenko, A. A. Krakovnyi, M. V. Dyakin, I. V. Korotash, D. Yu. Polotskiy, and M. A. Skoryk, *Metallofiz. Noveishie Tekhnol.*, **44**, No. 8: 989 (2022) (in Ukrainian).
8. S. Strite and H. Morkoc, *J. Vac. Sci. Technol. B*, **10**: 1237 (1992).
9. W. M. Yim, E. J. Stofko, P. J. Zanzucchi, J. I. Pankove, M. Ettenberg, and S. L. Gilbert, *J. Appl. Phys.*, **44**: 292 (1973).
10. B. Hejda, *phys. status solidi (b)*, **32**, Iss. 1: 407 (1969).
11. S. Bloom, *J. Phys. Chem. Solids*, **32**: 2027 (1971).
12. D. Jones and A. H. Lettington, *Solid State Commun.*, **11**: 701 (1972).
13. W. Y. Ching and B. N. Harmon, *Phys. Rev. B*, **34**: 5305 (1986).
14. A. Kobayashi, O. Sankey, S. M. Yolz, and J. D. Dow, *Phys. Rev. B*, **28**: 935 (1983).
15. V. M. Uvarov, E. M. Rudenko, Yu. V. Kudryavtsev, M. V. Uvarov, I. V. Korotash, and M. V. Dyakin, *Metallofiz. Noveishie Tekhnol.*, **46**, No. 3: 199 (2024).
16. C. Yeh, Z. W. Lu, S. Froyen, and A. Zunger, *Phys. Rev. B*, **46**: 10086 (1992).
17. D. Singh, *Plane Waves, Pseudopotentials and LAPW Method* (Kluwer Academic: 1994).
18. J. P. Perdew, S. Burke, and M. Ernzerhof, *Phys. Rev. Lett.*, **77**: 3865 (1996).
19. P. Blaha, K. Schwarz, G. K. Madsen, D. Kvasnicka, J. Luitz, R. Laskowsk, F. Tran, and L. D. Marks, *WIEN2k, An Augmented Plane Wave + Local Orbitals Program for Calculating Crystal Properties* (Wien: Techn. Universität: 2001).

Metallophysics and Advanced Technologies
Металофіз. новітні технол.
Metallofiz. Noveishie Tekhnol.
2025, vol. 47, No. 1, pp. 9–24
https://doi.org/10.15407/mfint.47.01.0009
Reprints available directly from the publisher

PACS numbers: 46.55.+d, 62.20.Qp, 68.35.Af, 75.70.Cn, 81.40.Pq, 82.40.Ck, 83.60.Np

Formation of Dissipative Surface Structures during Friction Interaction of Solid Bodies in an External Magnetic Field

M. M. Svyryd, V. I. Dvoruk, O. O. Mikosyanchyk, O. Y. Sydorenko, and V. M. Borodiy

National Aviation University,
1 Lyubomyr Huzar Ave.,
UA-03058 Kyiv, Ukraine

The method of formation of the dissipative structures (DS) consisting of wear products obtained during the frictional interaction of solid bodies in a magnetic field (MF) is presented. A physical model of the local influence of MF on the mechanism of formation of the wear-surface DS of a ferromagnetic (steel 45) paired with a diamagnetic (glass) during sliding friction without lubrication is presented. The parameters of the movement and fixation of wear products on the worn surface depending on the direction of MF are determined. As established, the intensity of wear is subjected to the physical laws of the impact of MF on the magnets, which are on the path of its magnetic lines through the actual contact surface.

Key words: magnets, friction, magnetic field, nanostructure, wear products.

Представлено методику формування дисипативних структур (ДС), що складаються з продуктів зносу, одержаних під час фрикційної взаємодії твердих тіл у магнетному полі (МП). Вибудовано фізичний модель локального впливу МП на механізм формування ДС зношуваної поверхні феромагнетика (криця 45) у парі з діямагнетиком (склом) під час тертя ковзання без змащування. Визначено параметри переміщення та фіксації продуктів зносу на зношуваній поверхні залежно від напрямку МП. Вста-

Corresponding author: Mykhaylo Mykolayovych Svyryd
E-mail: svirid_mn@ukr.net

Citation: M. M. Svyryd, V. I. Dvoruk, O. O. Mikosyanchyk, O. Y. Sydorenko, and V. M. Borodiy, Formation of Dissipative Surface Structures during Friction Interaction of Solid Bodies in an External Magnetic Field, *Metallofiz. Noveishie Tekhnol.*, **47**, No. 1: 9–24 (2025). DOI: 10.15407/mfint.47.01.0009

новлено, що інтенсивність зношування підпорядковується фізичним закономірностям впливу МП на магнетики, які знаходяться на шляху проходження його магнетних ліній через фактичну площу контакту.
Ключові слова: магнетики, тертя, магнетне поле, наноструктура, продукти зношування.

(Received 25 October, 2023; in final version, 14 October, 2024)

1. INTRODUCTION

Any structure used in mechanical engineering is designed to perform a specific job of transmitting forces and loads. Therefore, it is always in an unbalanced tense state. This causes the need for additional energy costs with further reflection in the change of surface topography under the action of deformation components [1–3]. In this regard, energy support of the structure is necessary to ensure appropriate operating parameters.

The most stable and not subject to premature changes method of such support is the use of an external static magnetic field (MF). The energy state of the specified field practically does not change over time. It is stable in terms of internal parameters, but it has different effects on magnets in the area of its influence. With regard to such a design as a tribomechanical system, the action of the MF manifests itself in a change in the atomic structure of the magnets from which its triboelements are made, as well as the components of the specified structure. This is inevitably reflected in the conditions and parameters of the formation of dissipative structures (DS) in the zone of frictional interaction, which, in turn, ambiguously affect the structural components of magnets.

The effect of MF on the deformation parameters and wear products (WP) of the surface is most conveniently detected in sliding friction without lubrication.

From the energy point of view, the tribomechanical system refers to an open type relative to the environment, from which energy is supplied by mechanical, chemical (interaction with the environment), thermal (both from friction and from the outside) method, as well as activation using an external magnetic field in combination with the Earth's magnetic field (0.0005 T). The energy conditions of such a system are characterized by an increase in entropy, due to the contact spots of the actual contact surface (ACS), developed in the process of frictional interaction.

The basis of the conducted research was the development of a physical model of the tribomechanical system, which takes into account the location of its energy flows relative to the ACS. Research technology using a ferromagnetic–diamagnetic friction pair, in which the latter is transparent to the passage of light, and its characteristics are close to a completely solid body, is presented in the work [4]. This makes it possi-

ble to monitor the process of formation of DS in the air, as well as the influence of MF on the placement of WP in the zone of frictional interaction, which depends on the structure of protective tribological films.

The mechano-physicochemical process of the surface-film formation mechanism is determined in the scientific works of B. I. Kostetskyi [5], according to which, during friction, wear particles are dispersed with their subsequent sintering in the ACS zones.

At the same time, the geometric sizes of the particles acquire a wide spectrum of fractions from dozens of a micron to hundredths of a millimetre [6], from which their conglomerate clusters are subsequently formed (Fig. 1): the larger the size, the lower the surface energy of the particles during deformation of the conglomerate. Nanoparticles (up to 10 nm) in such a conglomerate have a higher surface energy [7].

Materials formed in the parameters of nanoparticles are characterized by significantly better physical properties compared to monolithic metal: magnetic, surface energy, anisotropy, *etc*. [8]. Particles of micron-sized materials can be compared to near-surface atoms, therefore, in such systems, excess surface energy appears, which leads to the appearance of a highly defective state of individual nanoparticles. Nanoparticles of ferromagnetic metals Fe, Co, Ni and alloys oxidize very quickly in normal atmospheric conditions, so they are protected by a coating comparable in thickness to the size of the particles themselves [9].

Thus, in the conditions of the applied research technology, it is necessary to take into account the chemical activity of nanoparticles, as a drawback of nanoclass materials.

In the conditions of sliding friction, a wide range of WP fractions is formed, but particles larger than 500 μm are filtered out due to the action of centrifugal forces, as well as the presence of filters in lubrication, fuel and hydraulic systems.

2. STATEMENT OF THE PROBLEM AND OBJECTIVE OF THE RESEARCH

The primary parameter that characterizes the conditions of operation of a tribomechanical system is the presence of DS in the contact zone capable of ensuring that it performs the relevant technical functions [10]. The determining factor in the formation of DS is the presence of a donor of its elements with the necessary properties. Donor elements must be subject to directed movement in the contact zone under the influence of external energy flows. During sliding friction without lubrication, the worn surfaces are subjected to the directed action of auxiliary energy flows and the deformation component in the unstable structure of the ACS.

The purpose of the study is studying the regularities of the formation of dissipative surface structures during the frictional interac-

tion of solid bodies in an external magnetic field, which will contribute to increasing the wear resistance of the tribosystem.

The research hypothesis is based on the restoration of triboelements in the process of frictional interaction due to the formation of nanocoatings from wear products on their surfaces under the directed action of the energy flow of the external MF.

3. MATERIALS AND RESEARCH METHODS

Two materials are used in the studied tribomechanical system: the first is a sample made of martensite-hardened ferromagnetic steel 45, the second is a counter-body made of diamagnetic glass. Using a solid transparent substance (glass), it is possible to monitor the kinetics and mechanism of wear and formation of DS on the surface of the ferromagnetic sample (Fig. 1). Tribological studies of the sample on the counter-body were carried out at a relative displacement speed of $V = 0.1$ m/s and a normal load of 1 N per sample area of 7.56 mm^2. The topography of the surface of steel 45 is shown in Fig. 1, on which present a significant deposit of a conglomerate of iron oxides [11].

Formatted during the relative movement of triboelements, WP are located in the gaps between their surfaces, forming DS from conglomerates that fill the depressions of the roughness on them.

3.1. Determination of Tribological Characteristics of Ferromagnetic WP Depending on the Direction of Influence of MF on the ACS Zone

The effect of MF and its direction in the process of friction without lubri-

Fig. 1. Friction surface of steel 45 in dynamic mode when moving on glass without the influence of a magnetic field.

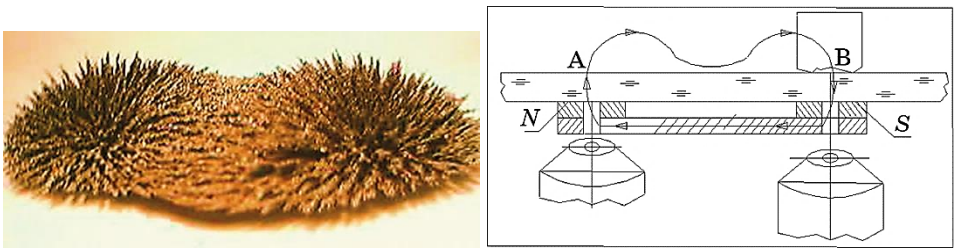

a *b*

Fig. 2. Scheme: configuration of the magnetic field of the magnet used in the experiment (from the hard drive) (*a*), passage of ML through a bipolar magnet, glass and the body of a ferromagnetic sample (*b*).

cation was studied according to the method [4] on the tribological complex. The sample was placed in positions (A or B, Fig. 2, *b*) in such a way that the magnetic lines (ML) crossed the friction plane perpendicularly.

The results of determining the intensity of wear during tribocontact without lubrication of steel 45 on glass under conditions of sliding friction according to the finger-plane friction scheme are shown in Fig. 3 (curve *1*). In the same Figure, the curves characterizing the influence of the change in the direction of MF from the sample (MF-*SN* curve) and into the sample (MF-*NS* curve) on the wear intensity are presented.

Therefore, in the position of sample A (Figure 2), MF, which is directed into this sample and corresponds to MF-*NS* curve (Fig. 3), contributes to the minimum value of the intensity of wear. The position of sample B on

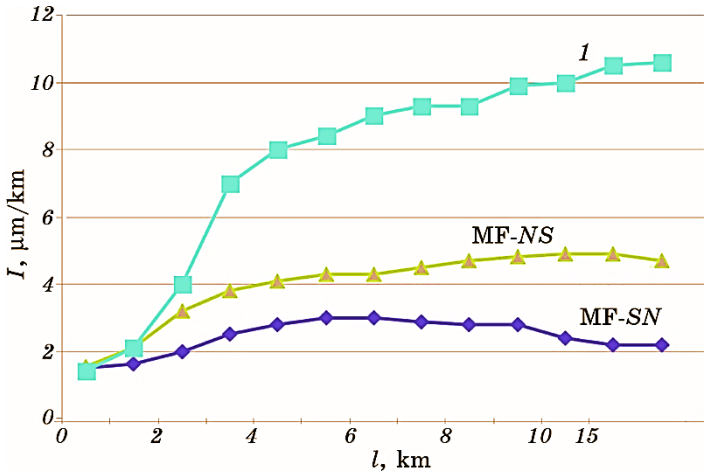

Fig. 3. Intensity of wear of steel 45 during friction sliding on glass: curve *1* — friction, without the influence of MF, MF-*SN* with *SN* direction, MF-*NS* with N_S referral.

the pole of *SN* magnet (Fig. 2) reflects the direction of MF from the sample in which the intensity of wear increases (Fig. 3, curve MF-*SN*).

The curve *1* is characterized by the greatest intensity of wear due to the action of the created oxide conglomerates (Fig. 1) [11] and rapid oxidation of FeO, Fe_2O_3, Fe_3O_4. The activation of oxygen in the contact zone is due to the following factors: increased energy state of the surface of iron nanoparticles, saturation of the contact zone with paramagnetic oxygen, which under the influence of MF concentrates in areas of the ACS.

Thus, the ferromagnetic sample forms a layer of nanoparticles of ferromagnetic DS based on iron oxide Fe_3O_4 between the surfaces of triboelements.

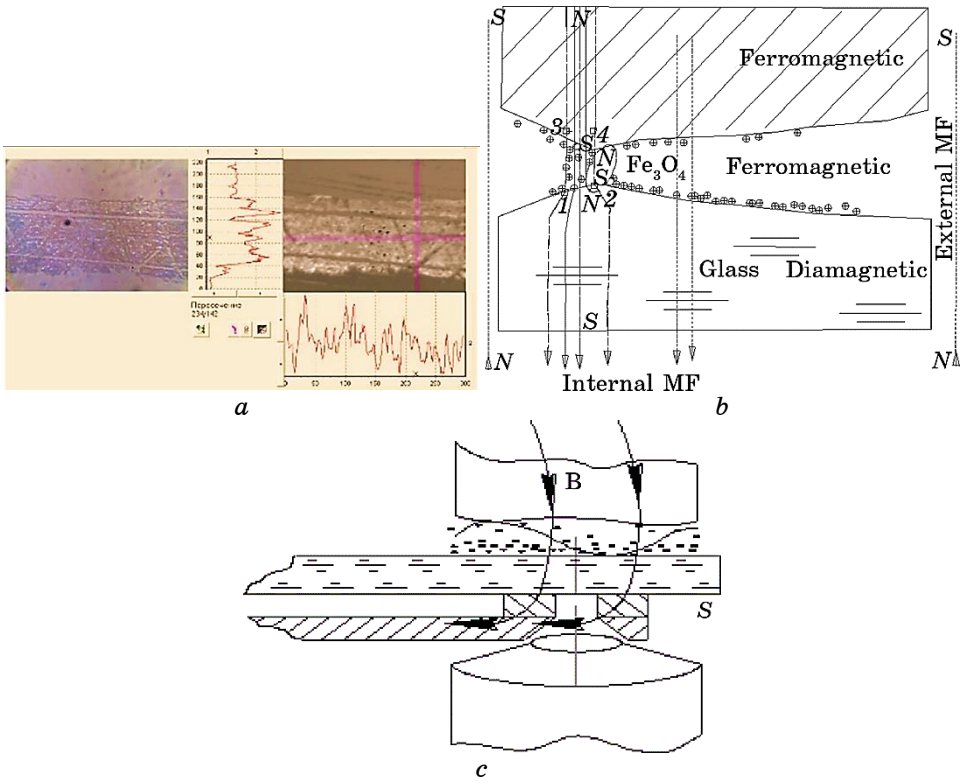

Fig. 4. Profilogram of the friction track on the glass (see Fig. 2, plane B) and topography of the surface with the direction of the external MF in the direction of the *SN* glass (*a*), the scheme of the location of wear products in the directed MF on the pole *SN* corresponds to plane B of Fig. 2 (*b*), scheme-model of the transition zone of friction between the sample and the glass in the resulting MF (*c*).

3.2. Physical Model of the Mechanism of Tribomagnetic Contacting

The influence of MF on the formation of the structure under the action of dynamic loads and deformation movements is perceived by different materials individually. The passage of MF through a ferromagnetic medium significantly increases its induction due to the peculiarities of the structural structure of the crystal lattice and the presence of a significant number of free electrons, which by their excitations create an internal MF, which is much larger than the external MF. Due to this, the magnetic susceptibility of the material (χ) increases, which in Fig. 4, *c* in the *1–2–3–4* zone is represented by the concentration of ML, both in the metal and in DS zone. Since the ACS contact is always characterized by an elevated temperature up to the level of welding bridges due to a significant deformation component between the protrusions of the interacting surfaces.

However, above the Curie temperature, the ferromagnetic properties changes dramatically to paramagnetic. Such structural transformations are formed in the areas of ACS during the relative movement of the surfaces even under insignificant loads and velocities.

At the same time, taking into account that the magnetic susceptibility of a ferromagnet is always significantly greater ($\chi_m >> 1$) than that of air ($\chi_m < 1$), therefore MF is concentrated in the sample at ACS transitions, which in the total area are realized on the plane of 0.1% of the total contact, on which ML are formed into a dense magnetic flux, the value of which is the sum of the ACS points of the contact (shown on the example of one touch ACS (Fig. 4, *b*) in the volume of space *1–2–3–4*).

So, at the point of contact *3–4* in Figure 4, *c* between steel and DS, the direction of MF does not change, however, a change in the specified direction is observed around the contact areas. This happens due to a decrease in the strength of the magnetic flux, as well as a smaller value of the magnetic permeability of paramagnetic air compared to a ferromagnetic. The change in the direction of the magnetic field can occur not only around ACS zones, but also near them [12]. If we take into account that the contact planes occupy 0.1% of the working plane, then a significant magnetic potential is concentrated on them [13], which can reach up to 30 Wb instantaneously. At the same time, DC are formed under the influence of a significant magnetic flux (Fig. 4, *b*, zone *1–2–3–4*), as well as the surface energy of nanoparticles. Small ferromagnetic particles (1–100 μm) are attracted to the glass and are located on the surface in the form of a track of magnetized conglomerates, which mechanically 'are smeared' in the direction of movement of the sample across the glass surface (Fig. 4, *a*) [14].

The directional MF affects the relative displacements of WP of the ferromagnetic, which at the transitions between the friction surfaces change their direction and location relative to the rough surface of the

a *b*

Fig. 5. The friction surface: on the glass at *SN* pole (*a*), on steel 45 in the direction of *SN* magnetic field (*b*), ×100.

steel [14]. At the same time, the density and direction of ML changes depending on the magnetic permeability of the ferromagnetic material ($\mu >> 10^3$–10^6).

The ML direction vector and the magnetic susceptibility of steel and glass in their own way affect the location of the WP in the contact zone and around it.

Thus, the movement of the magnetized WP creates a DC on the surface of the model counter-body—glass (Fig. 4, *a*). The wear products of ferromagnetic steel 45, kept in the contact zone. They are pressed to the glass by the directed field from the ferromagnet (Fig. 4, *b*, *c*, zone *1–2*, Fig. 5, *a*) and, forming into conglomerates on its surface, reduce wear and the coefficient of friction [15]. At the same time, the surface of the sample is characterized by structured DS and the presence of local thin deposited zones (Fig. 5, *b*).

If the direction of the magnetic field is changed to the opposite, *i.e.* from *NS* pole of the magnet to the sample (Fig. 2), on which the near end will form *SN* pole, and the opposite one will take on the value of *NS*, then the character of the friction surface (Fig. 6, *a*) will take the form of curve MF-*NS* (Fig. 3).

In this position, WP are accumulated not only near the sample, but are also drawn into the contact zone, while the wear is reduced by approximately 2.5–3 times, compared to the wear (curve MF-*SN*, Fig. 3). This is explained by the forced retention of PW by the directed flow of the magnetic field (zone *1–2–3–4*, Fig. 6, *b*), which is directed into the body of the ferromagnetic from the surface of the steel 45.

At the same time, there is a significant decrease in the coefficient of friction to the level of 0.07–0.1 is observed. On the friction surface of the sample, WP is held by MF, followed by their dispersion to the finest fractions on the sample (Fig. 7, *a*). Larger particles (size 10–20 μm) repeatedly enter the friction zone and contribute to increased wear re-

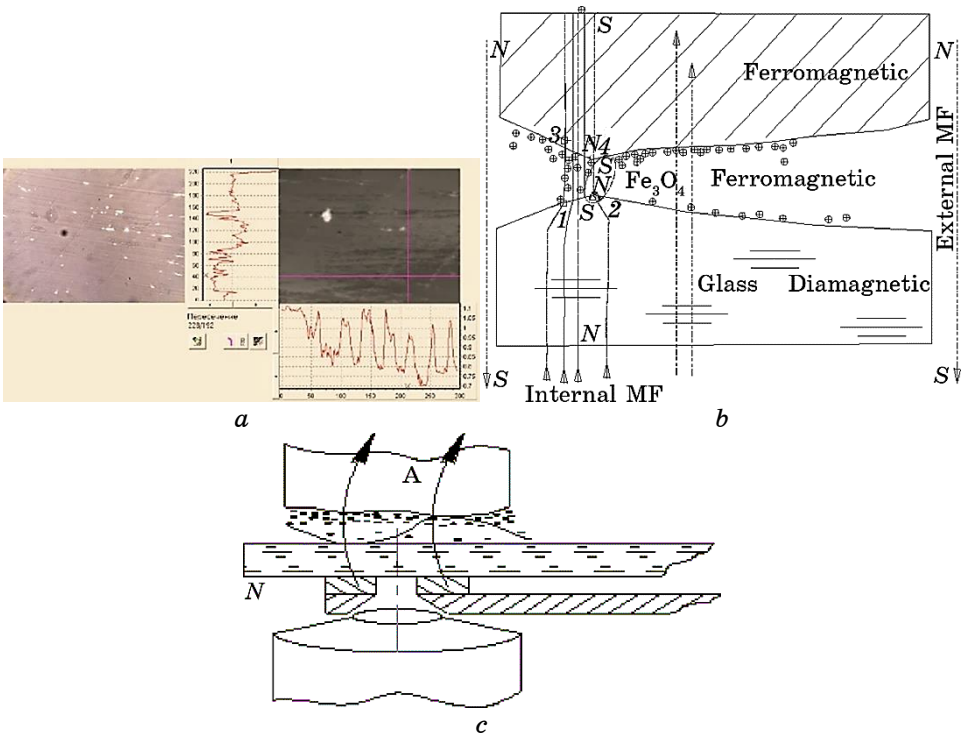

Fig. 6. Profilogram of the friction track on the glass (plane No. 3, Fig. 3) and topography of the surface with the direction of the external MF in the direction of *NS* glass (*a*), the scheme of the location of wear products in the directed MF near *NS* pole corresponds to plane No. 3 of Fig. 2 (*b*), scheme of the transition zone of friction between the sample and the glass in the resulting MF (*c*).

sistance [13]. Considering that WP conglomerates are oxides created under the influence of high local temperatures and pressures, they deposited on the glass, which is accompanied by the formation of protective oxide films on it (Fig. 7, *b*).

Further operation of the tribomechanical system during friction without lubrication on *NS* pole is accompanied by the formation of DS on the metal sample (steel 45). The dynamics of this process is shown in (Fig. 8), from which it can be seen that initially continuous protective films are formed (Fig. 8, *a*–*c*). After that, they are divided into separate areas, which are located on a significantly smaller plane (Fig. 8, *d*, *e*). This process ends with peeling of these films from their areas, and the appearance of dark oxide zones in their place, as well as powder from the products of their dispersion.

This mechanism of tribomagnetic contacting is subject to the laws of oxidative wear. When applying an external magnetic field directed from

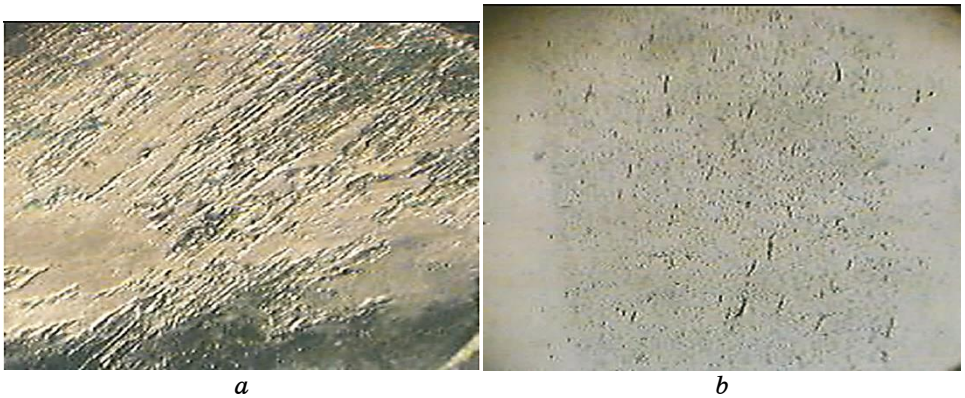

a *b*

Fig. 7. Appearance of the friction surface on *NS* pole: on the sample (*a*), on glass (*b*). The speed of friction is 0.1 m/s, normal load $P = 0.1$ kg, ×90.

NS pole toward the surface of the sample, dense oxide-type tribological films prevail [15] due to the presence of paramagnetic oxygen, which is drawn into the zone of frictional interaction by the magnetic field.

Thus, the process of formation of surface films with structural adaptation under the influence of MF consists in the gradual formation of DS, which, under the influence of the magnetic plastic effect, reduce their strength and increase the deformation component up to 15% [16, 17].

3.3. Analytical Substantiation of the Results of Tribological Research

Friction conditions are realized in the process of molecular-mechanical interaction in the surface layers of contacting bodies. The density of the energy balance is concentrated in the thin surface layers, therefore the properties of the deep layers of the material differ significantly, both structurally and energetically.

As the load increases, ACS, which takes part in the process of frictional interaction of the surfaces, expands, but its value does not exceed 0.1% of the total contact area. Energy costs are spent on overcoming the deformation components of the surface layers and creating an intermediate film with a defect-free structure at a minimum thickness [19]. In the contact zone, DS (Fig. 8, *a*) [20] are constantly being developed, which are sprayed on the friction surface, forming protective structures on it (Fig. 8, *b*–*e*). Further enrichment of the surface film with a fine fraction of DS ferromagnetic steel (Fig. 8, *f*) together with paramagnetic oxygen initiates chemical reactions, as a result of which, under the influence of frictional deformation and elevated temperature, different phase iron oxides are formed.

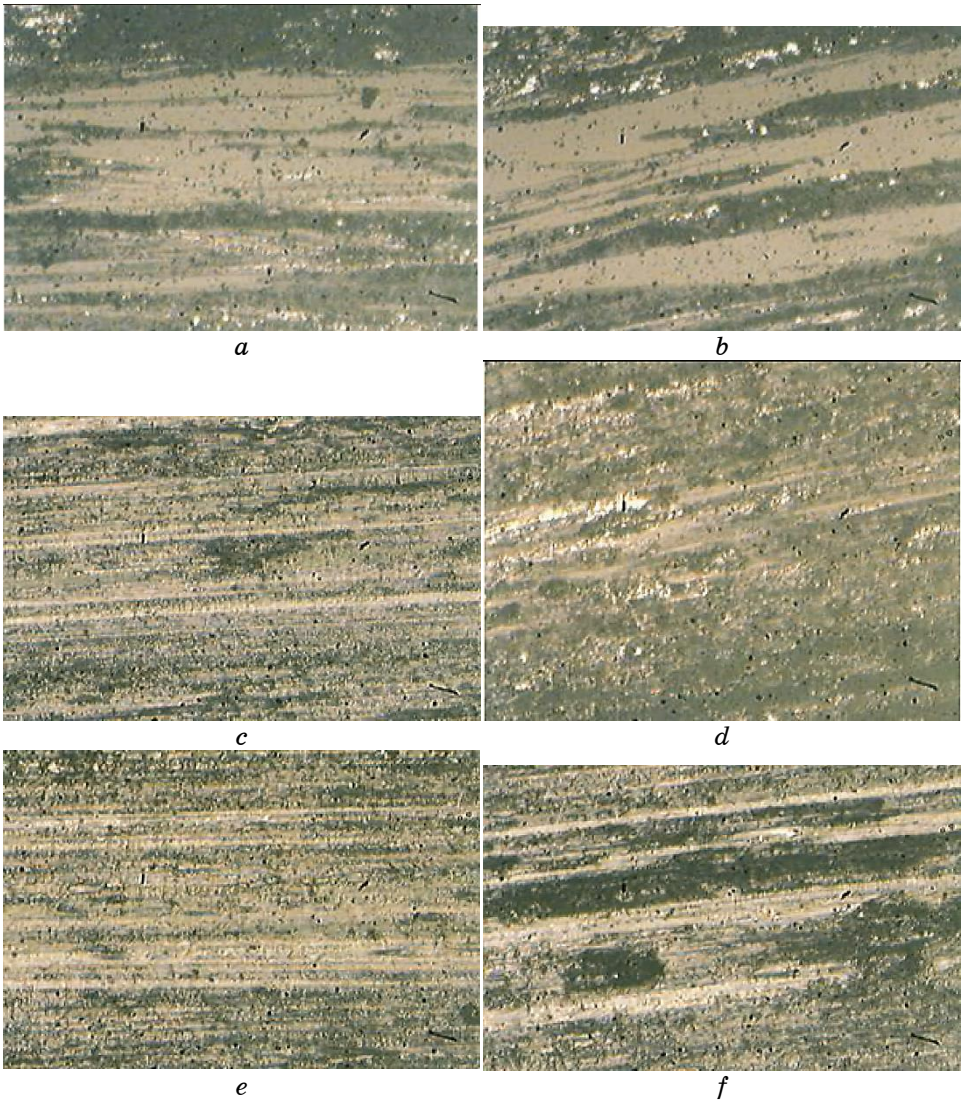

Fig. 8. Step-by-step formation of a protective oxide film on the surface of steel 45, when rubbing against a (model) counter body—glass, ×500 (photos taken in dynamic mode).

Determination of phase changes of the friction surface under the influence of MF was carried out by the method of quantitative phase analysis of the formation of the percentage content of the α-Fe phase in the ferrite-pearlite structure of steel 45 before and after exposure to MF (Table 1).

Depending on the direction of the field, changes in the atomic struc-

TABLE 1. Phase composition, texture coefficient and lattice periods of steel 45 after friction in a magnetic field.

No.	Material	Quantitative phase composition (% by mass), texture coefficient τ and period of the crystal lattice phases (nm)					Direction of MF (Fig. 2, *b*)
		α- Fe ferromagnetic component		f.c.c./γ- Fe paramagnetic component			
		a, nm	% mass	*a*, nm	τ	% mass	
1	St 45	0.2868	59.36	0.3701	0.48	40.64	N
2	St 45	0.2866	52.11	0.3693	0.49	47.89	*N*/*S*
3	St 45	0.2867	73.42	0.3694	0.40	26.58	*S*
4	St 45	0.2871	100				Without MF
5	St 45	0.28708	100				Without MF
		Volume-centred crystal lattice		Cubic face-centred lattice			

ture of steel 45 are observed in the zone of its active deformation and the effect of high temperature in the process of friction on the glass (Table 1).

In addition, under the influence of MF under conditions of magnetostriction, the parameter of the crystal lattice decreases in comparison to without MF $a = 0.28708–0.2872$ nm to $a = 0.2866–0.2868$ nm

The crystal lattice is formed from magnetically dependent elementary particles that are part of each atom. According to the Pauli principle, the spin of an electron (atom or molecule) in the quantum mechanical state always appears near the source of rotation [21]. Electrons occupy only specific discrete orbital positions around the nucleus, creating the atomic shell. The closer the electrons are to the nucleus, the stronger they are attracted to it, so more energy is needed to move them to other orbits.

The orbital closest to the nucleus can accommodate only two electrons with oppositely directed spins, which provides them with different quantum states. In the absence of an external magnetic field, the electron spins of the same level compensate for the total electric charge. The influence of the magnetic field directed parallel to the spin magnetic moments reduces the potential energy of the electron compared to the opposite direction of the field. As a result, the first electron will be in an energetically more stable state than the electron paired with it [22].

Since entropy ΔS is always positive, MF increases the energy of the system. The placement of the electron at the appropriate level must satisfy the condition of minimum potential energy. Due to this, the or-

bital radius decreases: the more energy a common pair of electrons has, the closer they must be to the nucleus of the atom, which, in turn, contributes to reducing the distance between lattice nodes. What, in particular, is indicated by the results of the analysis of the α-Fe phase composition (Table 1).

When the temperature increases ($T > 0$ K), the internal structure of a real crystal differs significantly from the ideal one. Defects can disrupt both the short- and long-range order of the crystal lattice (Fig. 8, *e*, *f*). The appearance of defects in a real crystal is explained by thermodynamic factors.

The stable state of the system is characterized by the minimum Gibbs energy: $\Delta G = \Delta H - T\Delta S$ at a certain concentration of defects in the crystal structure (depends on the material and environment). A certain amount of energy (ΔH) is spent on heating a defect-free crystal, which increases its Gibbs energy, which indicates the formation of defects on the friction surface (Fig. 8, *d*, *e*). Therefore, the enthalpy factor does not contribute to an increase in the number of defects. On the other hand, single vacancies in lattices (concentration of vacancies $\cong 10^{23}$ per 1 mole of substance) lead to a decrease in the total energy of the system and an increase in the entropy ΔS of the crystal. This is due to the presence of a significant number of nodes of the crystal lattice, where vacancies of this type can appear. The mathematical relationship between entropy and the probability of the formation of a vacancy is expressed by the formula $S = k\ln W$, where W is the probability of the formation of a single vacancy, which is proportional to the number of nodes of the crystal lattice of a given type, k is the Boltzmann constant. That is, the entropy factor ($T\Delta S$) at a temperature above 0 K leads to a decrease in the Gibbs energy of the crystal and contributes to the formation of defects in the crystal structure. Bearing in mind that it far exceeds the enthalpy factor, in which the energy is spent to form a single vacancy, the overall quantitative entropy parameter dominates, increasing the entropy of the crystal.

Since the temperature in ACS zones significantly exceeds point *A*1 (Fe–C state diagram), there is a change in the micro- and macrostructure of the steel, in particular, as a result of ferrite (α-Fe)–pearlite (α-Fe + Fe_3C) hardening the structure becomes martensitic. However, the energy state of the martensitic structure is lower than that of austenite (γ-Fe) [20]. The transition of α-Fe to γ-Fe begins when the steel 45 is heated to about 810°C and continues up to a temperature of about 1450°C, where the austenite structure is maintained. This indicates a significant energy advantage of the free energy in γ-iron over α-iron, which depends on the temperature level.

During the frictional interaction of surfaces in ACS zones, a sharp increase in temperature and high-speed deformation of the surface layer occur in an instant. The rupture of the zones during the move-

ment of the surfaces leads to their rapid cooling by removing heat into the metal matrix and the environment, which is accompanied by the creation of a structure with a tetragonal crystal lattice—martensite. Under the influence of MF and the processes of cooling and deformation of the rough steel surface, a more energy-intensive structure of austenite (γ-Fe) is formed in it at the level of *Ra* parameters.

When the magnetic field direction is changed, the ratio of the phase composition on the friction surface changes and the largest proportion of γ-Fe is observed in the bifurcation zone of ML at the position of sample B (see Fig. 2, *b*) (Table 1, position No. 2, N/S f.c.c./γ-Fe = 0.49), which indicates the most unstable structural state of the surface under the influence of the energy of the external MF.

Bearing in mind that friction is the relative movement of triboelements, and MF is imposed on both of their materials, it is necessary to create conditions under which the mechanical and chemical interaction of surfaces would have the least impact on the tribosystem. Investigating the kinetics of the formation of tribomagnetic films on friction surfaces, we come to the conclusion that the dynamics of the gradual build-up of surface films must be formed under the conditions of the influence of MF on a single material. That is, with a significant difference in the magnetic susceptibility of MF materials. Diamagnetic (glass) reduces the effect of magnetic field on the contact zone when paired with steel. The chemical interaction of iron with oxygen occurs in three stages. First, iron oxide FeO is formed, which contains 22.7% oxygen and also has the ability to dissolve in iron. Further accumulation of oxygen forms iron oxide Fe_2O_3 with an oxygen content of 30.06%. A mixture of FeO and Fe_2O_3 in MF has paramagnetic properties. The next stage takes place with the use of atomic oxygen to create Fe_3O_4 oxide, which contains 27.7% oxygen and acquires ferromagnetic properties in MF. Mechanochemical processes during rubbing of steel and glass under the influence of MP cause active deformation of the surface and accumulation of oxygen in the contact zone, which significantly affects the formation of surface protective films, the presence of which, according to the classification of B. I. Kostetskyi, corresponds to oxidative wear.

When the external MF is removed, the wear products are removed from the zone of frictional interaction. Under such conditions, steel wear occurs by the mechanism of friction without lubrication by the smooth surface of the glass.

The scientific novelty of the article lies in the disclosure of the wear mechanism of a ferromagnetic sample paired with glass (diamagnetic material) under the directed action of an external magnetic field. The effect of MF on the structural hierarchy of nanocoatings on the glass surface was determined. The basis of the structural transformations is the directed effect of MF on the deformation component, the mecha-

nism of the formation of WP and the formation of servo-vital films of a thin structure of tribological origin.

Practical Significance: monitoring of worn surfaces and restoration of the tribomechanical system; creation of conditions for reducing the wear of the tribomechanical system during operation.

4. CONCLUSIONS

1. An improved physical model of magnetic influence on the contact zone is characterized by the location of wear products around the friction zone and opens up the possibility of using them in the wear process to change the mechanism of formation of tribological protective nanocoatings. The location of nanocoatings is observed at the transitions between environments and materials of different magnetic nature along the direction of the magnetic field lines. On the basis of the analysis of the mechanism of impact of MF on the contact zone located perpendicular to the passage of the lines of force, the process of placement of wear products on the surface of the glass in the direction of MF from the sample to the glass in *SN* pole is considered.
2. The direction of the magnetic field affects the ratio of the phase composition of the friction surface, and the largest fraction of γ-Fe is observed in the bifurcation zone of the magnetic field lines (N/S f.c.c./γ-Fe = 0.49), which passes during an unstable state of the surface structure under dynamic by changing the energy of the external MF. In this way, the parameters of the crystal bed are reshaped from volume-centred α-Fe to face-centred γ-Fe (zone of the austenite structure). The rearrangement of the crystal bed takes place due to the rapid heating of the friction surface at the points of ACS with subsequent, rapid cooling (more than 1000°C/s) of the contact zone and the influence of the mobility of dislocations when the electronic structure changes under the influence of MF. The created formation of a finely dispersed structure significantly increases the tribological parameters of the surface.
3. The conditions of influence of MP on the tribological properties of ferromagnetic materials require further research.

REFERENCES

1. B. N. Mordyuk, O. O. Mikosyanchik, and R. G. Mnatsakanov, *Metallofiz. Noveishie Tekhnol.*, **42**, No. 2: 175 (2020) (in Ukrainian).
2. O. A. Mikosyanchik and R. G. Mnatsakanov, *J. Friction Wear*, **38**: 279 (2017).
3. B. M. Mordyuk and O. O. Mikosyanchik, *Metallofiz. Noveishie Tekhnol.*, **39**, No. 6: 795 (2017) (in Ukrainian).
4. M. M. Svyryd, S. M. Zanko, S. M. Zadniprovska, V. G. Parashchanov, and L. B. Priymak, *Prystriy dlya Doslidzhennya Materialiv na Tertya ta*

Znoshuvannya [A Device for Researching Materials on Friction and Wear Utility], Utility Model Patent of Ukraine No. 36600 (Published October 27, 2008) (in Ukrainian).
5. B. I. Kostetskiy, I. G. Nosovskiy, L. I. Bershadskiy et al., *Poverkhnostnaya Prochnost' Materialov pri Trenii* [Surface Strength of Materials under Friction] (Kiev: Tekhnika: 1976) (in Russian).
6. M. M. Svyryd, O. Y. Sydorenko, V. V. Kozlov, and S. V. Cherepov, *Metallofiz. Noveishie Tekhnol.*, **44**, No. 3: 365 (2022).
7. P. P. Savchuk, V. P. Kashitsky, M. D. Melnichuk, and O. L. Sadova, *Kompozytni ta Poroshkovi Materialy* [Composite and Powder Materials] (Ed. P. P. Savchuk) (Lutsk: FOP Telitsyn O. V.: 2017) (in Ukrainian).
8. S. P. Gubin and Yu. A. Koksharov, *Inorganic Mater.*, **38**: 1085 (2002).
9. K. M. Zhumaliev and N. T. Amanova, *Stabilization of Magnetic Nanoparticles* (2009).
10. D. N. Baranovskyy, *East European J. Enterprise Technologies*, **3**, No. 8: 28 (2009) (in Ukrainian).
11. H. Zaidi, M. Amirat, J. Frene, T. Mathia, and D. Paulmier, *Wear*, **263**, Iss. 7–12: 1518 (2007).
12. E. V. Charnaya, Cheng Tien, and Min Kai Lee, *Phys. Solid State*, **52**: 1539 (2010).
13. H. Shi, S. Du, C. Sun, C. Song, Z. Yang, and Y. Zhang, *Materials*, **12**, Iss. 1: 45 (2018).
14. M. M. Svyryd, O. Yu. Sydorenko, I. V. Smirnov, and S. V. Khizhnyak, *Problems of Frictions and Wear*, No. 2: 80 (2021).
15. D. M. Nuruzzaman and M. A. Chowdhury, *American J. Mater. Sci.*, **2**, No. 1: 26 (2012).
16. E. V. Darinskaya, *Magnitoplasticheskiy Effekt: Osnovnyye Svoistva i Fizicheskie Mekhanizmy* [Magnetoplastic Effect: Main Properties and Physical Mechanisms] (Thesis of Disser. for Dr. Sci. (Phys.-Math.)) (Moskva: Institut Kristallografii im. A. V. Shubnikova RAN: 2004) (in Russian).
17. M. O. Vasiliev, *Usp. Fiz. Met.*, **8**, No. 1: 65 (2007) (in Russian).
18. V. I. Alshits, E. V. Darinskaya, O. L. Kazakova, E. Yu. Mikhina, and E. A. Petrzhik, *Mater. Sci. Eng. A*, **234–236**: 617 (1997).
19. M. M. Svirid, A. P. Kudrin, S. M. Zadniprovska, A. M. Khimko, and O. Y. Yakobchuk, *Sposib Vidnovlennya Poverkhni Tertya v Impul'snomu Magnitnomu Poli* [Method of Surface Rubbing in a Pulsed Magnetic Field], Utility Model Patent of Ukraine No. 45918 (Published November 25, 2009) (in Ukrainian).
20. M. M. Svyryd, I. A. Kravets', H. A. Volosovych, S. M. Zan'ko, and L. B. Pryymak, *Mashynoznavstvo*, No. 8: 28 (2010) (in Ukrainian).
21. O. I. Tovstolytkin, M. O. Borovyy, V. V. Kurylyuk, and Yu. A. Kunyts'kyy, *Fizychni Osnovy Spintroniky* [Physical Foundations of Spintronics] (Vinnytsia: Nilan-LTD: 2014) (in Ukrainian).
22. I. M. Laptev and O. O. Parkhomenko, *Metallofiz. Noveishie Tekhnol.*, **42**, No. 11: 1583 (2020).

Metallophysics and Advanced Technologies
Металофіз. новітні технол.
Metallofiz. Noveishie Tekhnol.
2025, vol. 47, No. 1, pp. 25–38
https://doi.org/10.15407/mfint.47.01.0025
Reprints available directly from the publisher

PACS numbers: 61.05.cp, 61.66.Dk, 61.66.Fn, 61.72.jd, 81.05.Je, 81.20.Ev, 81.20.Wk

Mechanical Alloying of Equimolar TiC–VN and TiN–VN Blends

N. M. Bilyavina, V. V. Kuryliuk, V. V. Dibrov, and A. M. Kuryliuk

Taras Shevchenko National University of Kyiv,
60 Volodymyrska Str.,
UA-01033 Kyiv, Ukraine

The investigation of step-by-step sampled products of mechanical alloying (MA) of two equimolar mixtures of TiC–VN and TiN–VN sintered with high-energy ball mill is conducted implicating number of methods of x-ray diffractometry (x-ray phase analysis, x-ray structural analysis, investigation of crystallite sizes and microstresses in the crystal lattice, *etc.*). As shown, the crystal structures of VN, TiN, and TiC undergo significant structural transformations during MA treatment. Specifically, part of the vanadium or titanium atoms migrate from their localization to tetrahedral pores under the impact load and part of those atoms leave their positions in the lattice and form separate clusters in the reaction zone of the milled powder. These processes lead to substantial accumulation of crystallographic point defects in phase structures presented by vacancies in metal sublattices of VN, TiN, TiC and substitutional atoms of vanadium or titanium in the crystal lattice. Overall, the increase of the portion of mentioned point defects is accompanied by the increase of microstresses in phases. Substantial portion of accumulated vacancies and some fraction of the vanadium- and titanium-atoms' clusters formed in the reaction zone of the milled powder create preconditions for further formation of mutual solid substitutional alloys. As shown, the impact of the MA treatment is decreased in the VN → TiN → TiC series that can be explained with such phase characteristics as dissociation energy, elasticity modulus, and thermal conductivity. The MA-activated dispersed (crystallite size up to 20 nm) powder mixture of TiC–VN acquired in the work

Corresponding author: Vasyl' Vasyl'ovych Kurylyuk
E-mail: kuryliuk@knu.ua

Citation: N. M. Bilyavina, V. V. Kuryliuk, V. V. Dibrov, and A. M. Kuryliuk, Mechanical Alloying of Equimolar TiC–VN and TiN–VN Blends, *Metallofiz. Noveishie Tekhnol.*, **47**, No. 1: 25–38 (2025). DOI: 10.15407/mfint.47.01.0025

may be recommended as alloying additive for medical titanium composites to increase the functional characteristics.

Key words: mechanical alloying, carbide, nitride, crystal structure, x-ray diffraction.

З використанням комплексу методів Рентґенової дифрактометрії (Рентґенової фазової аналізи, рентґеноструктурної аналізи, визначення розмірів кристалітів і мікронапружень у кристалічній ґратниці тощо) проведено дослідження покроково відібраних продуктів механохемічної (МХ) синтези у високоенергетичному планетарному млині двох еквімолярних сумішей TiC–VN і TiN–VN. В результаті показано, що в ході МХ-оброблення кристалічні структури VN-, TiN- і TiC-фаз зазнають істотних структурних перетворень, а саме, під дією ударного навантаження в структурах фаз частина атомів Ванадію чи то Титану переміщується зі своїх положень у тетраедричні пори, а частина зазначених атомів залишає відповідні ґратниці з формуванням окремих кластерів у реакційній зоні млина. Ці процеси ведуть до істотного накопичення в структурах фаз точкових дефектів у вигляді вакансій у металевих підґратницях VN, TiN, TiC й у вигляді занурених у кристалічні ґратниці атомів Титану чи то Ванадію. Збільшення долі зазначених точкових дефектів супроводжується збільшенням у фазах мікронапружень. В цілому наявність великої долі накопичених вакансій і певної долі кластерів атомів Ванадію та Титану, сформованих у реакційній зоні млина, створює передумови для подальшого утворення взаємних твердих розчинів заміщення. Показано, що ступінь впливу МХ-оброблення зменшується в ряду VN → TiN → TiC, що цілком пояснюється такими характеристиками цих фаз як величина енергії дисоціяції, модуль пружности та величина термічної провідности. Одержана в роботі МХ-активована дрібнодисперсна (розмір кристалітів — до 20 нм) суміш TiC–VN може бути рекомендованою в якості леґувальної добавки для поліпшення функціональних характеристик стопів медичного титану.

Ключові слова: механохемічна синтеза, карбід, нітрид, кристалічна структура, Рентґенова дифракція.

(Received 27 June, 2024; in final version, 20 November, 2024)

1. INTRODUCTION

Transition metal compounds such as VN and TiN nitrides as well as TiC carbide belong to the class of hard refractory metal materials according to their promising physical and chemical properties. Their high melting points, ultra-high hardness, outstanding electrical and thermal conductivity, optical properties and superior chemical stability made these compounds implemented in many applications, especially in electrochemical devices, environmental remediation, gas sensing, photocatalysis, applied ceramics, and medicine [1–5]. In particular, TiN, VN

nitrides and TiC carbide have found their successful application as individual additives to improve the functional properties of ceramics [6–10], as well as titanium alloys used for medical applications [11, 12].

*Pc*BN ceramics (60% vol. of *c*BN nitride) with binders containing well-known TiC and TiN phases combined with VN nitride [13, 14] revealed the superior performance in mechanical properties. The properties of these materials was shown to be improved to an extent, it was credited to the existence of solid solutions formed in the TiC–VN and TiN–VN binders during the HPHT (high pressure, high temperature) sintering process (7.7 GPa, 1900–2350°C). More specifically, under certain HPHT sintering modes (Ti, V)(C, N) and (V, Ti)(N, C) mutual solid solutions form in the *c*BN–TiC–VN–Al composite (ratio in % vol. as 60:17.5:17.5:5) [15] as well as (Ti, V)N and (V, Ti)N mutual solid solutions form in the *c*BN–TiC–VN–Al composite (60:17.5:17.5:5) [16].

Mechanical alloying (MA) is one of the effective methods of synthesis, which can additionally provide the formation of solid solutions, moreover, in the nanocrystalline state. The study of the TiN and VN nitrides interaction, which occur at mechanical alloying of the equimolar TiN–VN mixture in a planetary mill, reveals the formation of the (Ti, V)N and (V, Ti)N mutual solid solutions, as it occurs during HPHT sintering of this mixture [16]. The mutual solid solutions forming under mechanical alloying of TiC–ZrC mixtures were studied in [17, 18]

The purpose of this work is detailed study of the kinetics of interaction of VN nitride with TiN nitride or with TiC carbide during mechanical alloying of the equimolar TiC–VN and TiN–VN mixtures in a high-energy planetary mill.

2. EXPERIMENTAL/THEORETICAL DETAILS

Two equimolar TiC–VN and TiN–VN mixtures of starting powders containing VN and TiN or TiC were placed into two steel vials for further ball milling in a high-energy planetary mill. Steel balls (diameter of 10 mm) were used for the milling with the balls to powder mass ratio of 20:1. The regime was chosen as 10 min of treatment and 20 min of cooling. The temperature of the working area in the reaction zone did not exceed 100°C during experiment; the ball-mill rotation speed was 1400 rpm.

Phase transformations in TiC–VN and TiN–VN mixtures processed have been studied by x-ray diffraction methods on the test samples selected after every 60 min of milling. XRD data was collected with ДРОН-3М automatic diffractometers (CuK_α radiation) in a discrete mode under the following scanning parameters: observation range $2\theta = 20°–100°$, step scan of 0.05° and counting time per step at 3 s. The original software package [15], including full complex of standard Rietveld procedures, has been used for analysis and interpretation of

the x-ray diffraction patterns obtained, namely, determination of both peak positions and integral intensities of the Bragg reflections by means of full profile analysis; carrying out qualitative and quantitative phase analysis using the least square method for lattice parameters refinement; testing of the structure models proposed and refining crystal structure parameters (including coordinates of atoms, atomic position filling, texture, *etc.*); calculation of the parameters of the real structure of the individual phases (coherent block sizes and microdeformation values).

3. RESULTS AND DISCUSSION

The results of the XRD phase analysis reveal that the test samples of both TiC–VN and TiN–VN mixes contain initial VN and TiC or TiN phases with a small amount of steel ball material contamination in the final products (Fig. 1). However, the lattice parameters of these phases differ from those in the initial blends (Table 1). The characterization of changes in lattice parameters during MA treatment ($a(t)$ values) was controlled by the relative value of their distortions, which were calculated according to the formula: $\varepsilon[\%] = 100(a_t - a_0)/a_0$, where a_t is the value of the lattice parameter at a certain t milling time, and a_0 is in the initial mixture (Table 1, Fig. 2). It can be seen that the crystal lattice distortions of TiN and VN nitrides are much greater than those ones of TiC carbide.

To clarify the causes of changes in ε values (Fig. 2), first the refinement of the crystal structures of TiC, TiN and VN phases within the

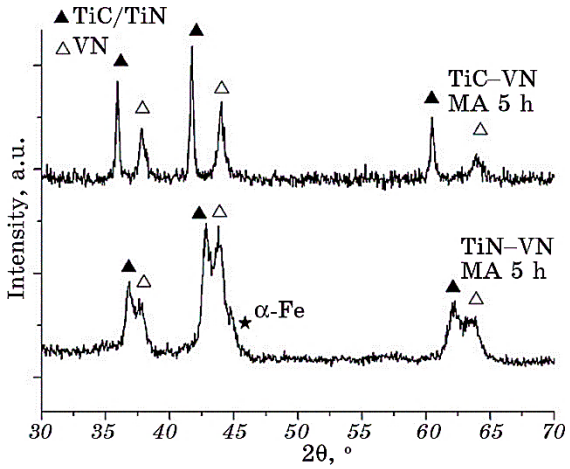

Fig. 1. Diffraction patterns of the TiC–VN and TiN–VN equimolar blends after 5 hours of treatment in a planetary mill.

TABLE 1. Parameters, distortions and microdeformations of the lattices of the TiC, TiN and TiC phases. It is impossible to determine the value of microdeformation of the lattices of nitrides existing in the TiN–VN blend due to the reflections overlap of these phases (Fig. 1).

Milling time t, h	Lattice parameter a, nm	Lattice distortion ε, %	Microdeformation $\Delta d/d$, %	Lattice parameter a, nm	Lattice distortion ε, %	Microdeformation $\Delta d/d$, %
TiC–VN blend						
	TiC carbide			VN nitride		
0	0.43252(3)	0	0	0.41251(6)	0	0
1	0.43246(3)	–0.0139	0.13(1)	0.41197(6)	–0.1302	0.20(4)
2	0.43242(4)	–0.0231	0.15(2)	0.41142(7)	–0.2642	0.40(5)
3	0.43240(6)	–0.0277	0.14(2)	0.41089(9)	–0.3927	0.46(8)
4	0.43266(9)	0.0324	0.12(1)	0.4112(1)	–0.3176	0.39(4)
5	0.43271(9)	0.0439	0.00(2)	0.4116(1)	–0.2254	0.25(2)
TiN–VN blend						
	TiN nitride			VN nitride		
0	0.42440(5)	0	–	0.41251(6)	0	–
1	0.42401(8)	–0.0919	–	0.41230(9)	–0.0509	–
2	0.42293(9)	–0.3464	–	0.41207(9)	–0.1067	–
3	0.4221(1)	–0.5419	–	0.4117(1)	–0.2061	–
4	0.4218(1)	–0.6126	–	0.4120(1)	–0.1139	–
5	0.4215(1)	–0.6833	–	0.4135(1)	0.2400	–

NaCl type structure model (space group $Fm3m$ (No. 225)) has been conducted: 4 Ti or 4 V in 4*a* 0 0 0; 4 N or 4 C atoms in 4*b* 0.5 0.5 0.5. As a result of these calculations, it was shown that the 4*a* position, which is occupied by metal atoms, becomes vacant at almost complete filling of the 4*b* position with nitrogen or carbon atoms. However, the reliability factor R_B exceeded the value of 0.03.

To improve the value of the R_B factor, several structural models have been proposed and tested for the TiC, TiN, VN phases existing in MA treated TiC–VN and TiN–VN mixtures. The best correlation between the calculated and experimental intensities values of the diffraction pattern reflections were obtained for the models presented in Table 2 ($R_B < 0.01$).

The obtained results (Table 2) indicate that the crystal structure of the VN nitride undergoes certain transformations during the MA processing. More specifically, some vanadium atoms leave the metal sub-

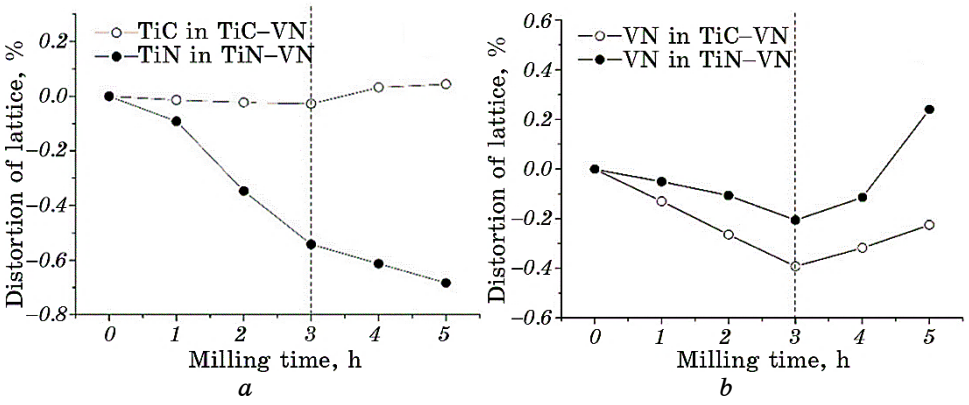

Fig. 2. Distortion of the crystal lattices of TiC, TiN and VN phases during MA treatments of TiC–VN blend (*a*) and TiN–VN blend (*b*) in a planetary mill.

lattice, which accommodates the V(1) atoms and the available Vac V(1) vacancies (position 4*a*). One part of the displaced atoms is located in the tetrahedral pores of the VN nitride lattice (V(2) atoms in the 4*e* position), and the second part of these atoms leaves the VN nitride with the formation of separate vanadium clusters in the reaction zone. Figure 3, *a* illustrates the transformation of the crystal structure of the VN nitride during the MA treatment. As it can be seen on Fig. 3, *a*, the main vanadium atoms in the VN nitride are surrounded by 6 nitrogen atoms at a distance of 0.206 nm (1 octahedron), and the distance of a possible migration of a vanadium atom into a tetrahedral pore (3 tetrahedron) is 0.180 nm (the arrow in Fig. 3, *a*), respectively.

Similar migrations caused by MA treatment are also characteristic of titanium atoms in TiN nitride and TiC carbide (Fig. 3, *b*). However, unlike to the cubic structure of VN, the best result was obtained for the model of the rhombohedral structure (presentation of the structures of TiN and TiC along their body diagonal, Table 2), in which the tetrahedral pore (tetrahedron 3-Ti(2)Ti(1)$_4$) becomes deformed, and the migration distances of titanium atoms vary from ≈ 0.18 nm (three positions) to ≈ 0.24 nm (one position).

Obviously, the difference in the possible positions, intended for placement of the vanadium atoms (regular tetrahedron 3-V(2)V(1)$_4$) or titanium atoms (a triangle 3-Ti(2)Ti(1)$_3$, in fact), results from the peculiarities of directionality atomic bonds in vanadium or titanium.

According to the results of crystal-structure refinement, which was carried out within the framework of the proposed models (Table 2), it was determined the quantitative content of titanium or vanadium both in the metal sublattice of the structures (positions 3*a* and 4*a*) and in the tetrahedral pores where these atoms migrated under the shock

load. The data obtained in this manner for TiC and VN phases that exist in the MA treated TiC–VN blend are presented in Fig. 4. It should be noted that analogical plots for the phases that exist in the MA treated TiN–VN blend are of the same kind. The total metal content in each of the VN, TiN, and TiC phases is presented in Fig. 5.

A detailed XRD study of the crystal structures of the VN, TiN, TiC phases, which exist in the step-by-step milled products, revealed certain tendencies in the kinetics of mechanochemical synthesis of equimolar TiC–VN and TiN–VN mixtures under MA processing in a planetary mill, as well as in the nature of the interaction of the phases existing in these blends.

Moreover, accumulation of defects in the metal sublattices of TiC, TiN, VN phases occurs mainly in the first stage of MA processing (up

TABLE 2. Crystal structure data for VN and TiC or TiN phases existing in TiC–VN and TiN–VN blends treated for 5 h in planetary mill.

TiC carbide in TiC–VN blend					
Atom	Position	Occupation	*X*	*Y*	*Z*
Ti(1)	3*a*	0.778(1)	0	0	0
Ti(2)	3*a*	0.222(1)	0	0	0.368(1)
C	3*a*	1.000(1)	0	0	0.5
Vac in Ti(1)	3*a*	–0.028(2)	0	0	0
Space group				*R*3*m* (No. 160)	
Lattice parameters *a*, *c* nm				0.3057(2), 0.7482(2)	
Total isotropic *B* factor, nm^2				$2.56(3)\cdot10^{-2}$	
Calculated content, at.%				49.3 Ti + 50.7 N	
Reliability factor				$R_B = 0.008$	
VN nitride in TiC–VN blend					
Atom	Position	Occupation	X	Y	Z
V(1)	4*a*	0.980(2)	0	0	0
V(2)	4*e*	0.020(2)	0.25	0.25	0.25
N	4*b*	1.000(1)	0.5	0.5	0.5
Vac in V(1)	4*a*	–0.126(4)	0	0	0
Space group				*F*–43*m* (No. 216)	
Lattice parameter *a* nm				0.4116(1)	
Total isotropic *B* factor, nm^2				$3.69(1)\cdot10^{-2}$	
Calculated content, at.%				47.0 V + 53.0 N	
Reliability factor				$R_B = 0.004$	

Continuation Table 2.

TiN nitride in TiN–VN blend					
Atom	Position	Occupation	X	Y	Z
Ti(1)	3*a*	0.783(1)	0	0	0
Ti(2)	3*a*	0.217(1)	0	0	0.356(1)
N	3*a*	1.000(1)	0	0	0.5
Vac in Ti(1)	3*a*	–0.034(2)	0	0	0
Space group				*R*3*m* (No. 160)	
Lattice parameters *a*, *c* nm				0.2983(1), 0.7313(2)	
Total isotropic *B* factor, nm^2				$2.25(3)\cdot10^{-2}$	
Calculated content, at.%				49.1 Ti + 50.9 N	
Reliability factor				$R_B = 0.008$	
VN nitride in TiN–VN blend					
Atom	Position	Occupation	X	Y	Z
V(1)	4*a*	0.955(2)	0	0	0
V(2)	4*e*	0.045(2)	0.25	0.25	0.25
N	4*b*	1.000(1)	0.5	0.5	0.5
Vac in V(1)	4*a*	–0.227(4)	0	0	0
Space group				*F*–43*m* (No. 216)	
Lattice parameter *a*, nm				0.4135(2)	
Total isotropic *B* factor, nm^2				$2.55(1)\cdot10^{-2}$	
Calculated content, at.%				43.6 V + 56.4 N	
Reliability factor				$R_B = 0.009$	

to 3 hours), as can be seen in Fig. 4. In this case, one part of the metal atoms leaves the crystal lattice forming the atomic clusters in the reaction zone of the milled powder, while the other part of the atoms migrates into tetrahedral pores of the crystal structure. At the first stage of milling, there is also a gradual increase in the microdeformation of the crystal lattice, which correlates with an increase in its distortions (Table 2, Fig. 5) as well as with an increase in the dislocation density (it is impossible to determine the value of microdeformation of the lattices of nitrides existing in the TiN–VN blend due to the reflections overlap of these phases (Fig. 1)).

After 3 hours of milling of TiC–VN and TiN–VN mixtures in a planetary mill, the process of active migration of vanadium atoms into tetrahedral pores of VN stops, at the same time the process of migration of titanium atoms into tetrahedral pores of TiC and TiN slows down

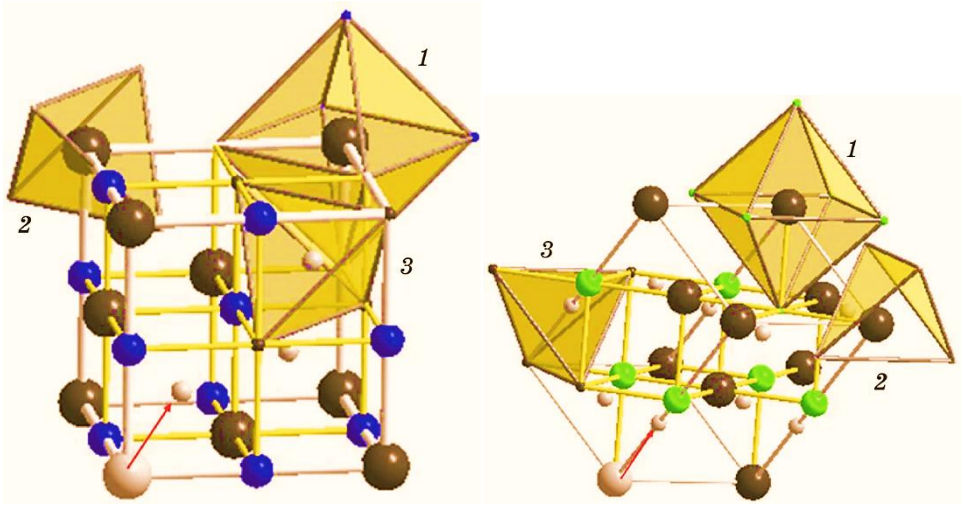

Fig. 3. Arrangement of the atoms in the structures of the phases that exist in TiC–VN and TiN–VN mixtures treated in a planetary mill for 5 hours: VN nitride (*a*), TiN nitride or TiC carbide (*b*). Atoms marked as follow: metal atoms are large black circles, nitrogen or carbon atoms are medium-coloured circles, and metal atoms jumped from the main position are small light grey circles. Polyhedra: *1*—$Me(1)N_6$ or *1*—$Ti(1)C_6$, *2*—$Me(1)Me(2)_4$, *3*—$Me(2)Me(1)_4$.

(Fig. 4). This causes a decrease in the deformation of the crystal lattices of TiN, VN nitrides and TiC carbide (Fig. 6), although their lattice parameters continue to change (Table 1, Fig. 2). In our opinion, this may be caused by the beginning of processes wherein the available vacancies in the metal sublattices of these phases are filled with free atoms of titanium or vanadium that have entered the reaction zone of the milled powder. Unfortunately, due to the closeness of the atomic scattering functions of titanium and vanadium, it is impossible to determine correctly the amount of dissolved metal by XRD method. But the formation of mutual solid solutions is evidenced by an increase in the parameters of the VN lattices (the size of titanium atom is large than vanadium one), as well as the decrease in the parameters of the TiC and TiN lattices which goes on despite the decrease in the amount of vacancies (Table 1, Fig. 4).

As it is known, the basis of mechanochemical synthesis is the mechanical processing of solid mixtures, during which grinding and plastic deformation of substances occur. Under the effect of applied mechanical stresses, the process of formation of point defects is initiated in the material, which leads to partial destruction of the crystal structure accompanied by creation of active centres for subsequent chemical

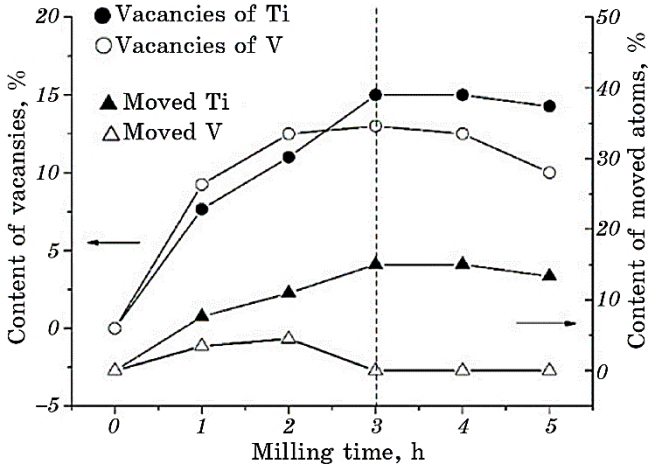

Fig. 4. Plots of dependences of the amount of available vacancies in the metal sublattice of the TiC and VN phases existing in the MA treated TiC–VN mixture (circles), as well as of the amount of atoms that have moved into the tetrahedral pores (triangles).

reactions. These are the processes, which occur during the MA processing of TiC–VN and TiN–VN blends in a high-energy planetary mill. More specifically, they are as follow.

1. At the first stage of MA synthesis (up to 3 hours of processing), there is an active accumulation of point defects, namely, an increase in vacancies in the metal sublattice of crystal structure as well as an increase in the number of atoms in its internodes (Fig. 4).

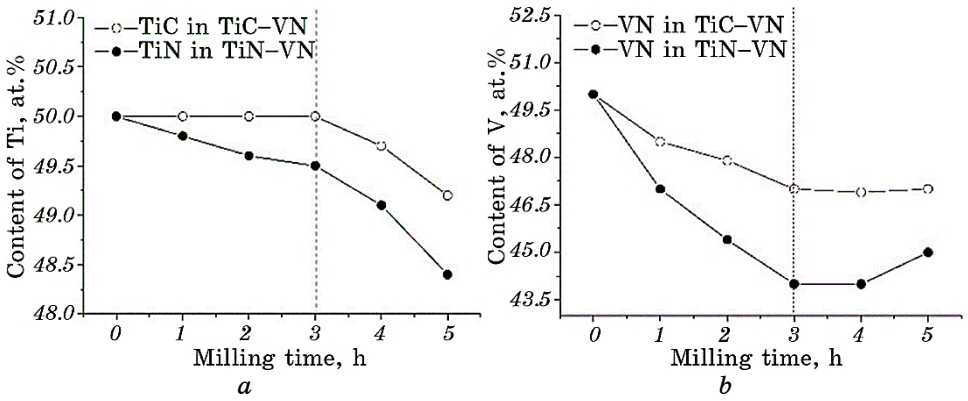

Fig. 5. Dependence of the content of metals in the crystal structures of TiC, TiN, VN phases on the MX processing time of TiC–VN and TiN–VN mixtures in a planetary mill.

TABLE 3. Some characteristics of the phases included in the TiC–VN and TiN–VN charges.

Phase	Melting point T, °C	Dissociation energy D_0, kJ/mole	Young's modulus, GPa	Thermal conductivity, W/(m·K)
TiC	3260	1388	494	7
TiN	2930	1261	251	29
VN	2050	1197	210	60–120

At the same time, clusters of vanadium and titanium atoms appear in the reaction zone of the milled powder, which have left the structures of the TiN and VN phases, as it evidenced by a shift in their composition (Fig. 5). Moreover, the process of forming titanium clusters during MA treatment of the TiC–VN mixture is slower. The accumulation of defects is accompanied by an increase in microstresses of crystal lattices and by an increase in the dislocation density (Fig. 6).

2. At the second stage of MA synthesis (after 3 hours of processing), the stress field created at the first stage as a result of the accumulation of point defects is starting to gradually relax (Fig. 6). It is probably due to a decrease in the number of atoms placing in the internodes (Fig. 4). Obviously, the interatomic bonds of these atoms in the structures are somewhat weaker, which contributes to the mass transfer to the reaction zone of the milled grains. The set of available factors (a high proportion of vacancies in the metal sublattice of the phases, as well as some proportion of the atomic clusters formed, Fig. 4) facilitate the creation of active centres for the further formation of mutual solid solutions. It is evidently illustrated by exceeding the lattice value of the VN nitride over its value in the initial charge (Fig. 2, *b*).

3. The extent of exposure of mechanochemical processing on the VN or TiN nitrides and on the TiC carbide, used in these experiments, is fully explained by the characteristics of these phases given in Table 3. Namely, the VN nitride was shown to be the most susceptible to MA treatment (especially in the presence of TiN but not of TiC). It can be explained by the increase in the values of the dissociation energy, melting temperature, and Young's modulus as VN $\rightarrow$ TiN $\rightarrow$ TiC. It should also be noted that the decrease in thermal conductivity as VN $\rightarrow$ TiN $\rightarrow$ TiC also influences on the extent of exposure of the MA synthesis process of TiC–VN and TiN–VN blends.

4. CONCLUSIONS

Using a wide complex of XRD methods, the products of mechanochem-

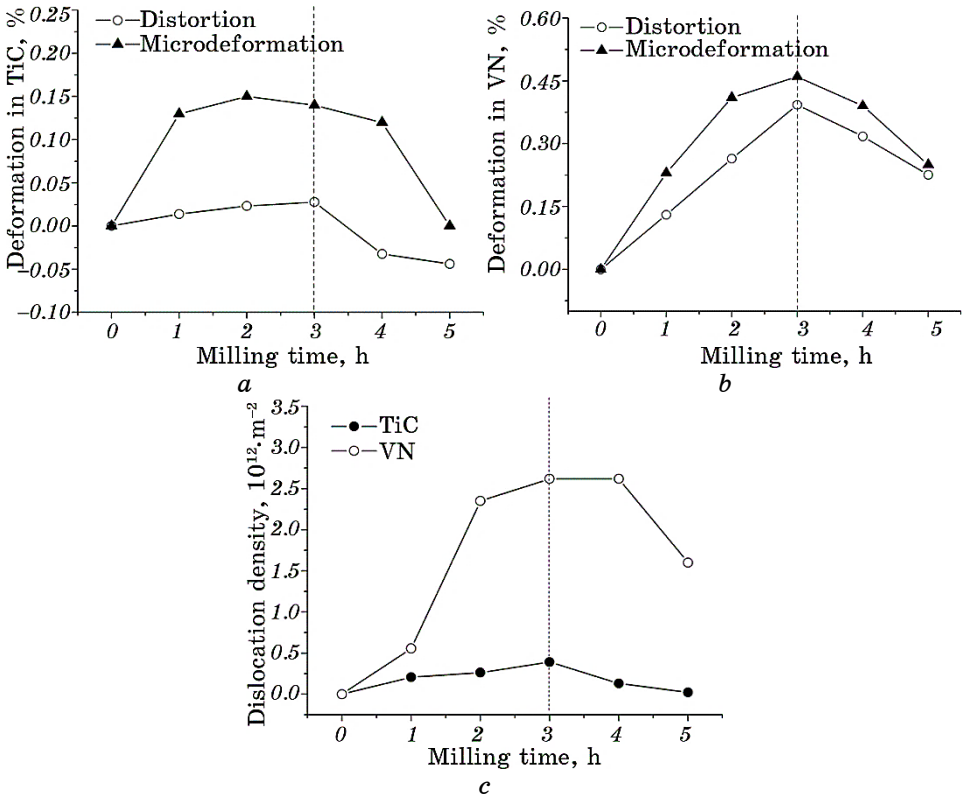

Fig. 6. Dependences of distortions and microdeformations of the crystal structures of TiC (*a*) and VN (*b*) phases as well as dislocation density (*c*) on the milling time of the TiC–VN mixture in a planetary mill.

ical processing of equimolar TiC–VN and TiN–VN mixtures were studied systematically. Studies of the phase transformation kinetics were performed and revealed the following.

1. The crystal structures of VN, TiN, TiC phases undergo certain transformations during the MA processing. Under the impact load, some vanadium or titanium atoms move into the tetrahedral pores of the corresponding lattices, and some of these atoms leave the lattices of nitrides or carbide forming the separate clusters in the reaction zone of the powder.

2. Accumulation of the indicated point defects in the crystal lattices of VN, TiN, TiC phases occurs abundantly at the first stage of MA processing (up to 3 hours of treatment). This process is accompanied by a gradual increase in microstresses values and an increase in the dislocation density.

3. At the second stage of the MA process (after 3 hours of treatment),

the stress field created at the first stage as a result of point-defects' accumulation is gradually starting to relax. The presence of a large proportion (share) of vacancies in the structures and a certain proportion (share) of formed atomic clusters in the reaction zone of the powder contribute to the creation of active centres for further formation of mutual solid solutions on their basis.
4. The extent of exposure of mechanochemical processing on the VN, TiN, TiC phases decreases in the series VN → TiN → TiC, which is fully explained by such characteristics of these phases, as values of the dissociation energy, the Young's modulus, the thermal conductivity.
5. Fine-crystalline (crystallite size up to 30 nm) MA activated powders of an equimolar TiC–VN mixture will be tested as functional additives to improve the properties of medical titanium alloys.

This work has been supported by Ministry of Education and Science of Ukraine within the project 24БФ051-01 'Synthesis of biocompatible metal-ceramic composites to improve the wear resistance of medical instruments and titanium-based implants'.

REFERENCES

1. H. O. Pierson, *Handbook of Refractory Carbides and Nitrides: Properties, Characteristics, Processing and Applications* (William Andre: 1996).
2. B. Mazumder and A. L. Hector, *J. Mater. Chem.*, **19**, Iss. 27: 4673 (2009).
3. L. Toth, *Transition Metal Carbides and Nitrides* (Academic Press: 2014).
4. S. A. Rasaki, B. Zhang, K. Anbalgam, T. Thomas, and M. Yang, *Prog. Solid State Chem.*, **50**: 1 (2018).
5. M. Mhadhbi and M. Driss, *J. Brilliant Eng.*, **2**: 1 (2021).
6. P. Patsalas, N. Kalfagiannis, S. Kassavetis, G. Abadias, D. V. Bellas, Ch. Lekka, and E. Lidorikis, *Mater. Sci. Eng. R*, **123**: 1 (2018).
7. M. Idrees, A .Mukhtar, Ata-ur-Rehman, S. M. Abbas, Q. Zhang, and X. Li, *Mater. Today Commun.*, **27**: 102363 (2021).
8. S. Mahadik, S. Surendran, J. Y. Kim, G. Janani, D. K. Lee, T. H. Kim, J. K. Kim, and U. Sim, *J. Mater. Chem. A*, **10**, Iss. 28: 14655 (2022).
9. A. Aramian, Z. Sadeghian, M. Narimani, N. Razavi, and F. Berto, *Int. J. Refract. Metals Hard Mater.*, **115**: 106320 (2023).
10. K. V. Slipchenko, V. Z. Turkevich, V. M. Bushlya, and J.-E. Stehl, *Porodorazrushayushchiy i Metaloobrabatyvayushchiy Instrument—Tekhnika i Tekhnologiya ego Izgotovleniya i Primeneniya*, Iss. 22: 254 (2019) (in Ukrainian).
11. H. C. Man, S. Zhang, F. T. Cheng, and T. M. Yue, *Scripta Mater.*, **44**, Iss. 12: 2801 (2001).
12. W. H. Wei, Z. N. Shao, J. Shen, and X. M. Duan, *Mater. Sci. Technol.*, **34**, Iss. 2: 191 (2018).
13. K. Slipchenko, V. Bushlya, D. Stratiichuk, I. Petrusha, A. Can, V. Turkevich, and F. Lenrick, *J. Eur. Ceram. Soc.*, **42**, Iss. 11: 4513 (2022).
14. K. V. Slipchenko, I. A. Petrusha, V. Z. Turkevich, D. A. Stratiichuk,

V. M. Slipchenko, N. M. Bilyavina, D. V. Turkevich, V. M. Bushlya, and J.-E. Stah, *Metallofiz. Noveishie Tekhnol.*, **41**, No. 4: 1599 (2019) (in Ukrainian).
15. N. M. Belyavina, V. Z. Turkevich, A. M. Kuryliuk, D. A. Stratiichuk, and O. I. Nakonechna, *Dopovidi Natsional'noyi Akademiyi Nauk Ukrayiny*, No. 4: 33 (2024) (in Ukrainian).
16. N. Belyavina, O. Nakonechna, A. Kuryliuk, P. Kogutyuk, D. Stratiichuk, and V. Turkevich, *Mater. Proc.*, **14**, Iss. 1: 16 (2023).
17. T. G. Avramenko, A. M. Kuryliuk, O. I. Nakonechna, and N. N. Belyavina, *Metallofiz. Noveishie Tekhnol.*, **44**, No. 6: 713 (2022).
18. N. N. Belyavina, V. Z. Turkevich, A. M. Kuryliuk, D. A. Stratiichuk, O. I. Nakonechna, T. G. Avramenko, and P. P. Kogutyuk, *Dopovidi Natsional'noyi Akademiyi Nauk Ukrayiny*, No. 6: 54 (2022) (in Ukrainian).
19. M. Dashevskyi, O. Boshko, O. Nakonechna, and N. Belyavina, *Metallofiz. Noveishie Tekhnol.*, **39**, No. 4: 541 (2017).

Metallophysics and Advanced Technologies
Металофіз. новітні технол.
Metallofiz. Noveishie Tekhnol.
2025, vol. 47, No. 1, pp. 39–55
https://doi.org/10.15407/mfint.47.01.0039
Reprints available directly from the publisher

PACS numbers: 05.40.Fb, 05.60.Cd, 66.30.-h, 68.35.Fx, 81.05.Bx, 81.70.Bt

Method for Determining the Diffusion and Drift Components of Anomalous Mass Transfer in Metals under External Influences

O. V. Filatov, Y. O. Pavliuk, V. F. Mazanko, S. Ye. Bogdanov, D. S. Gertsriken, Ye. I. Bogdanov, and S. P. Vorona

G. V. Kurdyumov Institute for Metal Physics, NAS of Ukraine,
36 Academician Vernadsky Blvd.,
UA-03142 Kyiv, Ukraine

Within the framework of this investigation based on experimental data, the approach to determine the process parameters of anomalous mass transfer in solid state using isotopic technique under external influences is developed. This approach is used to determine the process parameters of mass transfer in high-entropy alloys (HEA) AlFeNiCoCuCr and steel S235 (analogue of steel 3) after electric-spark alloying and subsequent impact treatment. Radioactive ^{60}Co isotope is used as indicator of mass transfer process. As shown in this work using the developed method, the predominant mechanism of mass transfer in condition of electric-spark alloying and mechanical impact is the directed movement of atoms carried away by mobile dislocations in S235 and HEA. Calculating the mean and root-mean-square displacements of atoms, the force acting on each atom and the mobility of ^{60}Co atoms in S235 under mechanical-impact processing are determined. As shown, the Einstein–Smoluchowski equation may be used to determine the atoms mobility under external influences and the process of anomalous mass transfer, if D_T to replace by D_{ef}.

Key words: anomalous mass transfer, radioactive ^{60}Co isotope, atoms mobility, external influence, high-entropy alloys, steel S235.

В рамках даного дослідження на основі експериментальних даних розроб-

Corresponding author: Oleksandr Valentynovych Filatov
E-mail: filatov@imp.kiev.ua

Citation: O. V. Filatov, Y. O. Pavliuk, V. F. Mazanko, S. Ye. Bogdanov, D. S. Gertsriken, Ye. I. Bogdanov, and S. P. Vorona, Method for Determining the Diffusion and Drift Components of Anomalous Mass Transfer in Metals under External Influences, *Metallofiz. Noveishie Tekhnol.*, **47**, No. 1: 39–55 (2025). DOI: 10.15407/mfint.47.01.0039

лено підхід для визначення параметрів процесу аномального масоперенесення у твердих тілах з використанням методу радіоактивних ізотопів за умов зовнішніх впливів. Даний підхід використано для визначення параметрів процесу масоперенесення у високоентропійних стопах (ВЕС) AlFeNiCoCuCr і криці S235 (аналог криці 3) після електроіскрового леґування та подальшого ударного оброблення. Як індикатор масоперенесення, використовували радіоактивний ізотоп ^{60}Co. За допомогою розробленої в даній роботі методики показано, що переважним механізмом масоперенесення в умовах електроіскрового леґування та механічного удару в S235 і ВЕС є спрямований рух атомів, що захоплюються рухомими дислокаціями. Розрахунком середнього та середньоквадратичного зміщень атомів визначено силу, що діє на кожен атом, і рухливість атомів ^{60}Co в S235 в умовах механічного ударного впливу. Показано також, що рівняння Айнштайна–Смолуховського можна використовувати для визначення рухливости атомів в умовах зовнішніх впливів і процесу аномального масоперенесення, якщо зробити заміну D_T на D_{ef}.

Ключові слова: аномальне масоперенесення, радіоактивний ізотоп ^{60}Co, рухливість атомів, зовнішній влив, високоентропійні стопи, криця S235.

(Received 11 September, 2024; in final version, 22 October, 2024)

1. INTRODUCTION

The study of the diffusion mechanism features, mass transfer and structural changes under external influences is one of the main fundamental problems in solid-state physics. In scientific works [1, 2], the theoretical approaches to determining the diffusion parameters and anomalous diffusion are described.

1.1. Definition of Anomalous Mass Transfer and Anomalous Diffusion

The phenomenon of tracer atoms penetration to macroscopic depths (tens and hundreds of microns) in solids in an extremely short time compared to ordinary diffusion, called 'anomalous mass transfer', was discovered in the study of processes occurring in metals under pulsed vacuum welding conditions [3–5]. The mass transfer was called 'anomalous' due to the fact that under conditions of high-speed plastic deformation of crystalline solids (deformation rate $\varepsilon' > 1\ \text{s}^{-1}$), the migration rate of self and impurity atoms in them exceeds by several orders of magnitude the rate of stationary diffusion mass transfer and diffusion in the liquid phase [4]. The term 'accelerated non-stationary mass transfer' is also used for this phenomenon. Usually, diffusion obeys the central limit theorem [6], which implies that the sum of random jumps of atoms will approach a stable distribution that has the same shape as a normal distribution (according to Gauss):

$$\rho_N(x) = \frac{1}{\sqrt{2\pi}} e^{-x^2/2}. \quad (1)$$

There is a term 'anomalous diffusion' when the probability distribution profile (which has a normal Gaussian form) according to the central limit theorem is violated, as well as the usual laws of Brownian motion following from this theorem [1, 6]. The anomalous diffusion behaviour manifest in Eq. (2) is intimately connected with the breakdown of the central limit theorem (3), caused by either broad distributions or long-range correlations. Anomalous diffusion is found in a wide diversity of systems, its hallmark being the non-linear growth of the mean squared displacement in the course of time [2]:

$$< x^2(t) > \sim D_\alpha t^\alpha, [D_\alpha] = \mathrm{cm}^2\mathrm{s}^{-\alpha}, \quad (2)$$

$$< x^2(t) > \sim D_1 t, [D_1] = \mathrm{cm}^2\mathrm{s}^{-1}. \quad (3)$$

According to the value of the anomalous diffusion exponent α, defined in Eq. (2), one usually distinguishes several domains of anomalous transport, as shown in Fig. 1.

The Cauchy distribution has no moments (they are infinite), but it is a stable distribution:

$$\rho_c(x) = \frac{1}{\pi} \frac{1}{x^2 + 1}. \quad (4)$$

It does have a well-defined full width half maximum. The Cauchy distribution is also known as a Lorenz distribution. Therefore, there is no first moment (mean) even though the function is symmetrical about $x = 0$. Likewise, the variance is infinite. This distribution has tails (Fig. 2).

The consequences of violating the central limit theorem are that tails dominate eventually in a sum of randomly generated variables. The

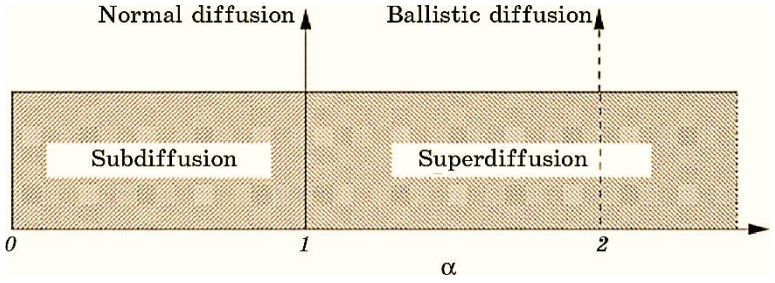

Fig. 1. Different domains of anomalous diffusion, defined through the mean squared displacement, equation (2), parametrized by the anomalous diffusion exponent α: subdiffusion for $0 < \alpha < 1$, normal Brownian diffusion $\alpha = 1$, superdiffusion for $\alpha > 1$. Another special case is ballistic motion $\alpha = 2$ [2].

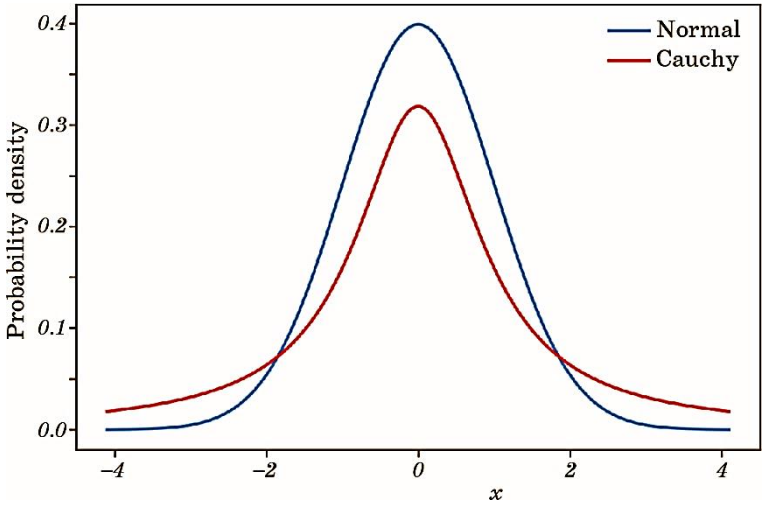

Fig. 2. A comparison of the shape of the normal (1) and Cauchy distributions (4) [6].

standard deviation of a distribution of random walkers increases limitless. A random walker obeys something like a Cauchy distribution if every once in a while, the walker takes a big jump. Moreover, every once in a longer time, the walker takes even bigger jump and so on in a self-similar (fractal) or power law form. This parameter leads to superdiffusion.

If jumps are made, on the contrary, from time to time, with stops, which each time become even longer in time, then, this leads to the phenomenon of subdiffusion (Fig. 3) and is related to a phenomena called intermittency that is sometimes seen in chaotic dynamical systems [2].

That way, the graphical representation $\rho(x, t)$ for the subdiffusive case $\alpha = 1/2$ is obtained, which is displayed in Fig. 3. In comparison to the standard Gaussian result, shown in Fig. 4, the pronounced cusps of the subdiffusive propagator are distinct.

1.2. Formulation of the Problem

The currently existing theoretical approaches consider the effect of the length of the atom jump and the duration of stops and are based on the dependence of the concentration distribution on time. In contrast, the experiment contains data on the distribution of concentration as function from depth.

In this paper, it is proposed a method for determining the parameters of diffusion and mass transfer based on experimental data on the distribution of concentration over depth, which does not require studying the time dependence. In addition, the method makes it possible to

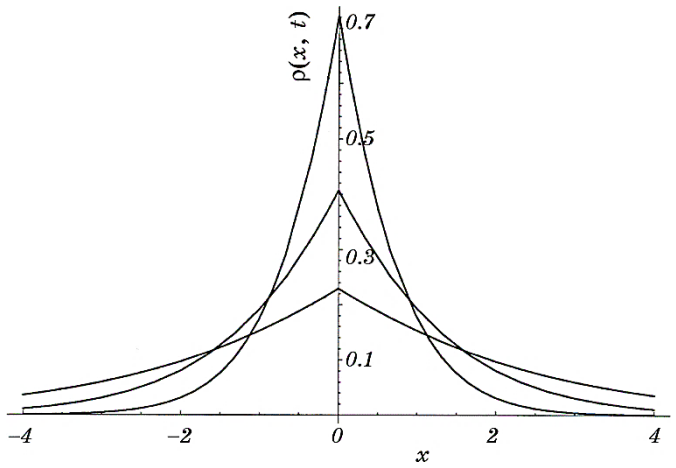

Fig. 3. $\rho(x,t) = (4D_\alpha t^\alpha)^{-1/2} \sum_{n=0}^{\infty} (-1)^n (n!\,\Gamma(1-\alpha(n+1)/2))^{-1} (x^2 / D_\alpha t^\alpha)^{n/2}$ as a form of the probability distribution function for subdiffusion with the parametric exponent of anomalous diffusion $\alpha = 1/2$, drawn for the consecutive times $t = 0.1, 1, 10$. The graph is characterized by the cusp shape [2].

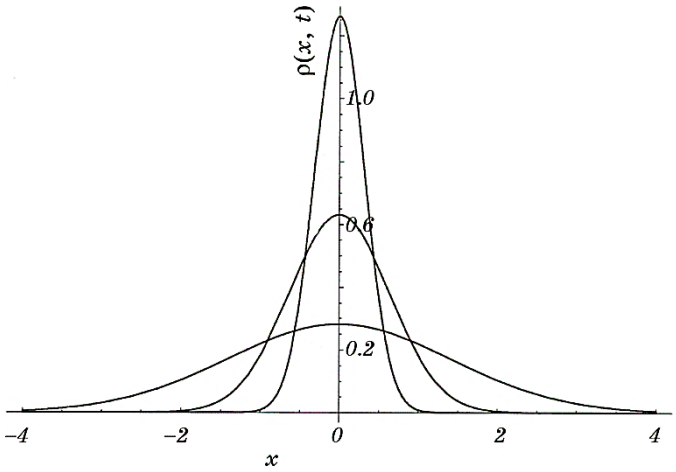

Fig. 4. Form of the probability distribution function $\rho_N(x, t)$ for Brownian diffusion $\alpha = 1$ for the times $t = 0.05, 0.2, 1$. The much smoother shape close to the origin sets this solution apart from the subdiffusive counterpart drawn in Fig. 3 [2].

determine the contribution of the driving force due to external action, and thereby distinguish the diffusion component and the drift contribution to the total mass transfer.

To achieve this purpose, the following tasks were solved in the work.

1. A method for calculating the effective diffusion coefficient (mass transfer) is proposed, taking into account the diffusion component and directional motion under the action of a driving force.

2. The diffusion coefficients and the average rate of atomic migration for different materials are compared.

3. The contribution of each of the different types of influences to the mass transfer process during complex processing is highlighted.

4. On the basis of the data obtained, conclusions were drawn about the mechanisms of mass transfer.

2. EXPERIMENTAL AND THEORETICAL DETAILS

2.1. Description of Materials

The following materials were selected as research materials: widely used S235 steel (analogue of steel 3) with a b.c.c. structure and a challenging high-entropy alloy (HEA) AlFeNiCoCuCr with a mainly b.c.c. structure, the diffusion processes in which are noticeably lower compared to diffusion in its components [7].

The samples were a steel cylinder 10 mm high and 10 mm in diameter with an electrolytically deposited layer of the radioactive ^{60}Co isotope 0.3–0.5 μm thickness. A layer of high-entropy AlFeNiCoCuCr alloy 30 μm thick was deposited onto the isotope layer by electrospark alloying (ESA) under the following conditions: current strength $I = 2.2$ A, processing time $\tau = 120$ s and 180 s, respectively. The operating frequency was 50 Hz. The standard industrial plant 'ELITRON-22' was used for the formation of electrospark coatings.

The next type of external influence on the samples was impact treatment with a load of $m = 10.5$ kg falling from a height $h = 1$ m.

To obtain the concentration distribution of ^{60}Co isotope, the autoradiography and layer-by-layer removal techniques were used [8, 9].

3. RESULTS AND DISCUSSION

3.1. Diffusion and Mass Transfer Parameters in S235 and HEA after Electric-Spark Alloying

To determine the time t, the diffusion calculation takes into account the electric-spark alloying (ESA) processing frequency, which is 50 Hz. The duration of one contact of the tip of the electrode with the treated surface is of 0.01 s and 0.01 s cooling between touches. The radius of the spot formed by the transferred drop of cathode material on the surface of S235 is of 0.35 mm. Taking into account the thermal

conductivity of steel b, the depth of the heated layer is $z = 2(bt)^{1/2} = 0.5$ mm. Using these data, it is possible to estimate that the cooling time of sample surface to $0.7T_{\text{melt}}$ is of $\cong 0.015$ s. It takes about 30–50 pulses to form one spot. The time between pulses can be neglected from the point of view of the influence on the temperature since the heated volume in the intervals between pulses does not have time to cool below $0.7T_{\text{melt}}$ before the next pulse. Thus, the exposure time of a thermal pulse for the formation of one spot during ESA is

$$t = \tau / N = 1.2 \text{ s}. \tag{5}$$

where N is equal to 100, the number of spots with an alloying substance on the surface of the sample, τ is equal to 120 s, the overall time of processing the surface of the sample.

The application of the random walks theory to the diffusion of ^{60}Co atoms as a result of ESA leads to equations analogous to the first and second Fick's laws, who adapted the heat conduction equations derived by Fourier [10]. If we take into account that the source of the diffusing substance consists of a finite amount of impurity, then, the solution of the second Fick equation has the form

$$C(x,t) = \frac{Q_0}{\sqrt{\pi Dt}} \exp\left(-\frac{x^2}{4Dt}\right); \tag{6}$$

from the experimental data, a graph of the dependence of $\ln C(x, t)$ on x^2 was plotted, and according to formula

$$\ln C(x,t) = \ln \frac{Q_0}{\sqrt{\pi Dt}} - \frac{x^2}{4Dt}, \tag{7}$$

a straight line was obtained: the ratio

$$\frac{1}{x^2} \ln\left(\frac{C}{C_0}\right) = \text{const}. \tag{8}$$

This explains the bulk nature of diffusion, which prevails over grain boundary diffusion. At the same time, the exponent '2' at x indicates that the application of the second Fick's law is justified in this case due to the fact that the contribution to the total flux from the drift tends to '0'. The exponent at x, which would differ from '2', would indicate that the process of atoms transfer under pulsed impacts occurs under the action of a significant driving force, which is comparable in magnitude to $k_B T$ [5]:

$$\text{tg}\alpha = -\frac{1}{4Dt}. \tag{9}$$

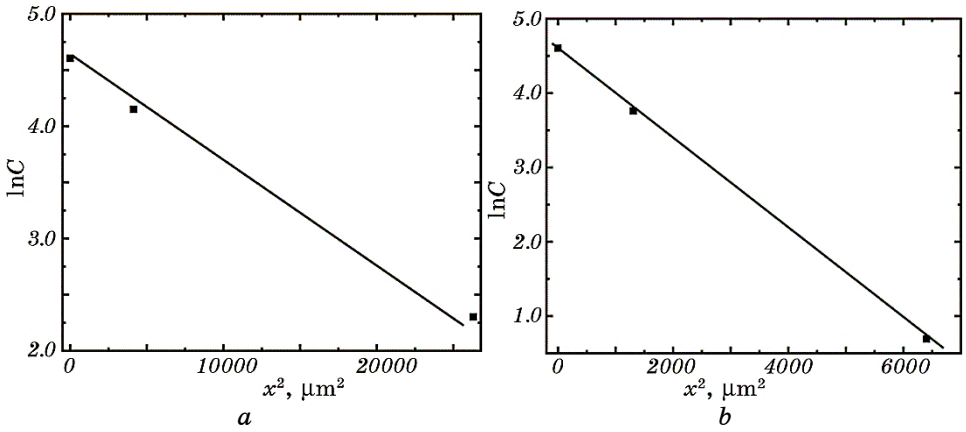

Fig. 5. Dependence graph according to $\ln C = x^2$: S235 after ESA (*a*), for HEA after ESA (*b*).

Knowing tgα from Figure 5 and diffusion time t, the mass transfer coefficients D_M after ESA were found. For S235, $D_M = 4.3 \cdot 10^{-8}$ m²/s, and for HEA, $D_M = 3.1 \cdot 10^{-9}$ m²/s.

The diffusion coefficient is 14 times higher in S235, than in HEA, which is consistent with the idea that the driving force of mass transfer is dislocations that move the radioactive isotope through the mechanism of capture and transfer of an interstitial atom [11, 12]. In HEA, due to the presence of atoms of different sizes in the composition, elastic displacements will occur during the movement of a dislocation and an additional 'friction' force will arise. The local Burgers vector **b** varies both in magnitude and in direction [13]. Thus, mass transfer is going slower in HEA, than in S235.

3.2. Diffusion and Mass Transfer Parameters in S235 and HEA under Impact Deformation

Determination of the diffusion time t as a result of impact (2.3 ms) at sample S235 + HEA after ESA processing was carried out by the occurrence of an electromotive force (EMF) from the electrical-signal oscillogram according to the method described in Ref. [14], since the estimated diffusion time corresponds to the plastic deformation time (Fig. 6).

As follows from the oscillograms of electrical signals in Fig. 6, the plastic deformation time is 2 ms. During this time, diffusion proceeds predominantly by the interstitial mechanism, which is realized while the dislocations are moving intensively [15, 16]. The role of vacancies in the process of plastic deformation is low due to the high activation energy and due to the low mobility of vacancies [17]. Therefore, the

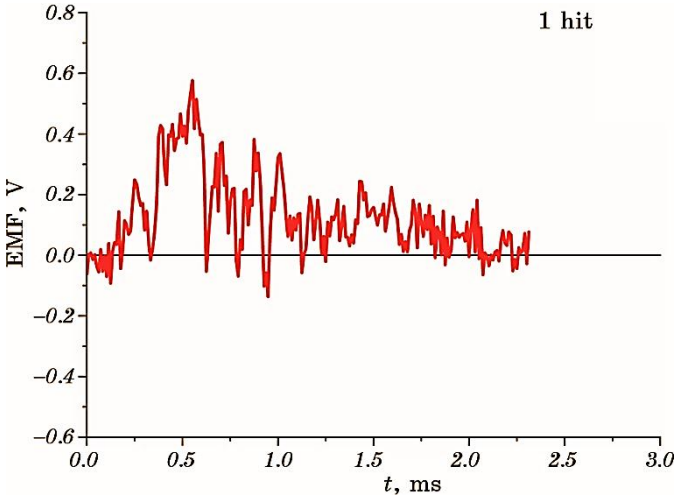

Fig. 6. Dependence graph of the electrical signals from loading time at sample S235 + HEA after ESA processing.

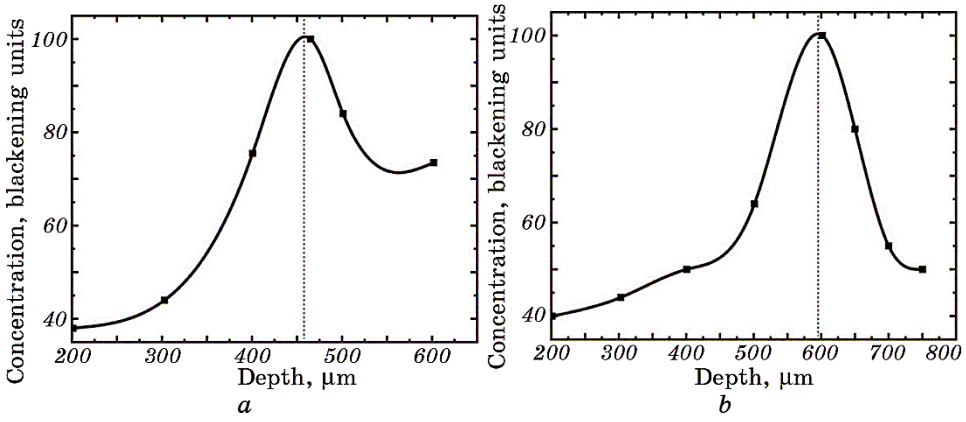

Fig. 7. Normalized concentration distribution of ^{60}Co isotope in depth in S235 (to the left of the maximum) and in HEA (to the right): after ESA (*a*), after complex processing (*b*).

contribution of vacancies to mass transfer by the random walk mechanism at 300 K can be neglected.

The impact load contribution to the mass transfer process in S235 and HEA during complex processing (ESA with next impact processing) is separated out.

As a result of the directed impact load, the dependence of ^{60}Co concentration on depth changed (Fig. 7): the concentration maximum of the radioactive tracer shifted to the right, which can be explained by

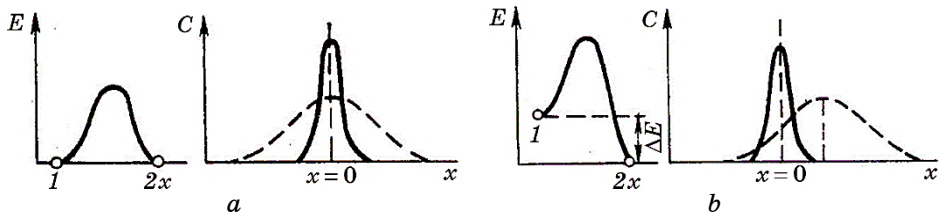

Fig. 8. Energy diagrams of potential barriers and corresponding concentration curves: without external forces (*a*), with external forces [18] (*b*).

the appearance of an external force, which leads to a symmetry breakdown of the potential barrier for atoms (Fig. 8, *b*). The probability of atoms transition in the direction of the force is more than in the opposite direction. Therefore, the symmetry of the concentration curve is broken; its maximum is shifted [18].

Since the total amount of the diffusing substance did not change due to the impact, but the concentration distribution over the depth (x coordinate) changed, in order to distinguish the contribution to the mass transfer of the impact load, the following was done:

1. The position of the maximum (100%) was found, which was taken as the 0-reference point by co-ordinate (Fig. 7, *b*),

2. Depths were found, at which concentrations of 90%, 80%, *etc.* are observed for each of the graphs in Fig. 7, *b*,

3. The subtraction from the data of the graph in Fig. 7, *b* of the data from Fig. 7, *a* was carried out according to the corresponding x coordinate found.

In this way, a displacement of x points was obtained, which correspond to the same relative concentrations before and after the impact, which is the result of the impact. This procedure was applied to each of the branches in the graphs of Fig. 7, which characterize the penetration of the diffusant into S235 and into HEA. The subtraction result characterizes the role of mass transfer in the impact process, is shown in Fig. 9. Thus, from the mass transfer under complex processing (ESA with next impact processing), the contribution of impact treatment was separated out.

When the contribution of drift to the total mass transfer is significant, the resulting distribution of concentrations may differ significantly from that predicted by the theory of diffusion by the mechanism of random walks. Dependence (5) of the natural logarithm of the C/C_0 concentration on the square of the depth x^2, as in the case of diffusion for random walk mechanism, at ESA is not fulfilled, and the values fall on a straight line with power exponents for x: where $n = 1.5$ and $n = 1$ for S235 and HEA, respectively (Fig. 10). That is, the concentration distribution is described by the dependence $C(x)/C_0 = \exp(-ax^n)$ [19].

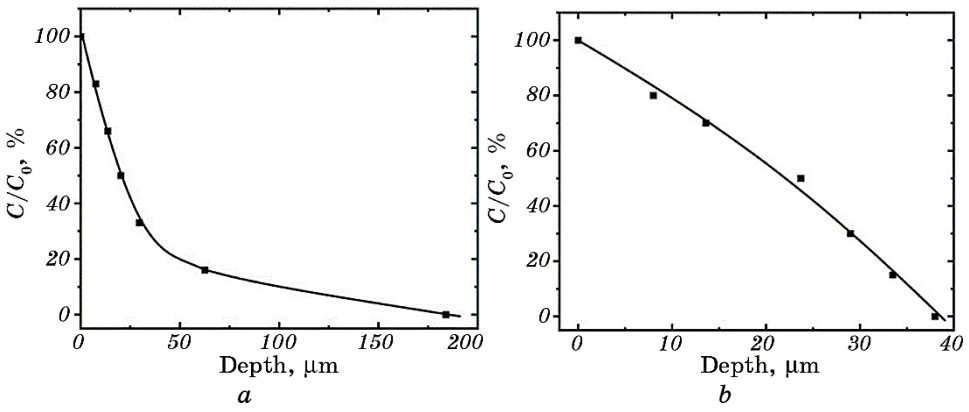

Fig. 9. Distribution of ^{60}Co concentration in depth in S235 (*a*) and HEA (*b*) under impact processing.

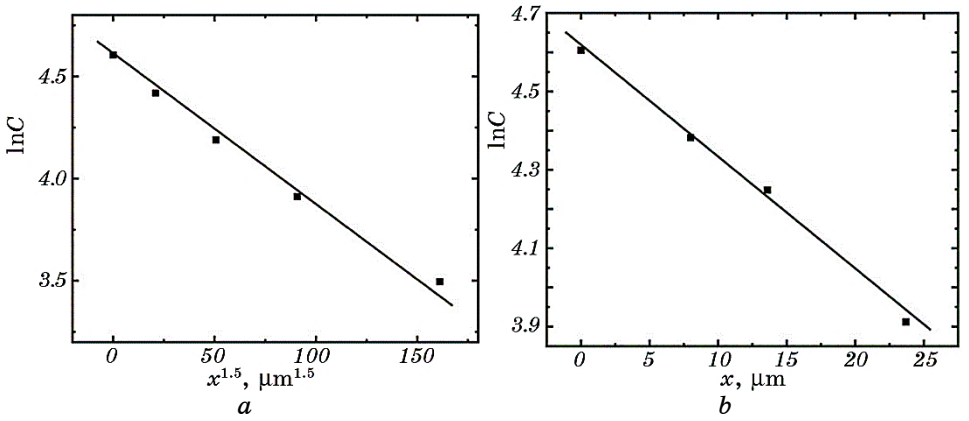

Fig. 10. The graphs of dependence $C(x)/C_0 = \exp(-ax^n)$: S235, $n = 1.5$ (*a*) and HEA, $n = 1$ (*b*) after impact processing.

This indicates an anomalous mass transfer and the unsuitability of the Fick's second law application.

According to formulas (9), (10), it can be found the mean and mean-square shifts as the first and second normalized statistical moments. The sources [1,2] show the possibility of using these moments to describe and find diffusion parameters, including anomalous ones, by the mechanism of random walks.

In this paper, for the first time, the graphical method of finding such statistical moments and determining the parameters of anomalous mass transfer on the basis of experimental data on the distribution of concentration is proposed. From the processed experimental

data (Fig. 9) of concentration distribution, the general (due to both diffusion and drift) mean and root-mean-square displacement for the ^{60}Co penetration into S235 and HEA is found out:

$$< x >= \frac{\int (C / C_0) x dx}{\int (C / C_0) dx}, \tag{10}$$

$$< x^2 >= \frac{\int (C / C_0) x^2 dx}{\int (C / C_0) dx}. \tag{11}$$

To find $<x>$ by the formula (10), the task was solved graphically (Fig. 11). In a similar way, when plotting the concentration distribution, but depending on x^2, $<x^2>$ was found using the formula (11).

To find $<x>$ by the formula (10, it is used the data approximation from Fig. 9, *a* for S235 by the rectangles' method with a variable subinterval. The same way $<x>$ was found by the formula (10) for HEA (the graphs are similar both for S235 and HEA) using the data approximation from Fig. 9, *b* (Table 1).

To describe mass transfer and comparison with diffusion by the ran-

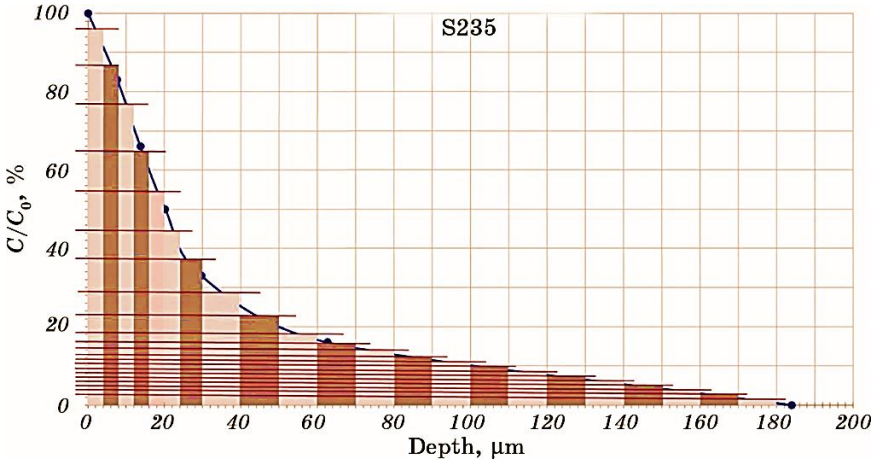

Fig. 11. An example of data approximation from Fig. 9, *a* by the rectangles' method with a variable subinterval to find $<x>$ by the formula (10).

TABLE 1. The results of determining $<x>$ and $<x^2>$ by the formulas (10), (11).

Value	S235	HEA
$<x>$, μm	44.9	11
$<x^2>$, μm^2	9674.4	460.2

TABLE 2. The values of mass transfer parameters under impact processing.

Value	S235	HEA
$<v>$, m/s	0.0225	0.0055
D_{ef}, m^2/s	$1.9 \cdot 10^{-6}$	$8.5 \cdot 10^{-8}$

dom walk mechanism, the effective diffusion coefficient is used [2]:

$$D_{ef} = \frac{< x^2 > - < x >^2}{2t}. \quad (12)$$

The average velocity of the directed motion of atoms is found by the formula

$$< v >=< x > /t. \quad (13)$$

As a result, the following values of mass transfer parameters under impact processing were obtained (Table 2).

The self-diffusion coefficient in iron by the interstitial mechanism is $3.6 \cdot 10^{-13}$ m^2/s by the molecular-dynamics method at 300 K [20], which is 7 orders of magnitude lower than the calculated effective mass transfer coefficient for S235 ($1.9 \cdot 10^{-6}$ m^2/s) under impact processing. Therefore, it can be concluded that the main foundation to the anomalous mass transfer under impact processing is contributed by the directional drift of particles, which is described by the second term in the general flux equation (14).

The flux equation assumes the sum of directed motion with random walks about its trajectory and has the form [18]

$$J = -D \frac{\partial C}{\partial x} + < v > C, \quad (14)$$

where J is the flux of atoms, and x is the co-ordinate, which for a one-dimensional process is equal to the distance from the origin.

As a result of impact processing, the effective diffusion coefficient (mass transfer) is 22 times higher in S235, than in HEA (see Table 2). This can be explained by the fact that the additional 'friction' force, which has arisen due to the incommensurability of its own atoms in the HEA, complicates directional mass transfer process because of the dislocations glide [11, 13].

3.3. Determination of Driving Forces and Mobility of Atoms in the Process of Mass Transfer under Impact Processing

The average value of the resultant force $<F>$ is a result of the impact,

which consists of the average normal response force $<N>$ and the force of gravity on sample at perpendicular impact. Then, $<F>$ is found by formula

$$< N >=< F > +mg . \tag{15}$$

When falling a block of mass 10.5 kg from a height 1 m, the kick-back is equal to 17 cm; then,

$$< F >= \Delta p / \Delta t . \tag{16}$$

The velocity of the body at the moment of falling, *i.e.*, the maximum speed

$$\upsilon = \sqrt{2hg} = 4.5 \text{ m/s} . \tag{17}$$

As a result of the calculations, $<F> = 42.5 \cdot 10^3$ N, $<N> = 4.2 \cdot 10^4$ N.

Our estimates show that about 50% of the energy is spent on elastic deformation, damping pad in the basement of equipment, heating the sample, and on elastic compression of a hardened steel spacer plate. Therefore, in further calculations, a normal response force value will be used as a twice less: $2 \cdot 10^4$ N.

Using the obtained data, the normal stresses, σ_0, in the cross-section are calculated according to the formula

$$\sigma_0 =< N > /A_0 = 2.5 \cdot 10^2 \text{ N/mm}^2 . \tag{18}$$

The tangential stress that leads to dislocation glide was calculated [21]:

$$\tau = \sigma_0 \cos\varphi \cos\lambda = \sigma_0 / 2 = 1.25 \cdot 10^2 \text{ N/mm}^2 . \tag{19}$$

From the data on the dependence of dislocation glide speed on tangential stress [22], it follows that the dislocation velocity is about 10^4 cm/s. Based on these data, the dislocation density ρ leading to mass transfer was estimated by the Taylor–Orowan equation [23]: $1.1 \cdot 10^5$ cm^{-2}.

From the second relation of the Einstein–Smoluchowski equation founding the force acting on each atom [2],

$$< x(t) >= \frac{1}{2} \frac{F < x^2(t) >}{k_B T} . \tag{20}$$

As a result, the driving force F for S235 at 300 K temperature, which is of $3.8 \cdot 10^{-17}$ N, and for HEA is of $1.96 \cdot 10^{-16}$ N, is determined. The average displacement and average quadratic displacement for S235 and

HEA were calculated above (see Table 1).

The authors of Ref. [24] showed that the HEA coating applied by ESA to stainless steel consists of zones of interdroplet spaces having a nanoscale structure (2.5–15 nm) with a b.c.c. crystal lattice and areas of droplet fall having a grain structure. AlCuCoFeNiCr in the cast state contains of three phases: two with an f.c.c. lattice and one with a b.c.c. lattice. Lattice parameter is as follows: $a_{\text{f.c.c.(1)}} = 0.3625$ nm (1%), $a_{\text{f.c.c.(2)}} = 0.3593$ nm (26%), $a_{\text{b.c.c.}} = 0.2879$ nm (73%) (in parentheses, it is indicated the percentage content of the corresponding phase). To calculate the work A of force acting on each atom by formula (21), the used lattice spacing for a b.c.c. iron crystal is equal to 0.286 nm, since the volume fraction of a b.c.c. phase is significantly larger for case of AlCuCoFeNiCr:

$$A = FS = Fa / \sqrt{2} . \tag{21}$$

The calculations found that $A_{\text{S235}} = 7.7 \cdot 10^{-27}$ J, $A_{\text{HEA}} = 4 \cdot 10^{-26}$ J.

The work of force directed action on the atoms is not enough to make atom a jump to the neighbouring position, because the magnitude of the work of force is significantly less than the thermal oscillations energy $k_B T$ ($4.11 \cdot 10^{-21}$ J). Nevertheless, in our case, the transfer of radioactive tracers to new positions is observed. This indicates that mass transfer under external influences is realized due to mobile dislocations, rather than direct diffusion jumps of atoms.

Let us estimate the mobility of atoms in the process of anomalous mass transfer for S235 and HEA. Some authors use the concept of diffusion mobility as a synonym for the diffusion coefficient, although they have different dimensions. Mobility of atoms depends on strength and velocity according to the formula

$$\mu = < v > / F ; \tag{22}$$

the founded $<v>$ for S235 and HEA are presented in Table 2.

The calculations found that the mobility of ^{60}Co atoms in S235 is equal to $5.9 \cdot 10^{14}$ m/(s·N), and for HEA, it is of $2.7 \cdot 10^{13}$ m/(s·N).

On the other hand, diffusion mobility is related to the diffusion coefficient according to the Einstein–Smoluchowski equation:

$$\mu = D_T / (k_B T) . \tag{23}$$

If, in formula (22), D_T is replaced by D_{ef} (see Table 2), then, the following mobility values are obtained: $4.6 \cdot 10^{14}$ m/(s·N) for S235 and $2.07 \cdot 10^{13}$ m/(s·N) for HEA. This is consistent with the results of the calculation by the previous formula (21). Therefore, the well-known Einstein–Smoluchowski equation for determining mobility can be used

for the process analysis of the anomalous mass transfer under external influences, if to replace D_T by D_{ef}.

4. CONCLUSIONS

1. For the first time, on the basis of experimental data, a method for determining the parameters of anomalous mass transfer with separation of the diffusion component and drift under driving force is proposed. The method is based on determining the exponent of the power n at x when plotting the concentration dependence of the following form: $(\ln(C/C_0))/x^n = \text{const}$. Based on the numerical value of the exponent n, a conclusion about the mass transfer mechanism and the selection of appropriate formulas for finding the parameters of mass transfer: D, D_{ef}, $<v>$, μ, F is made.
2. As shown using our method, the predominant mechanism of mass transfer under the ESA and mechanical impact conditions in S235 and HEA is the directed motion of atoms, which are entrained by mobile dislocations, since the drift component of the flux equation is significantly larger than the diffusion component by the mechanism of random walks. This is also confirmed by estimates of the work of force due to the atoms' movement, the value of which ($A_{S235} = 7.7 \cdot 10^{-27}$ J, $A_{HEA} = 4 \cdot 10^{-26}$ J) is much less than the energy of thermal vibrations $k_B T$ ($4.11 \cdot 10^{-21}$ J).
3. It is shown that the effective diffusion coefficient (mass transfer) as a result of external influences (mechanical impact and ESA) is tens of times higher in S235 than in HEA, which is consistent with the dislocation mechanism of mass transfer. This coincides with the conclusions of the authors of Ref. [13] that the additional 'friction' force, which has arisen due to the incommensurability of its own atoms in the HEA, complicates directional mass transfer process because of the dislocations glide.
4. For the first time, based on the mean and root-mean-square displacements of atoms obtained from the experimental concentration profiles, the force acting on each atom and the mobility of ^{60}Co atoms in iron under mechanical impact processing are determined.

The work is carried out within the framework of R&D (Reg. Nos. 0117U002133 and 0122U002366) supported by the National Academy of Sciences of Ukraine, which is gratefully acknowledged.

REFERENCES

1. J.-P. Bouchaud and A. Georges, *Phys. Rep.*, **195**, Iss. 4–5: 127 (1990).
2. R. Metzler and J. Klafter. *Phys. Rep.*, **339**, Iss. 1: 77 (2000).
3. L. N. Larikov, V. M. Fal'chenko, and V. F. Mazanko, *Avtomaticheskaya Svar-*

ka, No. 5: 19 (1974) (in Russian).
4. L. N. Larikov, V. M. Fal'chenko, and V. F. Mazanko, *DAN SSSR*, **221**, No. 5: 1073 (1975) (in Russian).
5. S. I. Sydorenko, O. V. Filatov, and S. M. Voloshko, *Anomal'ne Masoperenesennya. Zakonomirnosti ta Mekhanizmy* [Abnormal Mass Transfer. Laws and Mechanisms] (Kyiv: National Technical University of Ukraine 'Kyiv Polytechnic Institute': 2008) (in Ukrainian).
6. A. C. Quillen, *Notes on the Central Limit Theorem, Random Walks and Diffusion* (2021).
7. S. V. Divinski, A. Pokoev, N. Esakkiraja, and A. Paul, *Diffusion Foundations*, **17**: 69 (2018).
8. Yu. F. Babikova, A. A. Gusakov, V. M. Minaev, and G. G. Ryabova, *Analitcheskaya Avtoradiografiya* [Analytical Autoradiography] (Moskva: Ehnergoatomizdat: 1985) (in Russian).
9. L. N. Larikov and V. I. Isaichev, *Diffuziya v Metallakh i Splavakh* [Diffusion in Metals and Alloys] (Kiev: Naukova Dumka: 1987) (in Russian).
10. P. V. Pavlov and A. F. Khokhlov, *Fizika Tverdogo Tela* [Solid State Physics] (Moskva: Vysshaya Shkola: 2000) (in Russian).
11. O. V. Filatov and O. M. Soldatenko, *Metallofiz. Noveishie Tekhnol.*, **42**, No. 1: 1 (2020).
12. D. A. Kropachyov, O. E. Pogorelov, and O. V. Filatov, *Metallofiz. Noveishie Tekhnol.*, **35**, No. 6: 793 (2013) (in Russian).
13. S. O. Firstov, T. G. Rogul, N. A. Krapivka, S. S. Ponomarev, V. N. Tkach, V. V. Kovyljaev, V. F. Gorban', and M. V. Karpec, *Deformatsiya i Razrushenie Materialov*, No. 2: 9 (2013) (in Russian).
14. V. P. Bevz, V. F. Mazanko, A. V. Filatov, and S. P. Vorona, *Metallofiz. Noveishie Tekhnol.*, **28**, Spec. Iss.: 271 (2006).
15. A. Filatov, A. Pogorelov, D. Kropachev, and O. Dmitrichenko, *Defect and Diffusion Forum*, **363**: 173 (2015).
16. I. N. Karnaukhov, A. E. Pogorelov, and M. S. Chernolevskii, *Metallofiz. Noveishie Tekhnol.*, **28**, No. 6: 743 (2007) (in Russian).
17. A. Kelly and G. W. Groves, *Crystallography and Crystal Defects* (London: Longman Group: 1970).
18. J. R. Manning, *Diffusion Kinetics for Atoms in Crystals* (D. Van Nostrand Company: 1968).
19. V. M. Mazanko, O. V. Filatov, and S. P. Vorona, *Metallofiz. Noveishie Tekhnol.*, **17**, No. 9: 74 (1995) (in Russian).
20. O. V. Filatov, *Mezoskopichna Fizyka ta Modelyuvannya Materialiv* [Mesoscopic Physics and Modelling of Materials] (Kyiv: National Technical University of Ukraine 'Kyiv Polytechnic Institute': 2015) (in Ukrainian).
21. V. I. Trefilov, V. F. Moiseev, and Ye. P. Pechkovskij, *Deformatsionnoye Uprochnenie i Razrushenie Polikristallicheskikh Metallov* [Strain Hardening and Fracture of Polycrystalline Metals] (Kiev: Naukova Dumka: 1987) (in Russian).
22. B. Gurrutxaga-Lerma, J. Verschueren, A. P. Sutton, and D. Dini, *Int. Mater. Rev.*, **66**, Iss. 4: 1 (2020).
23. J. Hirth and J. Lothe, *Theory of Dislocations* (Krieger Publishing Company: 1982).
24. V. M. Nadutov, P. Yu. Volosevich, A. V. Proshak, V. E. Panarin, and M. E. Svavil'nyy, *Metallofiz. Noveishie Tekhnol.*, **39**, No. 11: 1525 (2017) (in Russian).

Metallophysics and Advanced Technologies
Металофіз. новітні технол.
Metallofiz. Noveishie Tekhnol.
2025, vol. 47, No. 1, pp. 57–81
https://doi.org/10.15407/mfint.47.01.0057
Reprints available directly from the publisher

PACS numbers: 46.25.-y, 46.35.+z, 81.20.Hy, 81.40.Gh, 81.40.Jj, 81.40.Lm, 83.60.Jk

Study of the Stress–Strain State of the Material of the Blanks during Plastic Stamping by Rolling

V. M. Mykhalevych, M. A. Kolisnyk*, and A. A. Shtuts*

Vinnytsia National Technical University,
95 Khmelnytske Shose,
21021 Vinnytsia, Ukraine
**Vinnytsia National Agrarian University,*
3 Sonyachna Str.,
21008 Vinnytsia, Ukraine

The work is aimed at solving an urgent problem in the scientific and technical field: the development and implementation of new technological processes in metal processing aimed at resource-saving and increasing production efficiency. Spinning is an important process in modern industry for the production of thin-walled workpieces, which are widely used in various industries. Investigation of the stress–strain state of the material during spinning is of great importance for improving manufacturing technologies and increasing product quality. This work proposes solutions of key research aspects such as the influence of process parameters (temperature, deformation rate, pressure, *etc.*) on the stress–strain state of the material. The relationship between these parameters and the mechanical properties of the processed material, including strength, plasticity, and crack resistance, is analysed. The investigation includes experimental methods such as mechanical testing, microstructural analysis, and modelling of deformation processes.

Key words: metal processing, spinning, resource-saving, technological processes, production efficiency, low-waste technologies, pressure material processing, stress–strain state, metal plasticity, forming, technological inheritance, complex-profile products.

Corresponding author: Volodymyr Markusovych Mykhalevych
E-mail: vmykhal2@gmail.ua

Citation: V. M. Mykhalevych, M. A. Kolisnyk, and A. A. Shtuts, Study of the Stress–Strain State of the Material of the Blanks during Plastic Stamping by Rolling, *Metallofiz. Noveishie Tekhnol.*, **47**, No. 1: 57–81 (2025). DOI: 10.15407/mfint.47.01.0057

Робота стосується вирішення актуальної проблеми в науково-технічній галузі: розробки та впровадження нових технологічних процесів металооброблення, спрямованих на ресурсозбереження та підвищення ефективности виробництва. Формування є важливим процесом промисловости для виробництва тонкостінних заготовок, які широко застосовуються в різних галузях промисловости. Дослідження напружено-деформованого стану матеріялу під час формування має важливе значення для вдосконалення технологій виготовлення та підвищення якости продукції. У даній роботі запропоновано вирішення ключових аспектів дослідження, таких як вплив параметрів процесу (температури, швидкости деформації, тиску тощо) на напружено-деформований стан матеріялу. Проаналізовано зв'язок між цими параметрами та механічними властивостями оброблюваного матеріялу, зокрема міцністю, пластичністю та тріщиностійкістю. Дослідження включають експериментальні методи: механічні випробування, аналізу мікроструктури й моделювання процесів деформації.

Ключові слова: металооброблення, формування, ресурсозбереження, технологічні процеси, ефективність виробництва, маловідходні технології, пресове оброблення матеріялів, напружено-деформований стан, пластичність металу, технологічна спадковість, вироби складного профілю.

(Received 8 May, 2024; in final version, 20 November, 2024)

1. INTRODUCTION

Spinning, as a process of forming metal workpieces, is of significant importance in modern industry, especially in the production of parts where the requirements for quality and precision are high.

Due to wide application of it and constant strive for optimizing production processes, research of the stress–strain state of the material during spinning becomes highly important. Understanding the internal processes occurring during material processing allows for the improvement of manufacturing technologies and the enhancement of product quality.

The object of the research is the behaviour of the material under the influence of various stamping parameters, such as temperature, deformation rate, pressure, and material thickness.

The analysis of the stress–strain state methods in spinning processes (SP) in the development and improvement of processes is particularly important. Information about the stress–strain state (SSS) of workpiece material and the influence of various technological processes on it allows determining the force parameters, evaluating the deformability of workpiece material, the stability of tooling, purposefully expanding the technological capabilities at the development stage, and predicting the operational characteristics of products. The most objective results are obtained from the study of SSS of workpiece material

using various research methods.

Due to the complexities of forming workpieces by SP method due to the influence of numerous factors, it is most expedient to use various experimental and computational methods for analysing SSS of the material.

Hardness measurement method. The hardness of a material is directly related to the maximum stress intensity experienced by the material throughout its entire history of plastic deformation σ_i [9, 12, 15]. Moreover, elastic unloading during cyclic deformation of metals does not lead to a change in hardness.

Therefore, the definition σ_i according to the results of the hardness measurement, it is possible only for cases of plastic deformation. Thus, for pressure treatment processes, it is possible to determine the intensity of stresses in the plastic zone based on the results of hardness measurements σ_i and taking into account the hypothesis of a single flow curve and intensity of deformations ε_i.

When investigating products obtained by SP method, the most suitable method for hardness measurement is the Vickers method, which provides a minimal plastic zone around the indentation. The use of the hardness measurement method requires the availability of a calibration chart for 'stress intensity–hardness–degree of deformation' σ_i–HV–ε_i.

Grading graphs of metals processed by rolling stamping (SHO) methods are built based on the results of hardness measurements on a hardness tester in the cross-sections of cylindrical samples deposited under conditions of a linear stress state. At the same time, the values are determined σ_i and ε_i according to the results of measuring the size of the samples and the deposition force according to the formulas:

$$\sigma_i = 4P / \pi d^2,\ \varepsilon_i = \ln(h_0 / h), \quad (1)$$

where P is deforming force, d is diameter of the deformed sample; h_0 and h are the height of the sample before and after deformation.

Samples are cut in the meridian direction, placed in a holder, and filled with epoxy resin. After hardening, the samples in the holder are ground using a series of abrasive papers, polished, and hardness is measured at 10–15 points of the cross-section. According to average hardness values and calculated values, σ_i and ε_i build grading graphs.

Figure 1 shows the workpieces obtained by SHO method according to the combined scheme of planting and reverse extrusion, cut, poured into a holder, polished and processed by measuring hardness with the construction of hardness isolines. Isolines of stress intensity and deformation intensity were obtained with the use of the constructed grading schedule based on them.

In Figures 2 and 3, grading graphs of M06 copper and low-alloyed steels 30ХГСА and 40ХН2МА are constructed, respectively. Of particular interest is the gradation graph of M06 copper, which has a

Fig. 1. Cross-sections of workpieces for hardness measurement.

strong dependence of stress intensity on strain intensity up to the values of the latter $\varepsilon_I \geq 1$. This allows determining the deformation intensity with sufficient accuracy based on hardness measurement results up to relatively high values. Thus, copper can be used for physical modelling of SP processes of other metals.

For the investigation of particularly thin-walled elements, the hardness measurement method is unsuitable due to the small size of the investigated plastic zone compared to the size of the indenter impression. Therefore, microhardness measurement of the material is used to analyse the strengthening of these zones μHV compared to the hardness measurement method, determining stressed deformed state (VAT) of the plastic zone by microhardness measurement is associated with a number of difficulties. First, when measuring the hardness, the imprint of the pyramid repeatedly overlaps various structural components that have different hardness. In the case of a homogeneous material, as a result of the measurements, the value of the average hardness is obtained, which depends only on the strengthening.

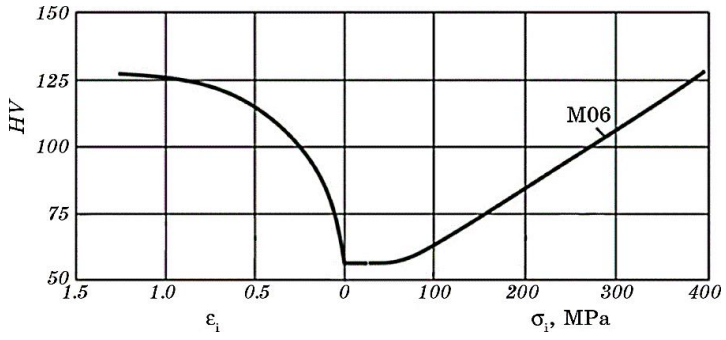

Fig. 2. Graduation graph σ_i–HV–ε_i copper M06.

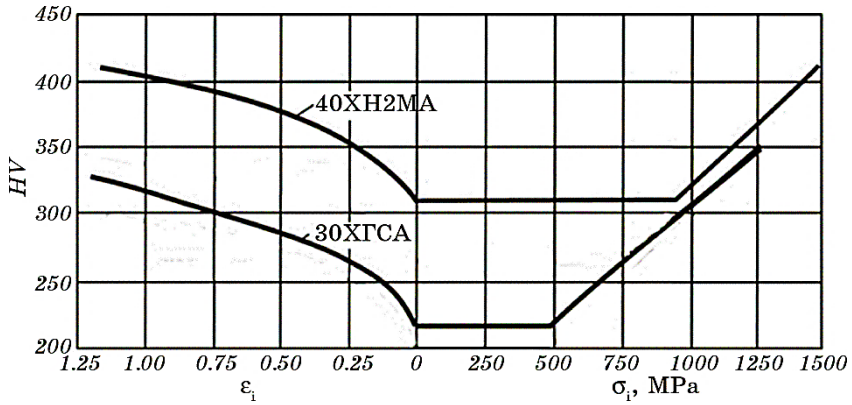

Fig. 3. Graduation graphs σ_i–HV–ε_i low-alloy steels.

When measuring microhardness, the size of the imprint, as a rule, does not exceed the size of a separate structural component. Therefore, to obtain reliable data, it is necessary to measure the microhardness in the same structural component, preferably in the one that strengthens the most. This is not always possible, especially if you need to get information in the form of an array of values in some area.

On the other hand, since the hardness is related to the microhardness of the structural components, this relationship can be represented in the form of certain dependence [14]. In work [18, 20] the specified dependence is adopted in the form of a linear model:

$$H = H_1 a_1 + H_2 a_2 + C, \tag{2}$$

where a_1, a_2, C are constants that do not depend on ε_i.

Thus, the microhardness of the structural components can be converted into the macrohardness of the material and obtain an already substantiated dependence.

On the other hand, if there is strengthening in the workpiece with the same degree, then the study SSS can be carried out by direct measurement of microhardness. For this, it is necessary to collect only statistics of microhardness values μHV at every level.

Our research showed that, if we make about 15 measurements of microhardness in a zone with the same degree of hardening, we would get its average value, which clearly correlates with the values σ_i and ε_i. At the same time, there is no need to monitor the microhardness of any individual structural component. Study of the regularity of the distribution of values σ_i and ε_i in the deformed layer by measuring microhardness in work [20, 21, 25] confirm the effectiveness of this method.

To build grading graphs σ_i–HV–ε_i samples are used, as for measuring hardness. However, surface preparation for microhardness meas-

urement is significantly different, as even a slight defamation of the surface layer distorts the measurement results. While measuring the hardness, the riveted thin layer is pressed by the pyramid and does not affect noticeably the hardness reading.

When investigating SSS of the plastic zone in blanks obtained by spin forming methods, they are cut and the surface is prepared similarly to the surface of calibration samples. Measurements of hardness are then conducted at intervals that prevent the overlapping of plastic zones from indenter impressions. By analysing the hardness measurements of the deformed zone and using calibration graphs, isoclines of distribution are obtained σ_i and ε_i. When necessary, the accuracy of the results obtained on specific sections (usually near the free surface of the blank) is verified using the grid method. Within the scope of conducted research, this method was used to determine SSS of the plastic zone in blanks during direct and reverse extrusion by the spin-forming method. Figure 4 depicts a holder with prepared polished sections of copper blanks, spun to various degrees according to a combined scheme of embossing with reverse extrusion.

The slip line field method. Based on the construction of a slip line field that meets static and kinematic boundary conditions, the distributions of stresses, strain rates, and the magnitude of accumulated strain along the flow lines, as well as the stress state index, are determined:

$$\eta = I_1(T_\sigma) / \sqrt{3I_2(D_\sigma)} , \qquad (3)$$

where $I_1(T_\sigma)$ is the first invariant of the stress tensor, $I_1(D_\sigma)$ is the second invariant of the stress deviator.

The obtained results of the research on SSS of the billet allow us to determine the energy and force parameters of the process, the amount

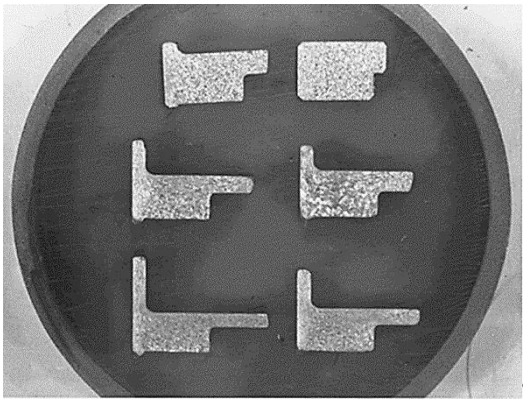

Fig. 4. Appearance of the holder with polished sections of copper blanks, prepared for microstructural analysis and hardness measurement.

of used plasticity resource of the metal, and the quality parameters of the produced products. This method was developed for the conditions of studying rolling processes.

The grid method. It belongs to the most common experimental-calculative method for determining SSS of deformed billets. Changes in co-ordinate-dividing grids allow determining the components of deformation at different stages of the deformation process. For the first time, it is obtained the ratio for calculating deformations based on distorted square dividing grids [1, 2, 10]. Renne generalized the method for the case, when the initial cell has the shape of a parallelogram.

Using this research methodology, studies can be conducted by measuring the co-ordinates of nodes step by step, *i.e.*, determining the fields of displacements over a certain period of time, followed by determining the fields of deformation rates. The stress state is calculated based on the deformed state using the relationships of plasticity theory. In this case, the stress field must satisfy the equilibrium equations, plasticity conditions, flow law, and boundary conditions.

The most commonly used approach is one in which the task of calculating the kinematics of deformation based on the known co-ordinates of nodes of the distorted dividing grid is reduced to constructing approximations $X(X_0, Y_0, t)$, $Y(X_0, Y_0, t)$ co-ordinates of nodes $\tilde{X}_{l,n}, \tilde{Y}_{l,n}$ grids (where X_0, Y_0 are Lagrangian variables associated with the undeformed sample) and their derivatives in co-ordinates and time. In this approach, the type of approximations used plays an important role. An approach, in which spline functions of one argument or a combination of splines of one argument (by time) and splines of two arguments (by co-ordinates at each stage) are used for approximation, and differentiation has become widespread. At the same time, the more effective approach, from the point of view of the accuracy of the approximation, is the approach in which the time derivatives of the co-ordinates of the nodes are first calculated (that is, the flow velocities of the material particles), and then their derivatives in terms of co-ordinates X_0, Y_0.

When studying spin-forming methods, the grid method needs to consider two types of heterogeneous input information: analytical and geometric. Analytical information consists of differential and algebraic equations that the unknown functions in the plastic domain and at its boundary must satisfy. Geometric information concerns the shape of the boundary of this domain. A fairly effective approach in studying metal forming processes using the grid method is the method of specifying geometric information and its calculation when constructing differential relationships using the theory of R-functions [21, 22, 25].

A function of several arguments is called an R-function if it changes sign only when at least one of its argument's changes sign. The following system of R-functions is most commonly used:

$$x \wedge y = x + y - \sqrt{x^2 + y^2},\ x \vee y = x + y - \sqrt{x^2 + y^2},\ \neg x = -x. \qquad (4)$$

The operations in formulas (4) are called R-conjunction, R-disjunction, and R-negation. It is obvious that R-conjunction is positive only in the first quadrant, while R-disjunction is positive in the first, second, and fourth quadrants.

An equation of the domain Ω and its boundary Γ is called an equation of the form:

$$\omega(x, y) = 0, \qquad (5)$$

if $\omega_\Gamma = 0$ i $\omega > 0$ inside the domain and $\omega < 0$ outside it. For clarity in constructing equations of domains, one can consider R-conjunction as the intersection of domains, and R-disjunction as their union.

The calculation of geometric information in analytical expressions in the R-functions' method is carried out using the concept of the solution structure of the problem, which is why the R-functions' method is also called the structural method. Let $U(x, y)$ be an unknown field in a certain domain Ω, which is a solution to a variational problem under certain conditions on the boundary Γ

$$L_{iU} = R_i \text{ in } \Gamma_i (i = \overline{1, m}) \qquad (6)$$

and in the region

$$A_U = V, \qquad (7)$$

where A and L_i are known differential or functional operators, V and R_i are known functions.

The structure of the solution to problem (6), (7) is called the following form:

$$U \equiv B(\varphi_1, \ldots, \varphi_n, \varphi), \qquad (8)$$

which for any sufficiently smooth functions will identically $\varphi_i(x, y)$ satisfy (6), (7). The correct and converse statement: for any function U satisfying (6), (7) $\varphi_1, \ldots, \varphi_n$ can be found such that (8) holds, then (8) is a complete structure. Proof of the completeness of structures is in general a difficult problem, and often the proof of completeness is the successful results of numerical experiments.

The functions $\varphi_1, \ldots, \varphi_n$ in formula (8), as shown in [11–14], are conveniently applied using finite functions, such as Shenberg B-splines. The presented methodology allows working with irregular and non-rectangular grids in areas with any shape of boundaries, and is also suitable for many transient processes where different grids are applied

at different transitions.

The finite element method (FEM) is a generalization of the variational method and belongs to the effective modern methods that allow determining the stress–strain state of inhomogeneous media [17, 18].

Considerable experience has been accumulated in the investigation of metal forming processes using numerical methods to determine the stress–strain state through direct variational methods, particularly the Ritz method, which equates the work of external and internal forces and has been further developed in works [3, 6, 7, 9], among others. The use of FEM significantly overcomes the difficulties in selecting coordinate functions and utilizes the capabilities of variational methods to determine not only integral but also local characteristics of the processes of plastic strengthening of machine part surfaces.

FEM is an effective numerical method for solving a wide range of boundary problems in continuum mechanics. It involves replacing the object under study with a set of discrete elements interconnected by nodes. The direct transition to the computational formula allows for naturally forming boundary conditions and arbitrarily placing the nodes in the element grid.

The most significant advantages of FEM in addressing metal forming processes include the freedom to choose nodal points, the arbitrary shape of the workpiece, the ability to set any necessary boundary conditions, considering the heterogeneity of material properties, and the use of standard software programs.

In the context of technological calculations, the sequence of solving a non-stationary nonlinear plasticity problem using FEM consists of the following steps [20, 22, 23]: problem formulation, discretization scheme, computation and result visualization procedure on a computer.

The problem formulation involves a mathematical description of the deformation schemes. To simplify the mathematical model, assumptions about the material property changes are introduced, namely, the material of the part is modelled as an elastoplastic material, friction coefficients between the workpiece and the tool are constant, and the tool is modelled as an absolutely rigid body.

The mathematical model also includes auxiliary equations that determine contact interaction, friction forces, and the condition of volume constancy. In modelling metal forming operations (MFO), the condition of volume constancy must be maintained, meaning the model's elements must also be of constant volume. In FEM, the compressibility of each element is characterized by a stiffness coefficient. This implies that the compressibility of any part of the workpiece-tool system, represented by a matrix of stiffness coefficients of its elements, ensures that elements only change their configuration during deformation without decreasing in volume.

The independent parameters are the nodal variables, and the distri-

butions within the elements are determined through them. As unknown kinematic and thermodynamic quantities, there are chosen-nodal velocities and displacements [7, 8, 20, 21].

The simplest form of idealization for a two-dimensional problem involves using triangles with nodes located at the vertices. These elements were among the first used.

Reducing the size of elements improves the convergence of FEM significantly more than increasing the order of elements. The reasons for this are: the influence of nodal variables is most pronounced when nodal points coincide with the vertices of elements, which is best facilitated in linear elements where all nodes lie at the vertices, from the second criterion of convergence, it follows that reducing the size of elements always leads to an increase in the accuracy of the solution due to better convergence, analysis of high-speed, nonlinear, and non-stationary MFO processes requires breaking the workpiece into small elements in areas with large gradients and abrupt changes in metal flow.

2. PRESENTATION OF THE MAIN RESEARCH MATERIAL

The most development and usage have been gained by the processes of orbital forging (OF) for obtaining complex profiled parts by implementing radial material flow of cylindrical workpieces using schemes of upsetting, flanging, spreading, squeezing, *etc*. Additionally, for a number of workpieces, a complex profile of the end part is characteristic, which can be obtained through direct extrusion (half-couplings are presented in Fig. 5, *a*, thrust bearing rings are presented in Fig. 5, *b*, *etc*.) [2].

Direct extrusion by OF method can be implemented in a rolling die with the necessary profile on the end of the workpiece opposite the end

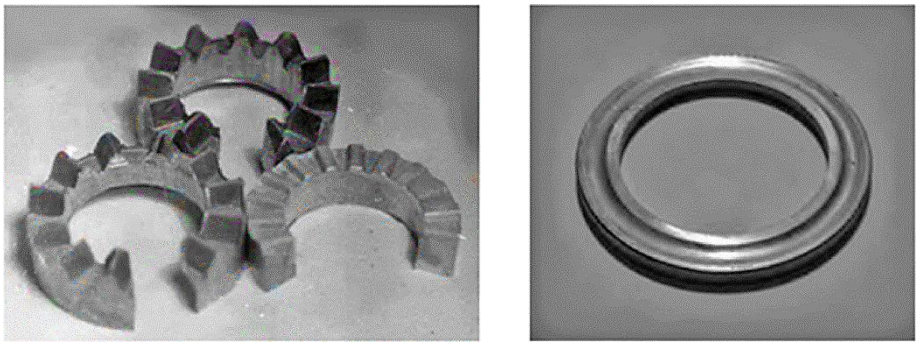

a *b*

Fig. 5. Workpieces obtained by OF method: cam half-couplings at different stages of rolling (*a*), thrust bearing ring (*b*).

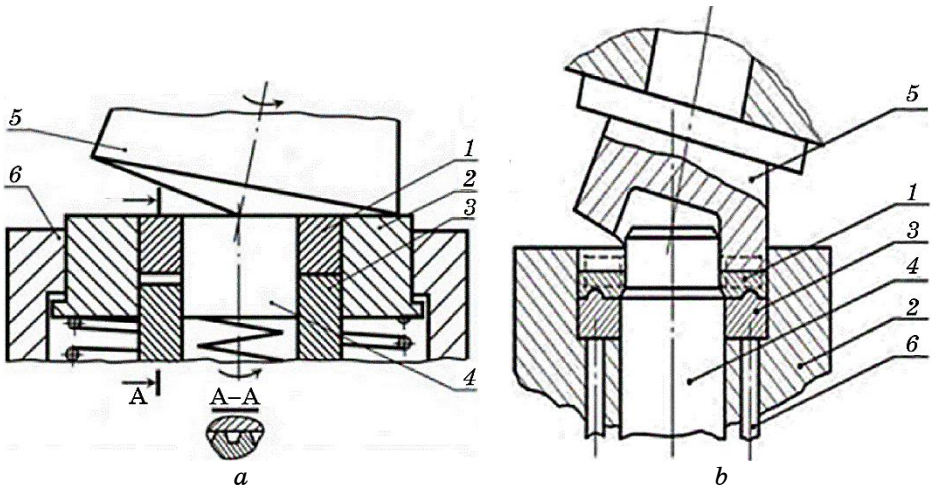

Fig. 6. Technological schemes of direct extrusion of the profile on the end of the workpiece by OF method: in a spring-loaded die and mandrel (*a*), in the die calibre of the stamp (*b*).

contacting the roll.

Figure 6 illustrates the technological schemes of forming and the corresponding elements of the workpiece ends.

Insufficient research of this process does not contribute to the development of technological schemes with a specified flow of material and the formation of necessary elements of the product. The lack of information about the material workability of the workpiece prevents the assessment of deformability and determination of the technological capabilities of the process based on factors of workpiece material failure and tool durability. The technological inheritability of the obtained products also remains undefined. Therefore, the study of the workability of workpiece materials is one of the important factors in improving processes of stamping by extrusion [1, 2]. To establish the influence of various technological parameters on the workability of the material, experimental research methods were initially applied: the method of hardness measurement, the method of dividing grids, and the analysis of the materials' microstructure.

The application of these methods in this work allows constructing paths of material particle deformation in the critical zones of the workpiece, which are used to assess the materials' deformability.

For physical modelling of the direct extrusion process by the extrusion method, the ring workpiece consists of two rings: internal and external. A rectangular dividing grid was applied to the external cylindrical surface of the internal ring. The appearance of the deformed rings, with a portion of the external ring cut off, is shown in Fig. 7.

Fig. 7. View of the rings after direct extrusion of the end profile by the extrusion method and cutting off a part of the external ring.

Figure 8 shows the view of the deformed grid on the surface of the internal ring at the initial (*a*), intermediate (*b*), and final (*c*) stages of direct extrusion by the extrusion method.

Figure 9 presents view of the deformed grid on the external surface of the punch.

When physically modelling the direct extrusion processes using elements skin (EC) method, copper M06 and armco-iron were chosen as

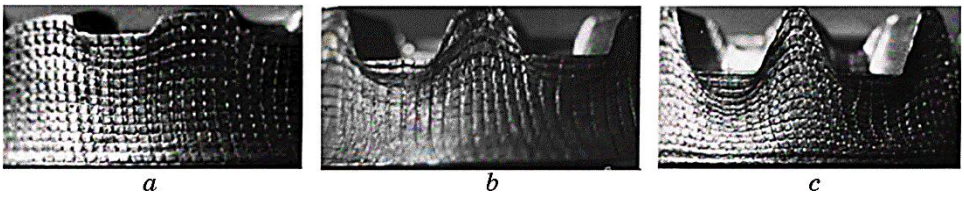

Fig. 8. View of the deformed mesh on the outer surface of the inner ring at different stages of direct extrusion by EC method.

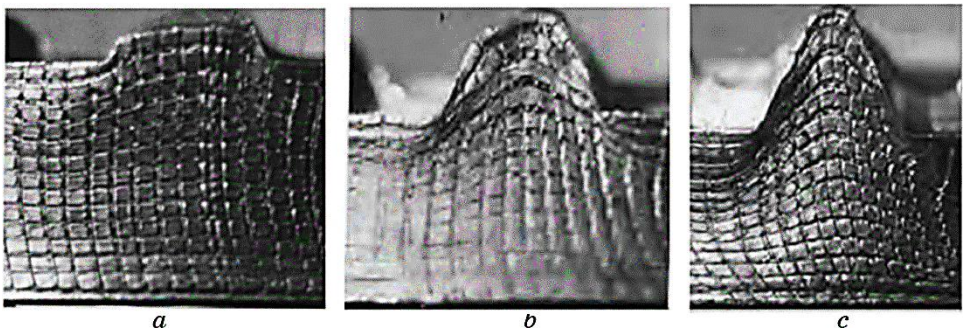

Fig. 9. View of the deformed mesh on the outer surface of the punch at different stages of direct extrusion by EC method.

the workpiece materials. Copper is characterized by high strengthening during plastic deformation, allowing for the precise determination of the distribution of deformation intensity in the internal zones of the workpieces with a high degree of accuracy. It also exhibits a pronounced but non-uniform initial microstructure. Armco-iron has a uniform grain structure, which can complement the results of the study with a microstructural analysis.

The view of the deformed microstructure of the copper M06 material in the cross-section of the punch at intermediate and final stages of deformation is shown in Fig. 10. Figure 11 presents an enlarged view of the microstructure of copper M06 at characteristic points (corresponding to Fig. 10, *b*) of the formed profile.

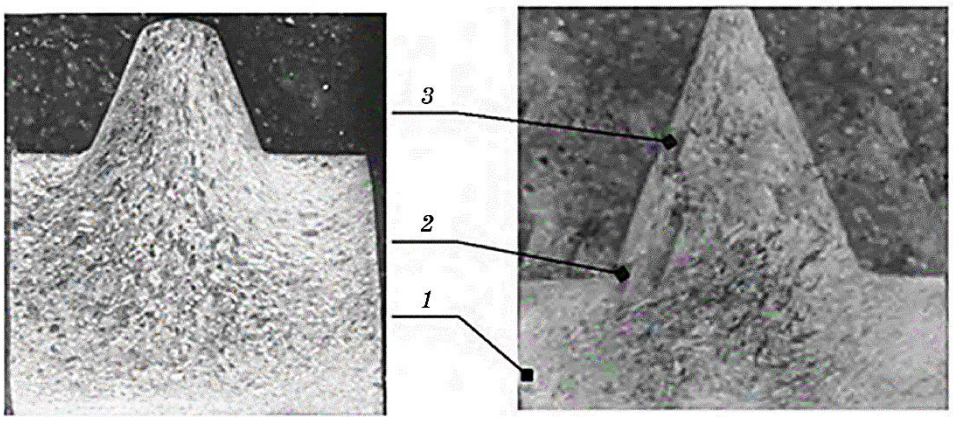

Fig. 10. View of the deformed microstructure of the workpiece material made of copper M06 in the cross-section of the punch at intermediate and final stages of deformation.

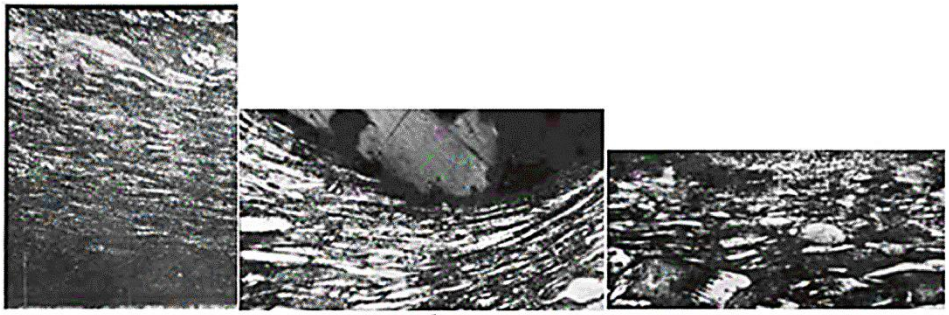

Fig. 11. Magnified view of the workpiece microstructure at characteristic points of the formed profile corresponding to Fig. 10, *b*: point *1* (contact zone with the roller) (*a*), point *2* (*b*), point *3* (*c*).

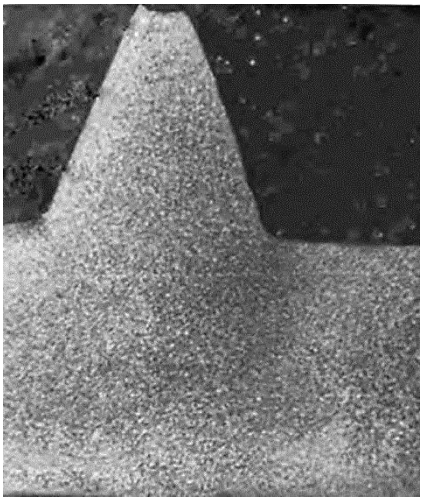

Fig. 12. View of the deformed microstructure of the workpiece material made of armco-iron in the cross-section of the die at the final stage of deformation.

The workpiece made of armco-iron (see Fig. 12) has a fine-grained structure, which was studied for individual zones under significant magnification.

The hardness measurement method is an effective way to determine the stress intensity σ_i in the workpiece without prior separation. Therefore, for processes of direct extrusion using the method, the stress intensity σ and the deformation intensity ε_i can be determined in the plastic zone of the workpiece based on hardness measurement results, taking into account the hypothesis of a single yield curve.

The graduation curve of copper M06 is shown in Fig. 2.

The investigation of the workpiece materials' nonuniform deformation state (SSS) by the hardness measurement method was conducted according to the technique presented in [3]. Figure 13 shows the distribution of deformation intensity in the extruded element zone obtained by hardness measurement.

Thus, the distribution of the intensity of deformations in the zone of the extruded element (see Fig. 12), obtained by the hardness measurement method, indicates a rather uneven nature of the deformed state in the cross section of the workpiece. The greatest intensity of deformations, which is observed in the contact zone of the roll with the workpiece, reaches the values $\varepsilon_I = 0.9–1.0$ and may exceed them. The next, most deformed, is the zone of entry of the metal into the forming channel. Here, the intensity of deformations reaches values $\varepsilon_I = 0.6–0.7$. The lowest level of deformations is observed at the free top of the extruded element and in its central part, and the intensity of deformations here reaches values $\varepsilon_I = 0.1–0.2$.

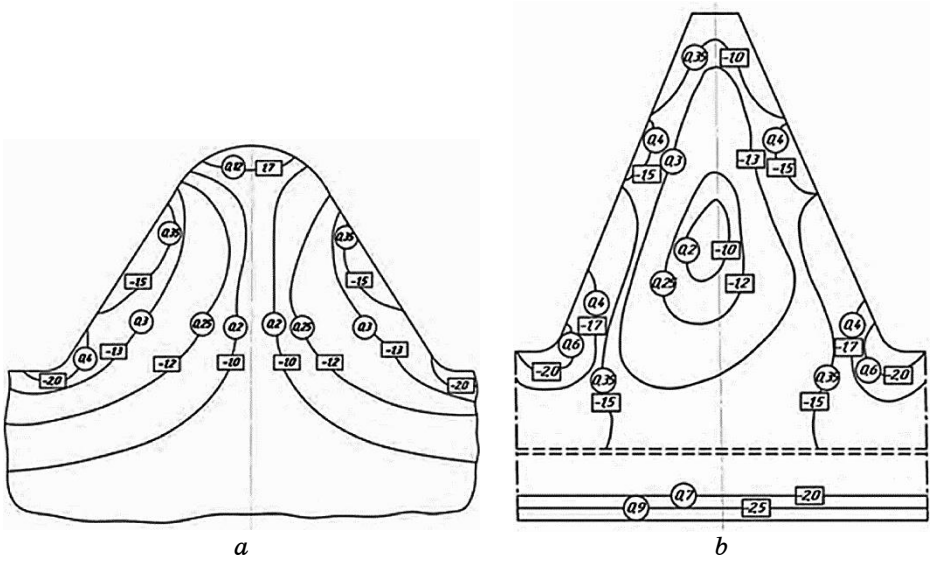

Fig. 13. Distribution of VAT parameters in the workpiece element obtained by extrusion using SHO method at intermediate (*a*) and final (*b*) stages: (O)η = const and (Ω)ε_i = const.

To study SSS of the plastic zone of the workpiece during direct extrusion by SHO method, we also used the method of co-ordinate dividing grids, built on the use of a technique based on the theory of *R*-functions [1]. At the same time, step-by-step extrusion of the element was carried out (see Fig. 8): a flat task. Character of distribution of isolines ε_I = const within the zone of the extruded element obtained from the results of the measurement of the co-ordinate dividing grid is shown in Fig. 14.

Thus, the distribution of the deformed state, obtained by the method of co-ordinate grids, coincides with that obtained by hardness measurement. The stress index in the zone of maximum deformation is $\eta = -2.5 - -2.0$ (see Fig. 13). These conditions indicate the presence of significant compressive stresses here, which makes the deformability of the blank material relatively safe. However, there is a risk of tooling failure in the areas near the tooth base. The material of the blank at the tooth tip undergoes relatively small deformations, but the stress index here is that requires an assessment of $\eta > +1$ material's deformability.

An important feature of this technological scheme is that metal particles from the free tooth tip and the 'stiff' stress scheme, during extrusion, come into contact with the tool, where their deformations continue to increase under the 'soft' stress scheme ($\eta = -1.3 - -1.5$). All this must be taken into account when constructing paths of material deformation to assess its deformability.

Another characteristic of the deformation is that, as can be seen in

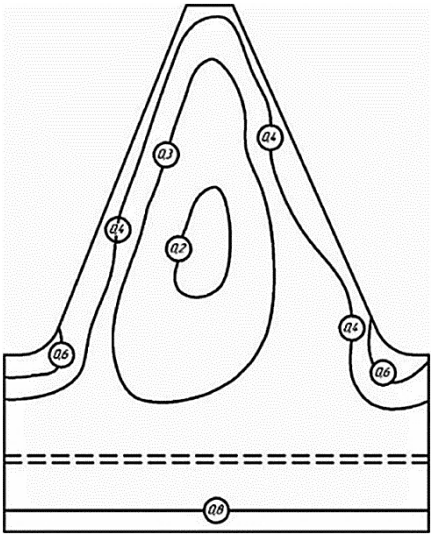

Fig. 14. Distribution of deformation intensity in the plane of the punch extruded by EC method, obtained from the measurement results of the coordinate grid.

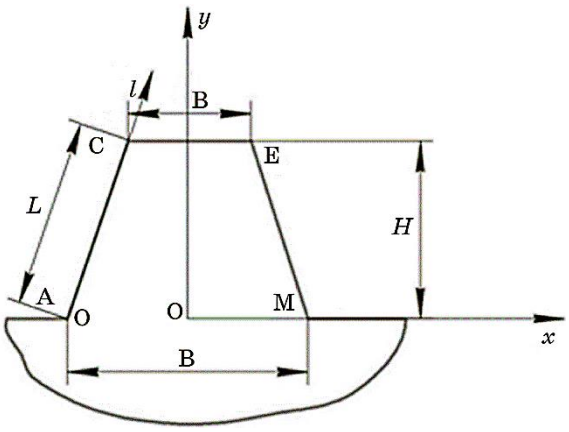

Fig. 15. Characteristic parameters of the profile of the element extruded by EC method.

Figs. 9 and 13, the deformation pattern in relation to the profile of the extruded element has a certain asymmetry. This is due to the asymmetric application of the load during blanking. Such a flow pattern is useful if the side surfaces of the element have different inclination angles. If it is necessary to eliminate the noted asymmetry, it is advisable to consider reversing the blank.

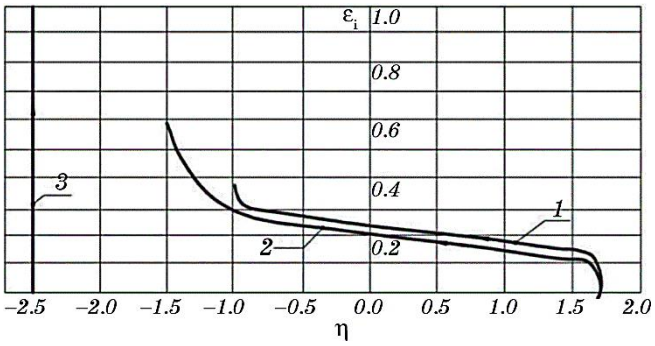

Fig. 16. Deformation paths of the material particles in the most characteristic deformed zones: in the middle of the lateral surface AC (*1*), at the entrance to the forming channel (near point A) (*2*), in the contact zone of the blank with the mandrel (*3*).

When changing the parameters of the element profile, characterized by the values shown in Fig. 15, the values of deformation intensity and stress index will change somewhat, but the character of their distribution will remain the same. The distribution character of the noted quantities will also remain unchanged when changing materials if the friction conditions remain unchanged.

To assess the deformability of the blank material and determine the limiting deformations, from the point of view of preventing material failure or ensuring the necessary technical characteristics of the part, it is necessary to have paths of deformation of particles in dangerous zones. Figure 16 shows the paths of deformation of particles of the blank material in the most deformed zones, obtained by the method of co-ordinate grids using the theory of *R*-functions.

The peculiarity of the deformation paths lies in the fact that at the initial stage of extrusion, the material on the line OM undergoes stretching at a stress ratio of $\eta = 1.73$. At the same time, the magnitude of deformation intensity is relatively small, reaching values of $\varepsilon_I = 0.15–0.20$ for the free surface at the final stage of shaping.

Subsequently, upon contact with the lateral surface of the matrix channel, deformation continues under conditions of $\eta = -1.0–+1.5$. For the most deformed area in contact with the mandrel, the deformation path *3* can be represented by an average value of the η parameter of $\eta = -2.5–-2.0$ in the mandrel pressure zone.

The extrusion scheme shown in Fig. 17, *a* provides for the extrusion of the flange and the reverse extrusion of the thin-walled element, and is implemented with a positive displacement of the apex of the conical mandrel (see Fig. 17, *a*). By displacing the apex of the mandrel along the axis of the blank, the flow of the flange material inside the blank can be ensured.

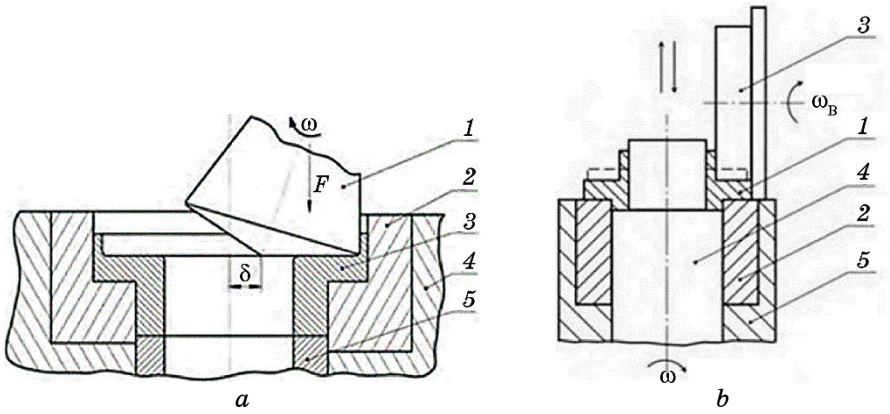

Fig. 17. Schemes of extrusion and reverse extrusion of thin-walled elements by SHS method on the end face of a ring blank with conical (*a*) and cylindrical (*b*) mandrels: *1*—blank, *2*—matrix, *3*—mandrel, 4—pusher sleeve, *5*—spindle.

The extrusion scheme shown in Fig. 17, *b* provides for the extrusion of the flange and the reverse extrusion of the thin-walled element, and is implemented with a negative displacement of the axis of the cylindrical mandrel (see Fig. 10).

To enhance the processes, an analysis of the residual stress distribution (RSD) in the blank material was conducted during the operations of both flanging and reverse extrusion using SSS method.

Figure 18 presents isolines of stress intensity distribution $\sigma_I = \text{const}$ and deformations $\varepsilon_I = \text{const}$, which were obtained from the results of measuring the hardness in the cross-sections of the blanks at different stages of rolling (the corresponding sections are shown in Fig. 4).

Thus, in the cross-section of the blank formed at the first stage of rolling (Fig. 18, *a*), the following characteristic zones of residual stress distribution can be identified.

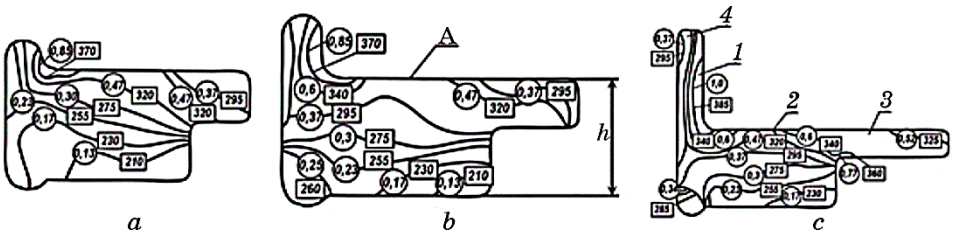

Fig. 18. Distribution of isolines (O)η = const and (Ω)ε_i = const in the cross-sections of M06 copper ring blanks formed by severe plastic deformation method.

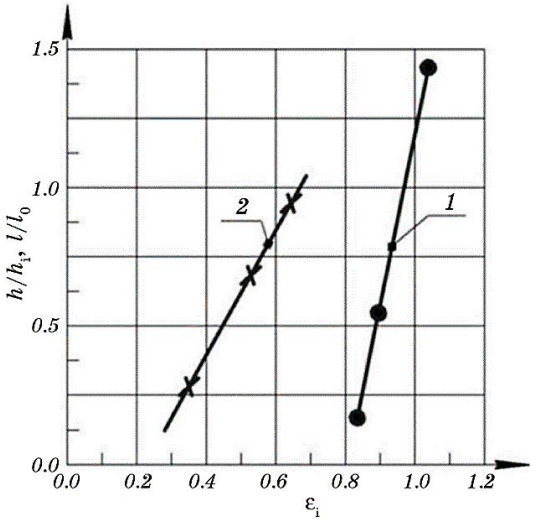

Fig. 19. Dependency of the relative height change of the thin-walled element h/h_i on the maximum intensity of deformations (*1*), and the relative size of the flange l/l_0 on the intensity of deformations in its peripheral area (*2*), according to Fig. 18.

The most deformed is the zone of the thin-walled element *1*, which is formed because of metal flow from zone *2*. The minor further deformation of zone *1*, as the height of the thin-walled element increases, (Fig. 19, dependence *1*) occurs due to successive cyclic shifts in the axial direction, caused by the characteristics of local loading in severe plastic deformation, and the increased resistance to metal flow in the gap between the roll and the mandrel.

Zone *2*, where the highest degree of deformation is observed at the contact with the roll (surface A), which gradually decreases as it moves away from the contact surface. The metal from zone *2* (Fig. 18, *b*) flows into zones *1* and *3*, and the intensity of its flow in one direction or another depends on the relative positioning of the roll and the blank [1, 3].

Zone 3 (the flange part of the blank) is a zone of relatively uniform deformation. The increase in deformation intensity on the periphery of the flange, depending on the relative increase in its length, is depicted in Fig. 19 by line *2*.

The distribution of the stress state index along the arc of contact in the middle part of the flange and along the contour of the blank formed by the roll is presented in Fig. 20. Thus, in the area with the highest intensity of deformations, a stress state pattern is observed that approximately corresponds to biaxial compression ($\eta \cong -2.0$).

Use of metals with higher resistance to plastic deformation σ_s, as well as an increase in unit crimping Δh leads to an increase in the stress

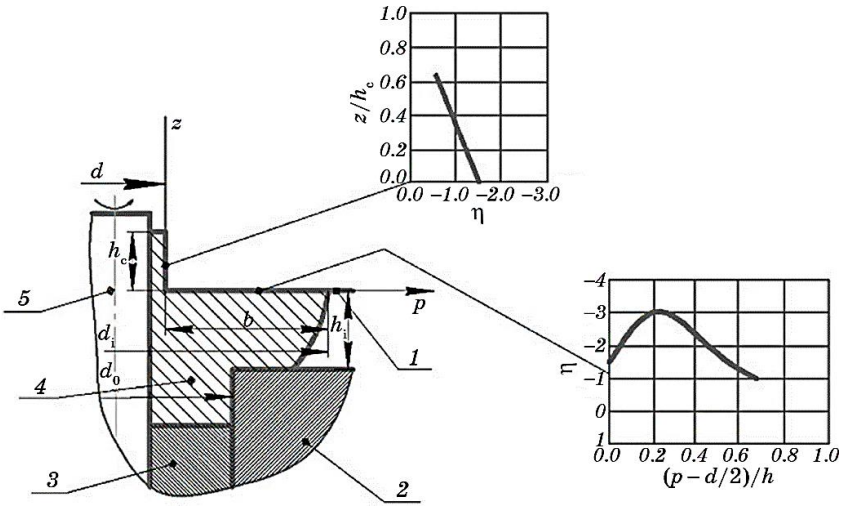

Fig. 20. Distribution of the stress state index along the height of the thin-walled element and along the width of the flange.

level, but does not have a noticeable effect on the indicator η.

It should be noted that in the zone of formation of maximum deformations in the thin-walled element there is a 'soft' scheme of the stress state ($\eta < -1.5$).

A stiffer stress state occurs in the flange part of the workpiece, namely on the peripheral, free from contact with the tool, surface (see Fig. 20).

Therefore, the assessment of the deformability of the workpiece material to determine the maximally achievable intensity of deformations ε_* or the value of the plasticity resource used ψ_B, should be carried out specifically for this zone.

Figure 21 shows the paths of deformation of metal particles on the free surface of the flange during its extrusion, depending on the parameters of the extrusion process.

Thus, the most favourable paths in terms of deformability are those with minimal ratio of deformed height to wall thickness of the workpiece and negative displacement of the roller tip.

Therefore, knowing the main parameters of the workpiece and its position during orbital forging, such as h_0, b_0 and δ, we can analytically describe the paths of metal deformation on the dangerous external surface of the flange and use this to assess the workpiece material's deformability.

Figure 22 shows graphs illustrating the patterns of change in the possible stress state values with increasing plastic deformation, depending on the parameters of the constructed model.

Stress state index η as a function of parameters θ and m at different

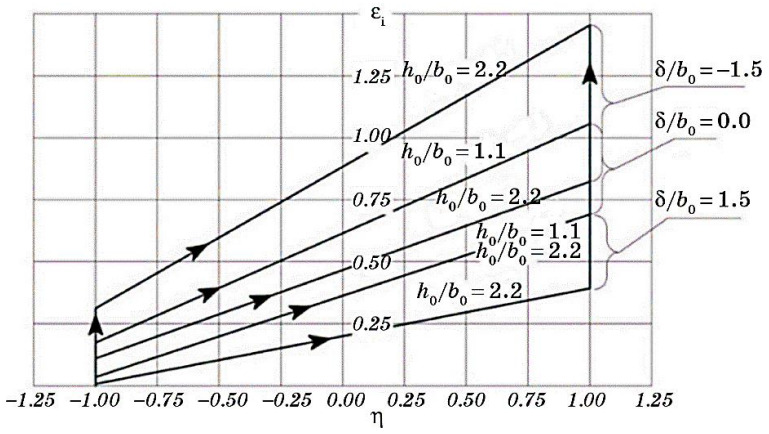

Fig. 21. Paths of deformation of the free surface of the peripheral part of the flange during orbital forging (h_0, b_0 are initial height and wall thickness of the tubular workpiece to be coined, δ is displacement of the tip of the conical roll from the axis of the workpiece).

stages of plastic deformation calculated using (9):

$$\begin{cases} \eta(t) = \dfrac{\dfrac{3}{2}(4-(1+\theta)(1+3\cos^2 t))}{\sqrt{9+\dfrac{3}{4}(2-(1+\theta)(1+3\cos^2 t))^2}}, \\ \bar{e}_i(t) = \dfrac{\sqrt{3}}{6} m \displaystyle\int_0^t \frac{\sqrt{(2-(1+\theta)(1+3\cos^2\tau))^2+12}}{\cos^2\tau}\, d\tau, \end{cases} \tag{9}$$

$$m \in [0,\infty), \theta \in [0,1], t \in [0, \pi/2].$$

Note that the last relation has only one material constant m, and the generalized relation (9) has two material constants: θ, m.

Another advantage of the recently derived relationship is the absence of a material constant in the analytical expression for the stress state in the parametric representation of deformation trajectories.

This leads to additional conveniences in analysing these relationships and selecting the material constant based on experimental data. In the generalized relationships (9), the material constant m is also absent in the analytical expression for the stress state indicator, although another material constant remains θ. These drawbacks are a natural trade-off for the ability to develop a more adequate model for the change in the stress state of a macro-particle of material on the free surface of the blank during roll stamping, given the displacement of the cone roller's apex from the blank's axis towards the contact spot.

Figure 23 presents the deformation trajectories we have constructed

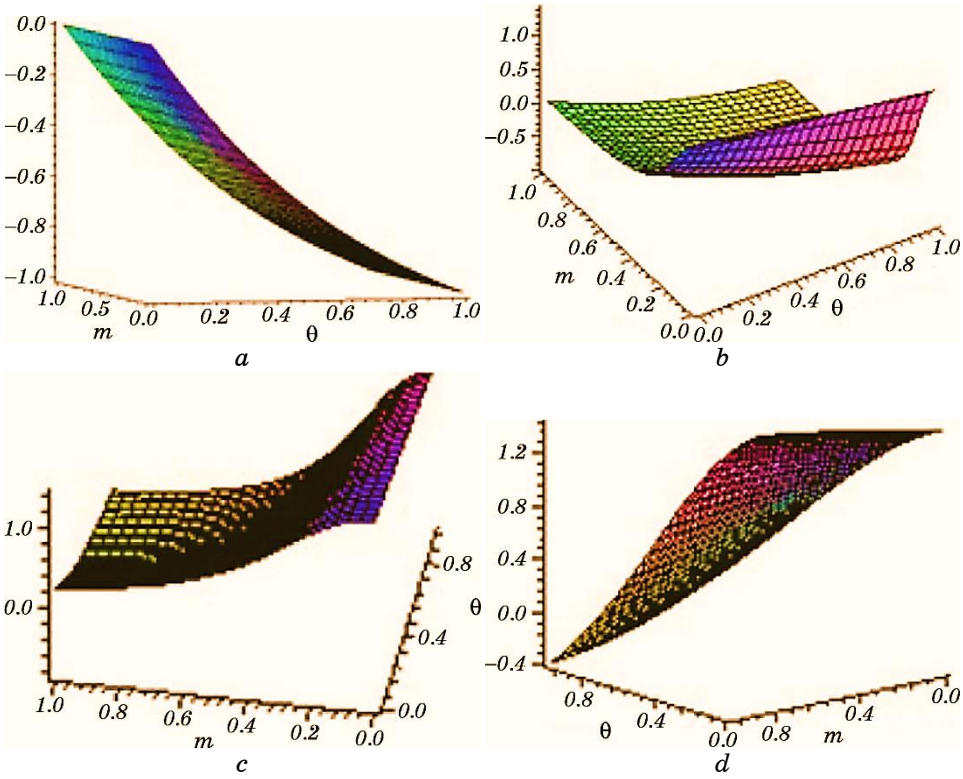

Fig. 22. Paths of deformation of the free surface of the peripheral part of the flange during orbital forging (h_0, b_0 are initial height and wall thickness of the tubular workpiece to be coined, δ is displacement of the tip of the conical roll from the axis of the workpiece).

for different values of material constants θ and m.

The advantages of representing deformation trajectories as parametric equations include the ease of analysing these trajectories. For instance, with a fixed value of the constant θ, we can determine the value of the parameter t that corresponds to the point, where the deformation trajectory intersects the y-axis. Based on the first equation of set (10), we can write

$$\eta(t) = 4 - (1+\theta)(1+3\cos^2 t) = 0,\ t \in [0, \pi/2], \tag{10}$$

from which follows

$$t = \arccos\left(\sqrt{\frac{3-\theta}{3(1+\theta)}}\right). \tag{11}$$

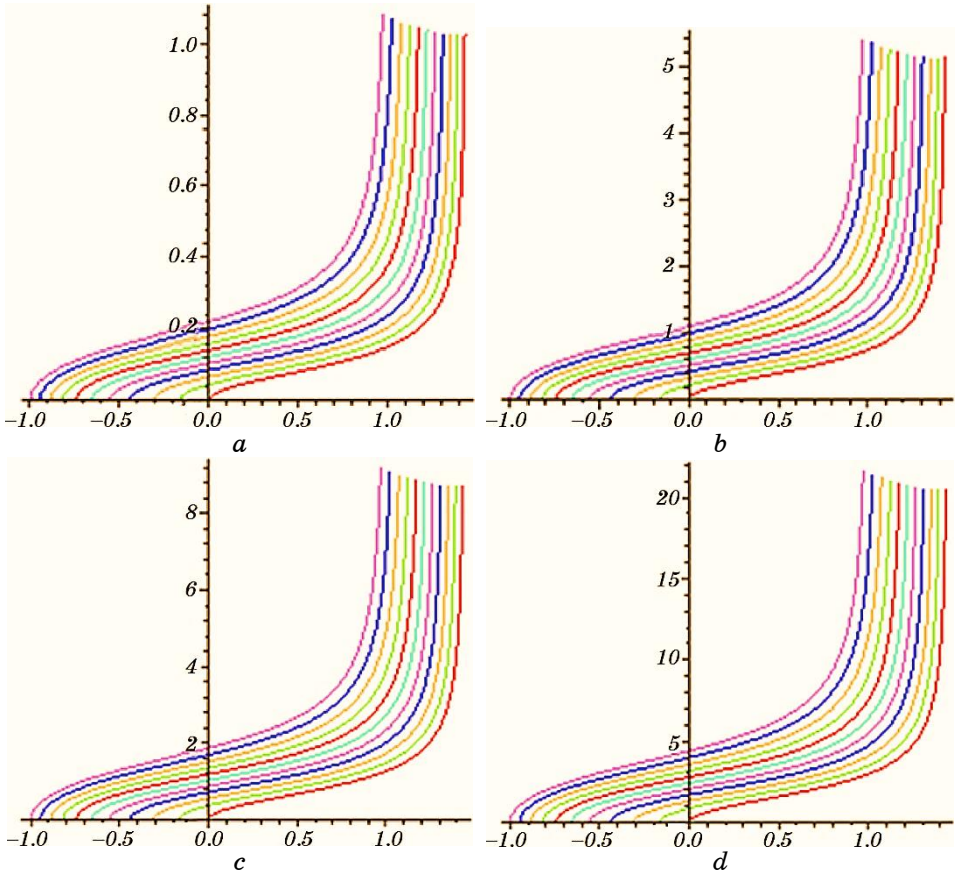

Fig. 23. Deformation trajectories $\bar{e}_i = \bar{e}_i(\eta)$ calculated for (10): $\theta \in [0, 1]$, $m =$ 0.1 (*a*), 0.5 (b*)*, 0.85 (*c*), 2.0 (*d*).

For example, at $\theta = 1$, $t \cong 0.9553166180$. Based on the second equation of system (12), we determine

$$\frac{\bar{e}_i(t = 0.9553166180)}{m} = \int_0^{0.9553166180} \sqrt{3 + \frac{1}{\cos^4 t}}\, dt \approx 2.206. \qquad (12)$$

From the last equality, it is easy to determine the ordinate (the amount of accumulated deformation) of the point of intersection of the deformation trajectory with the ordinate axis, in particular,

$$\bar{e}_i(\eta = 0, m = 0.1) \approx 0.22,\ \bar{e}_i(\eta = 0, m = 0.5) \approx 1.1,$$
$$\bar{e}_i(\eta = 0, m = 0.85) \approx 1.88,\ \bar{e}_i(\eta = 0, m = 2.0) \approx 4.41. \qquad (13)$$

3. CONCLUSION

The stress–strain state of workpiece material is an important characteristic necessary for assessing deformability and determining force parameters. Among the effective methods of NDS analysis are the grid method, hardness measurement, and microstructural analysis.

Direct extrusion by SHO method was considered by us using the example of forming end teeth of a gear sleeve. To increase the accuracy of determining deformation intensity in cross-sections of workpieces, a highly strengthening material—copper M06 was chosen for physical modelling.

As a result of constructing graduation graphs and measuring hardness in workpiece cross-sections, as well as grids on workpiece surfaces, the distribution character of stress and strain intensity, as well as the stress state index in the plastic area, was obtained. The most rigid stress state scheme is observed at the apex of the extruded teeth, but here the least deformation occurs. The largest deformations are formed at the base of the tooth, but the stress state is close to uniaxial compression.

Reverse extrusion by SHO method was also modelled on copper M06. NDS analysis showed that the most deformed zone is the thin-walled element zone, which is formed because of metal flow from the contact plastic spot area of the roller with the workpiece. Maximum deformations are observed in this zone, gradually decreasing as you move away from the contact surface. The flange part of the workpiece is a zone of relatively uniform deformation. Dependences of the growth of deformation intensity on the periphery of the flange from the relative increase in its length were constructed.

Based on the analysis results, paths of material particle deformation in dangerous zones due to possible workpiece destruction were constructed, which were then used to assess workpiece material deformability.

The possibilities of direct extrusion are limited by the complexity of force transmission from the roller to the opposite end face of the workpiece and significant contact stresses. Therefore, this operation is more suitable for calibration or forming of small-sized workpiece elements, which should be taken into account when developing corresponding SHO technological processes.

Further research in this direction will expand knowledge of material deformation mechanisms during stamping by extrusion and develop new approaches to optimizing technological processes in the production of metal parts.

REFERENCES

1. V. A. Matviychuk, *Tekhnika, Ehnergetyka, Transport APK*, No. 4: 110 (2022) (in Ukrainian).
2. A. A. Shtuts', *Herald of Khmelnytskyi National University. Series: Technical*

Sciences, **235**, Iss. 2: 167 (2016) (in Ukrainian).
3. A. A. Shtuts' and V. A. Matviichuk, *Tekhnika, Ehnergetyka, Transport APK*, No. 3: 178 (2016) (in Ukrainian).
4. V. A. Matviichuk, M. A. Kolysnyk, and A. A. Shtuts', *Tekhnika, Ehnergetyka, Transport APK*, No. 3: 77 (2018) (in Ukrainian).
5. A. A. Shtuts' and M. O. Sluzhaliuk, *Vibratsiyi v Tekhnitsi ta Tekhnolohiyakh*, No. 2: 138 (2020) (in Ukrainian).
6. A. A. Shtuts', *Vibratsiyi v Tekhnitsi ta Tekhnolohiyakh*, No. 4: 101 (2020) (in Ukrainian).
7. I. Kupchuk, M. Kolisnyk, A. Shtuts, and M. Paladii, *Bulletin of the Transilvania University of Braşov. Series I: Eng. Sci.*, **14**, No. 2: 1 (2021) (in Romania).
8. A. Shtuts and M. Kolisnyk, *Agricultural Eng.*, **54**: 62 (2022).
9. V. Matviychuk and A. Shtuts, *Traditional and Innovative Approaches to Scientific Research : Theory, Methodology, Practice* (Riga: Baltija Publishing: 2022), p. 90.
10. V. A. Matviichuk, V. M. Mykhalievych, and M. A. Kolysnyk, *Vibratsiyi v Tekhnitsi ta Tekhnolohiyakh*, No. 1: 81 (2022) (in Ukrainian).
11. V. A. Matviichuk and V. M. Mykhalievych, *Development of Local Deformation Processes: Theory and Practice of Pressure Treatment of Materials* (Zaporizhzhia: Motor Sich: 2016), p. 339 (in Ukrainian).
12. V. M. Mikhalevich, A. A. Lebedev, and Y. V. Dobranyuk, *Strength Mater.*, **43**: 591 (2011) (in Ukrainian).
13. A. A. Lebedev and V. M. Mikhalevich, *Strength Mater.*, **35**: 217 (2003).
14. V. O. Kraievskyi, V. A. Matviichuk, and V. M. Mykhalievych, *Improvement of Processes and Equipment for Pressure Treatment in Mechanical Eengineering and Metallurgy* (Kramatorsk–Sloviansk: 2003), p. 286 (in Ukrainian).
15. N. S. Hrudkina, O. E. Markov, A. A. Shapoval, V. A. Titov, I. S. Aliiev, P. Abhari, and K. V. Malii, *FME Trans.*, **50**, No. 1: 90 (2022).
16. V. Dragobetskii and A. Shapoval, *Metallurgical and Mining Industry*, No. 4: 363 (2015) (in Ukrainian).
17. V. Sikulskiy, V. Kashcheyeva, Y. Romanenkov, and A. Shapoval, *Eastern-European J. Enterprise Technol.*, **4**, No. 1: 43 (2017).
18. V. Dragobetskii, A. Shapoval, E. Naumova, S. Shlyk, D. Mospan, and V. Sikulskiy, *Proc. Int. Conf. Modern Electrical and Energy Systems MEES (November 15–17, 2017, Kremenchuk)* (IEEE: 2018), p. 400.
19. I. Kupchuk, M. Kolisnyk, A. Shtuts, M. Paladii, and A. Didyk, *Colloquium-Journal*, No. 16: 40 (2021).
20. S. Gundebommu, V. Matvijchuk, O. Rubanenko, and Yu. Branitskiy, *Mater. Today: Proc.*, **38**: 3337 (2021).
21. V. Matvijchuk, A. Shtuts, M. Kolisnyk, I. Kupchuk, and I. Derevenko, *Periodica Polytechnica, Mech. Eng.*, **66**, No. 1: 51 (2022).
22. O. L. Gaidamak, *Tekhnika, Ehnergetyka, Transport APK*, No. 4: 90 (2022) (in Ukrainian).
23. O. Gaidamak, *Tekhnika, Ehnergetyka, Transport APK*, No. 2: 161 (2022) (in Ukrainian).
24. V. Matviychuk, O. Gaidamak, and M. Karpiychuk, *Vibratsiyi v Tekhnitsi ta Tekhnolohiyakh*, No. 2: 65 (2022) (in Ukrainian).
25. M. Pulupec and L. Shvets, *Current Problems of Transport*, 195 (2019).
26. E. Posviatenko, N. Posviatenko, R. Budyak, L. Shvets, Y. Paladiichuk, P. Aksom, I. Rybak, B. Sabadash, and V. Hryhoryshen, *Eastern-European J. Enterprise Technol.*, **5**. No. 12: 48 (2018).

Metallophysics and Advanced Technologies
Металофіз. новітні технол.
Metallofiz. Noveishie Tekhnol.
2025, vol. 47, No. 1, pp. 83–102
https://doi.org/10.15407/mfint.47.01.0083
Reprints available directly from the publisher

PACS numbers: 46.35.+z, 61.72.Ff, 61.72.Mm, 62.20.fq, 81.20.Hy, 81.20.Wk, 83.50.Uv

Investigations on the Microstructure Evolution of Submicrocrystalline Metals Obtained by the Severe Plastic Deformation Method: A Review

B. S. Abdrasilov and B. B. Makhmutov

Karaganda Industrial University,
30 Republic Ave.,
KZ-101400 Temirtau, Republic of Kazakhstan

Currently, submicrocrystalline (SMC) metals and alloys obtained using severe plastic deformation (SPD) techniques are of increasing interest to researchers. In the present work, we focus on the study of materials with a disorientation spectrum dominated by large-angle grain boundaries, *i.e.*, not microfragmented, but nano- and micrograin materials—SMC materials in our terminology. The fundamental importance of the dominance of the high-angle grain boundaries (HAGBs) in the spectrum of grain-boundary disorientations is due to the exceptional role they play in the formation of the unique properties of SMC materials. As it will be shown in this paper, a special property of the HAGBs (in contrast to low-angle grain boundaries) is their ability to transition to a nonequilibrium state during SPD and to maintain this state for a certain time after deformation, which is the cause of many, if not all, special physical and mechanical properties of SMC materials.

Key words: severe plastic deformation, nanostructure, fragmentation, ultrafine-grained structure.

Нині субмікрокристалічні (СМК) метали та стопи, одержані з використанням методів інтенсивного пластичного деформування (ІПД), викликають підвищений інтерес у дослідників. У цій роботі ми зосередимося на

Corresponding author: Bolat Bizhanovych Makhmutov
E-mail: bb.makhmut@tttu.edu.kz

Citation: B. S. Abdrasilov and B. B. Makhmutov, Investigations on the Microstructure Evolution of Submicrocrystalline Metals Obtained by the Severe Plastic Deformation Method: A Review, *Metallofiz. Noveishie Tekhnol.*, **47**, No. 1: 83–102 (2025). DOI: 10.15407/mfint.47.01.0083

вивченні матеріялів зі спектром дезорієнтацій, у якому домінують великокутові межі зерен, тобто не мікрофраґментованих, а нано- і мікрозеренних матеріялів — СМК-матеріялів у нашій термінології. Принципове значення домінування висококутових меж (ВКМ) у спектрі дезорієнтацій меж зерен пов'язане з винятковою роллю, яку вони відіграють у формуванні унікальних властивостей СМК-матеріялів. Як буде показано в даній статті, особлива властивість ВКМ (на відміну від малокутових меж) — їх-ня здатність переходити в нерівноважний стан під час ІПД і зберігати цей стан упродовж певного часу після деформації, що є причиною багатьох, якщо не всіх, особливих фізико-механічних властивостей СМК-матеріялів.

Ключові слова: інтенсивна пластична деформація, наноструктура, фраґментація, ультрадрібнозерниста структура.

(Received 30 January, 2024; in final version, 8 July, 2024)

1. INTRODUCTION

When describing the structure of submicrocrystalline (SMC) materials, it is necessary to pay attention to the special state of other lattice defects—vacancies and dislocations. Although, in contrast to nonequilibrium grain boundaries, the role of these defects in the formation of properties is not determining, a number of peculiarities are observed in their behaviour.

If we start with point defects, first of all, we should note the exceptionally high concentration of nonequilibrium vacancies after SPD. Sometimes their concentration level reaches $C_v = 10^{-4}$ [1, 2]. It should be noted that these nonequilibrium vacancies are quickly annealed at long holding time or temperature increase and their contribution to the changes in the properties of SMC materials is usually insignificant.

Interesting features are also observed in the dislocation subsystem of SMC materials. First, it is a very high density of dislocations, the level of which is of $\sim 10^{15}$ m^2, which is two orders of magnitude higher than the usual one [3–7]. Secondly, due to the small grain size in SMC materials, there are difficulties in the operation of conventional intragrain sources of dislocations. The main mechanism of generation (nucleation) of dislocations in SMC materials is their generation from grain boundaries. This can lead to the emergence of special mesostructural regions—'regions of zero charge', the size of which exceeds the grain size (in contrast to conventional materials, where the region of zero charge, as a rule, is equal to the grain size).

Thirdly, despite the high density of dislocations, due to the small size of grains, very a few dislocations are contained in the grain body, and, during equal-channel angular pressing (ECAP), they do not form complex ensembles and clusters in the lattice and move through the

grains quite freely [8–12].

And, finally, the main thing: not only the generation of dislocations, but also the kinetics of dislocation motion in the grains and their 'disappearance' necessary to provide strain accommodation is determined by the interaction of dislocations with grain boundaries. This process is the key to understand the peculiarities of deformation behaviour of SMC materials.

In the case of SMC materials, all types of defects contribute to the deformation behaviour and structure evolution, but, in our opinion, nonequilibrium grain boundaries play a determining role. The description of the behaviour of nonequilibrium grain boundaries and their interaction with lattice dislocations is the key to understand the structure and properties of SMC materials.

Thus, the object of our study from the structural point of view are materials with a homogeneous submicrocrystalline structure with a spectrum of disorientations dominated by large angular grain boundaries, which (to ensure special physical and mechanical properties of the material) are in a nonequilibrium state.

2. PHYSICAL PROPERTIES OF SMC MATERIALS

Speaking about the physical properties of SMC materials, the most common are physical, electrical and thermal properties.

In Ref. [13, 14], a change—'shift'—of the Curie temperature by 36° (*i.e.*, approximately by $\cong 6\%$) and a 'shift' of the saturation magnetization value (by more than 30%) in the SMC nickel and iron were described. Except for the authors of the above-mentioned works, no one has ever recorded such 'shifts'. In our opinion, the 'effects' detected in [13, 14] are the result of insufficient care in setting up the experiments.

Note that the effect of a change in the Curie temperature was difficult to expect, since phase transitions of the second kind are associated with rearrangements in the electronic subsystem. Such rearrangements are very likely in dislocation nuclei and grain boundaries, but the fraction of the material in them in SMC structures is very small and cannot have a noticeable effect on the results of magnetic property measurements. Note also that, when heated to the Curie temperature (400°C for nickel, for example) due to the intense return of the defect structure, the density of dislocations 'returns' to the usual level, the grain size grows significantly and ceases to be submicron. Thus, any reasonable reason (under any bold assumptions about the role of defects) for the Curie temperature change disappears.

In a number of works [13, 15], another 'shift' has been recorded—a 2–4 times' increase of the coercivity after ECAP.

The 'shift' of the coercive force by several times compared to the undeformed state, as well as the intensive return of the coercive force

value during annealing, are quite typical for highly-deformed structures [16–21] and are not a specific effect related specifically to the ECA deformation and the creation of SMC structures.

It is known that the free path length of electrons in metallic materials, as a rule, does not exceed several nanometres. This value is significantly smaller than the characteristic size of the structural elements of SMC materials ($\cong 100$ nm). This means that the fundamental electrical properties of materials cannot change after ECAP.

In experiments, a noticeable increase ('shift') of electrical resistivity, which sometimes reaches ten percent at room temperature, is often observed. This is because the large density of lattice defects in SMC materials affects the electrical conductivity. The magnitude of the conductivity changes associated with lattice defects can be easily estimated using tabulated values of the resistivity of lattice defects. For copper, for example, the resistivity of defects is equal to the following, respectively: for vacancies, $D_r = 2{\cdot}10^{-8}$ Ohm·m per 1% of vacancies, for, dislocations $D_r = 2.8{\cdot}10^{-19}$ Ohm·cm^3, and for grain boundaries, $D_r \cong 4{\cdot}10^{-12}$ Ohm·cm^2.

At the limiting values of defect concentration in SMC copper, grain size $d \cong 200$ nm, dislocation density $r_v \cong 10^{11}$ cm^2 and vacancy concentration $C_v = 10^{-4}$, the defect-related increase in electrical resistivity at room temperature reaches $\cong 2.5{\cdot}10^{-9}$ Ohm·cm, which is of about 10% of the standard value. The relative contributions of various lattice defects to this change are as follow: the contribution of grain boundaries is of $\cong 2{\cdot}10^{-9}$ Ohm·cm, the contribution of dislocations is of $2.3{\cdot}10^{-10}$ Ohm·cm, and the contribution of vacancies is of about $2{\cdot}10^{-10}$ Ohm·cm.

It follows from the estimates that the main role in the experimentally measured 'shift' of electrical resistivity in SMC materials is played by grain boundaries [22–25].

It also follows from the estimates that the effect of the 'shift' of the electrical resistance level after ECA deformation observed in the experiments is trivially described within the framework of traditional ideas about the influence of defects on the electrical conductivity of metal and is not a specific property of SMC materials.

The thermal properties of SMC materials are usually studied by differential scanning calorimetry (DSC) [1, 2, 26]. The magnitude of heat release during heating of SMC materials with an initial grain size of $\cong 0.1 \times 0.2$ μm^2 is at the level of $\cong 1$ J/g [27]. This is a rather high value and one can speak about some 'shift'. In accordance with classical ideas [42], heat generation during heating is related to the return of defect structure. The contributions of various types of defects to heat release are calculated based on standard estimates of the energy of individual defects. It is known that the energy per unit length of a lattice dislocation is $\approx CA^2/4\pi(1-\nu)\ln(R/r_0)$, and the energy per unit area of a grain boundary is $\gamma_b \approx G_b/24$ [28]. Using these values and determining exper-

imentally the values of structural parameters (grain size and dislocation density), it is not difficult to determine the contributions to heat release associated with each type of defect. The difference between the calculated value and the experimentally measured value is usually associated with the contribution of vacancies. Taking the energy of vacancy formation equal to $\cong 10kT_m$ [45], the corresponding vacancy concentration is determined. In SMC materials, it turns out to be at a high level, but in general, reasonable for highly deformed structures: $C_v \sim 10^{-4}$ [1, 2]. Estimates show that the observed 'shift' in heat release is a trivial effect associated with the increased defectiveness of NMC materials. This is also evidenced by the fact that the shape of the DSC heat release curves (and the scale of the effect) is similar to the DSC curves obtained for conventional highly deformed structures [15].

So, in materials subjected to ECAP, some 'shifts' in the parameters characterizing physical properties are indeed observed, compared to undeformed materials. However, and this is important to emphasize, these changes are quite trivial. They fully correspond to the expected and easily calculated within the framework of classical concepts—changes in structure-sensitive parameters, when defects are introduced into the material. As a rule, the scale of these changes corresponds to the scale of changes in the specified parameters in materials subjected to deformation by other methods. As a rule, the observed 'shifts' are associated not only with the small grain size of SMC materials, but also with an increased density of lattice dislocations and a high concentration of vacancies [29–33].

Thus, the mentioned 'shift effects' of physical properties in SMC materials occur, but are trivial. Note that their study can help in solving problems of estimating the density of individual types of defects, especially, in the case of complex use of different methods.

At the same time, it should be noted that, in SMC materials, a number of effects are observed that are characteristic only of this group of materials. Such effects are observed in SMC materials in the case, when the process under study depends on several parameters, which, in turn, depend differently on the grain size d. In the case, where a change in d leads to multidirectional changes in parameters, a situation is possible, when, at a certain d^*, a maximum or minimum appears in the dependence of process parameters on grain size. An example of such an effect is the behaviour of SMC materials during deformation in the superplasticity regime. This effect is manifested in the fact that maximum plasticity is observed not in metals with smaller grain sizes—as follows from traditional ideas about the mechanisms of superplasticity [34, 35], but in materials with an 'intermediate' grain size d, lying close to $\cong 1$ μm [36–39]. This result is inexplicable within the framework of the classical theory of superplasticity [34, 35].

Another example of a similar effect is the amazing property of some

SMC materials, under tensile conditions at room temperatures, to simultaneously show a significant increase in strength and increase in ductility [3, 40, 41–43]. In conventional materials, an increase in strength, as a rule, leads to a decrease in ductility, and in some SMC materials, and specifically in the grain size range of 0.5–1 μm, a simultaneous increase in strength and ductility at room temperature is observed.

The third example very widely discussed in the literature [44–46] is associated with the behaviour of the yield stress of SMC materials. In accordance with the generally accepted model, the yield strength is related to the grain size by the Hall–Petch relation $\sigma_T = \sigma_0 + K/d^{-1/2}$, and, therefore, a decrease in grain size d should lead to an increase in the yield strength σ_T [44]. However, in the field of SMC materials, this law ceases to be observed. In some cases, a weak dependence of σ_T on d is observed [45, 46], and, in other cases, an inverse relationship is observed: the smaller d, the smaller σ_T [46, 47].

Thus, as can be seen from the brief analysis, SMC materials have special properties and a whole range of specific effects are observed in them, which makes it possible to distinguish these materials into a separate class of structural materials.

Separately, we should touch upon the problem of the formation and thermal stability of the structure of SMC materials during SPD and subsequent annealing. It should be noted that most of the experimental results obtained related to the study of diffusion-controlled processes in SMC materials are incomplete and contradictory. Often, for the same metal obtained by the same SPD method under the same conditions, conflicting data are provided on the influence of grain size and the state of grain boundaries on the nature and kinetics of diffusion-controlled processes, the influence of the structure of grain boundaries on mechanical, diffusion, magnetic, electrical, and other properties. This does not allow us to systematize the results and build correct theoretical models that describe the patterns observed in experiments and provide a satisfactory comparison.

A particularly difficult situation arises in the issue of describing diffusion-controlled processes of grain dispersion, recrystallization and decomposition of the solid solution in SMC materials.

Currently, there is a fairly large number of works in the literature devoted to the study of the laws of the process of dispersion of the structure of metals during SPD [3, 13, 46]. As known, developed plastic deformation is accompanied by intense fragmentation—the formation of misoriented microrange-fragments in the material [48]. As deformation occurs, the misorientation of fragments increases, and their sizes gradually decrease, reaching a certain minimum value d^*, which is usually called the limit of deformation refinement or the limit of grain dispersion [48].

Analysis of literature data [3, 48, 49] shows that the value of the

dispersion limit d^* depends on the structure and properties of the material, as well as on the selected SPD mode: the deformation pattern, its rate and temperature.

One of the most important factors is the deformation temperature. Its influence on the dispersion limit has been studied in detail for the aluminium and magnesium alloys [50, 51]; isolated studies have been carried out for copper [52], iron [53], nickel [54], titanium [55], *etc*. Generalization of these data allows us to conclude that the value of the dispersion limit d^* monotonically increases with increasing deformation temperature.

Studies by a number of authors [3, 51, 52] show that the dependence $d^*(T)$ in some cases has a two-stage character. In the temperature range above temperature T_1, which can conventionally be called the recrystallization temperature during ECAP, d^* increases with increasing temperature very intensively. In a number of works, the authors note a more complex nature of the dependence of d^* on the SPD temperature, which, according to the authors of Ref. [56], is caused by a change in the mechanisms of grain refinement with increasing temperature.

To describe the features of structure formation in metals and alloys during SPD, noteworthy works are those that consider the fragmentation process from the point of view of the concept of dynamic recrystallization during SPD [54], works that describe the process of grain structure refinement and the formation of high-angle grain boundaries using methods for numerical modelling of the nucleation and further development of low-angle subboundaries [57], ideas about the peculiarities of fragmentation processes at the mesolevel, the possibility of calculating the value of the limit of grain dispersion based on ideas about the accommodative nature of the SPD process. They deserve special attention and theoretical works based on the traditional language of the theory of disclinations in solids [58].

Thus, despite a large number of experimental works devoted to studying the process of formation of SMC structures using SPD methods, the question of the mechanisms of fragmentation of the grain structure of metals and alloys, as well as the question of the reasons for the existence of the grinding limit and the theoretical calculation of its value have not yet been resolved. In our opinion, among the key theoretical questions, which should be clarified in this discussion, is the question of the mechanism of formation of large grain boundaries during SPD, without an answer to which, further discussion about the mechanisms of fragmentation during SPD is very difficult [59–63].

3. CONTINUOUS DYNAMIC RECRYSTALLIZATION

In recent years, a large amount of experimental evidence has appeared for the formation of *BAB* during deformation through the rotation of

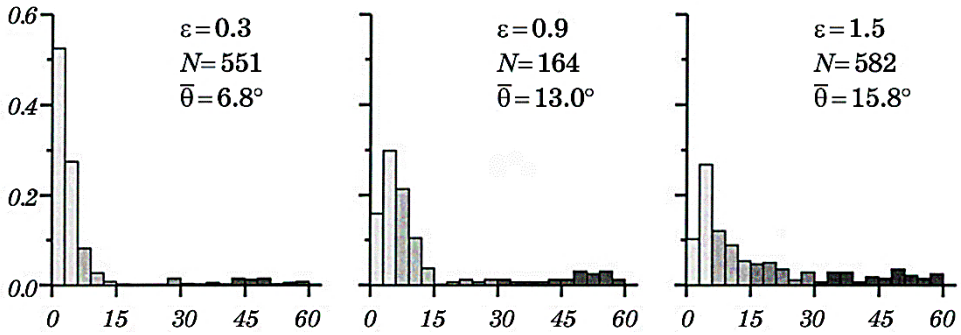

Fig. 1. Increase in the misorientation angle of grains with increasing degree of hot deformation in the aluminium–copper alloy (ε is the degree of deformation, N is the number of measurements, $\bar{\theta}$ is the average misorientation angle) [65].

subgrains (Fig. 1). In this case, the microstructure is formed quite homogeneous throughout the entire volume of the material, and it is difficult to identify specific places of nucleation and growth of nuclei. This phenomenon is classified as continuous dynamic recrystallization (CDR) [64]. The phenomenon of CDR has been much less studied compared to DDR; this is due both to the difficulties of identifying the onset of recrystallization (the study became possible only with the development of EBSD technology) and to the need to create a high level of deformation in the material, which is not realized in simple tensile or compression experiments. Most often, an SPD is required to begin the CDR process. To date, the overwhelming number of works devoted to the study of CDR processes is related to SPD processes.

Basic experimental facts about CDR (Fig. 2) [66] are as follow.

1) LPC has the form of a curve with saturation (Fig. 2, *a*), in some materials the appearance of one peak is observed, but more often there is no peak. The total strain accumulated over several cycles is most often plotted along the strain axis. The flow stress at the steady stage decreases with increasing temperature [66] increases with increasing strain rate [67] and does not depend on the initial grain size [68].

2) The average value of grain misorientation increases with increasing degree of deformation; low deformation rates accelerate this process [69]. However, there are stable misorientations that do not transform into HAGBs [66] (Fig. 2, *b*).

3) The transformation of LAB into HAGBs occurs as a result of a gradual increase in misorientations (HIM), rotation of the lattice near the grain boundary (LRCA) or the formation of microbend bands (MSBs), as shown schematically in Fig. 2, *c* [70].

4) The average grain size decreases with increasing deformation and reaches a saturation value at high degrees of deformation (Fig. 2, *d*). In

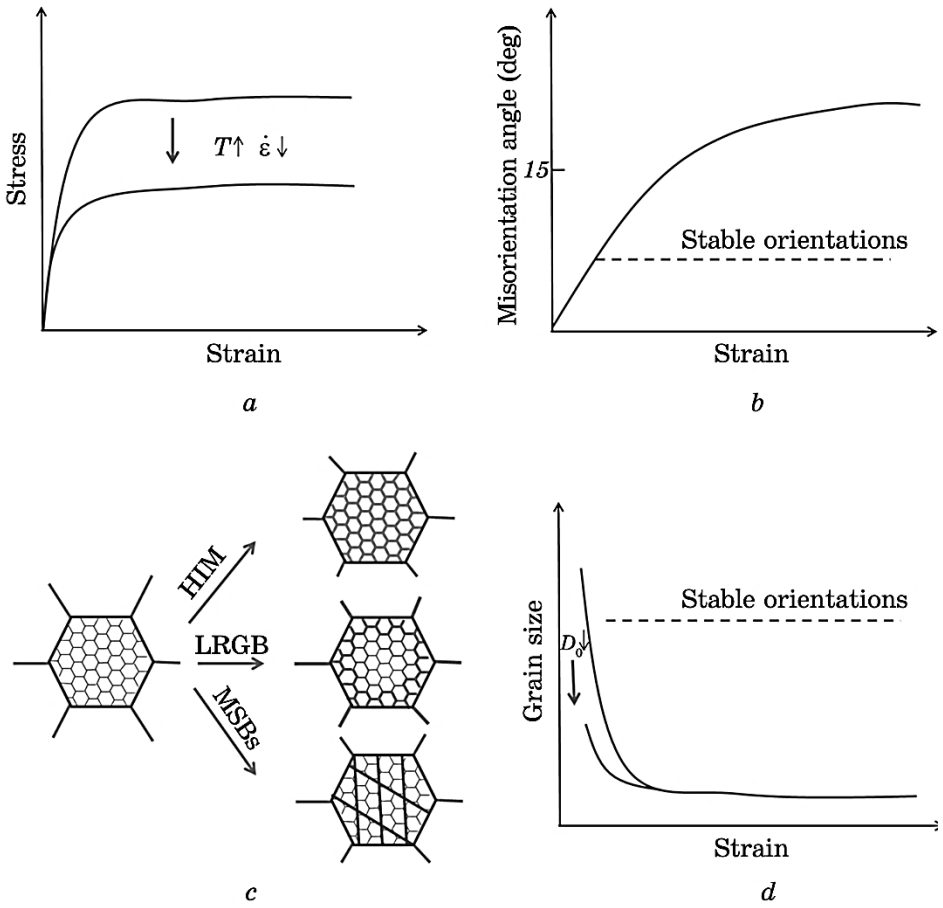

Fig. 2. Schematic representation of typical experimentally observed phenomena during CDR: DDR (*a*); change in the average value of CA rotation at elevated ($> 0.5T_m$) temperatures (*b*); transformation of LAGBs into HAGBs with a homogeneous increase in the misorientation angle, rotation of the lattice in the boundary region, or formation of ROP (thin lines indicate LAGBs, thick lines indicate HAGBs) (*c*); evolution of the average grain size with increasing degree of deformation (*d*) [71].

this case, the preservation of individual initial grains, favourably oriented to stress, is observed, even at high degrees of deformation. Reducing the initial grain size can lead to acceleration of the kinetics of grain refinement at high degrees of deformation. In this case, the method of strain accumulation has a very weak effect on the kinetics of the CDR process [65].

5) At high degrees of deformation during CDR, a strong crystallographic texture is formed in the material [65, 72].

CDR with a Gradual Increase in Grain Misorientation. At relatively high deformation temperatures ($> 0.5T_m$), as a rule, a homogeneous microstructure is formed; deformed grains or shear bands are formed less frequently than during cold deformation. Under these conditions, the CDR process begins due to the accumulation of dislocations in the MG, because of which their misorientation increases until a critical angle is reached ($\cong 15°$). Since it is difficult to track changes in the misorientation of an individual boundary, as a rule, they talk about the average value for the ensemble. A similar mechanism is observed experimentally both during deformation of a polycrystalline material and in the case of single crystals.

This type of dynamic recrystallization (DR) is observed during SPD with degrees of deformation of 2 and higher. The mechanism of occurrence is the formation of dislocation cells, which are transformed with increasing degree of deformation into subgrains and finally into grains (Fig. 3). Figure 3 shows the experimental dependences of grain size, average grain misorientation angle, and dislocation density at subboundaries during hot all-round forging of pure copper [72].

CDR during Progressive Lattice Rotation near Grain Boundaries. There is evidence that CDR can occur through progressive rotation of subgrains adjacent to pre-existing grain boundaries. This process is similar to the so-called rotational recrystallization described for many

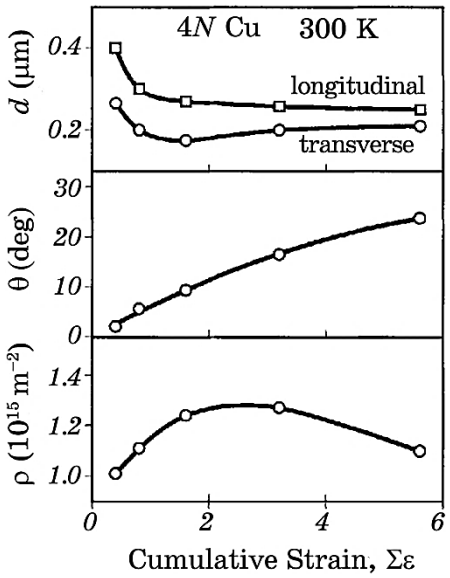

Fig. 3. Dependences of grain size, average grain misorientation angle and dislocation density in subboundaries during hot all-round forging of pure 4*N* copper [72].

crystalline materials [73].

Today, a simple mechanism has been proposed to explain the formation of new grains during hot deformation of h.c.p. metals (Fig. 4) [74]. Deformation in h.c.p. materials is inhomogeneous due to the absence of independent slip systems; therefore, local shear often begins near the grain boundary (Fig. 4, *a*). As the local shear develops, the CA rotates. In this case, the flowing DW (Fig. 4, *b*) promotes the formation of new small subgrains near the original CA (Fig. 4, *c*). As a result, the accumulation of a large number of subgrains leads to their merging and the formation of new grains surrounded by HAGBs. Figure 5 shows photographs of the microstructure formed according to the above mechanism [69, 74].

In Ref. [75], models of CDR micromechanisms were developed that predict the grain size distribution, the evolution of the misorientation angle, the crystallographic texture, and the strain hardening of the material during hot intense deformation. The main assumption of these models is that the lattice inside the individual grain is not homogeneous during severe deformation. Near the grain boundary, local lattice distortions arise due to the accumulation in the grain bounda-

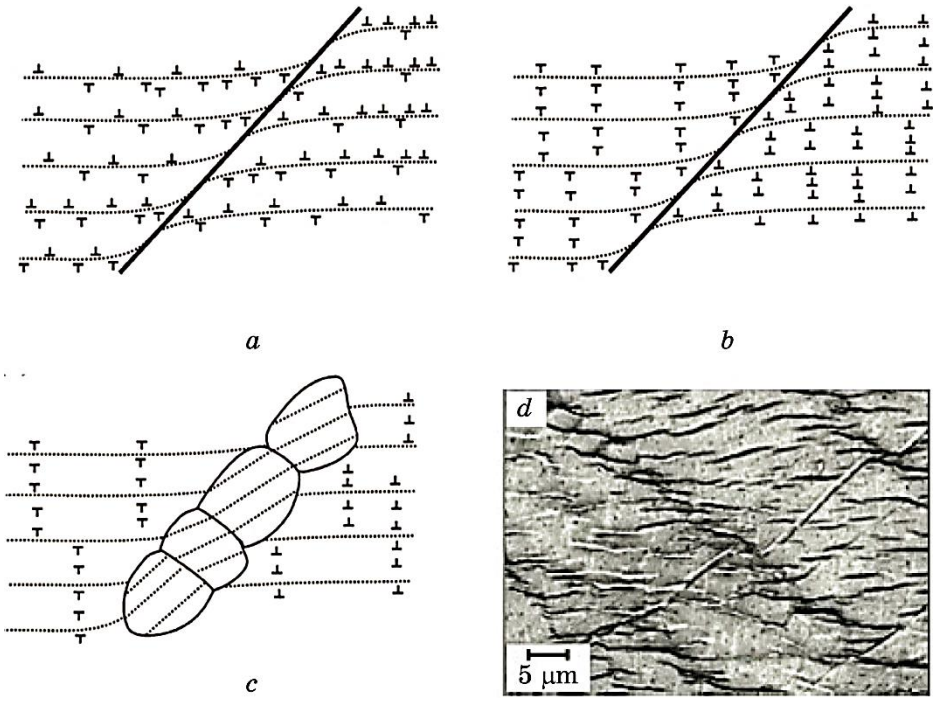

Fig. 4. Schematic representation of the formation of a chain of small grains along the CA in magnesium [74].

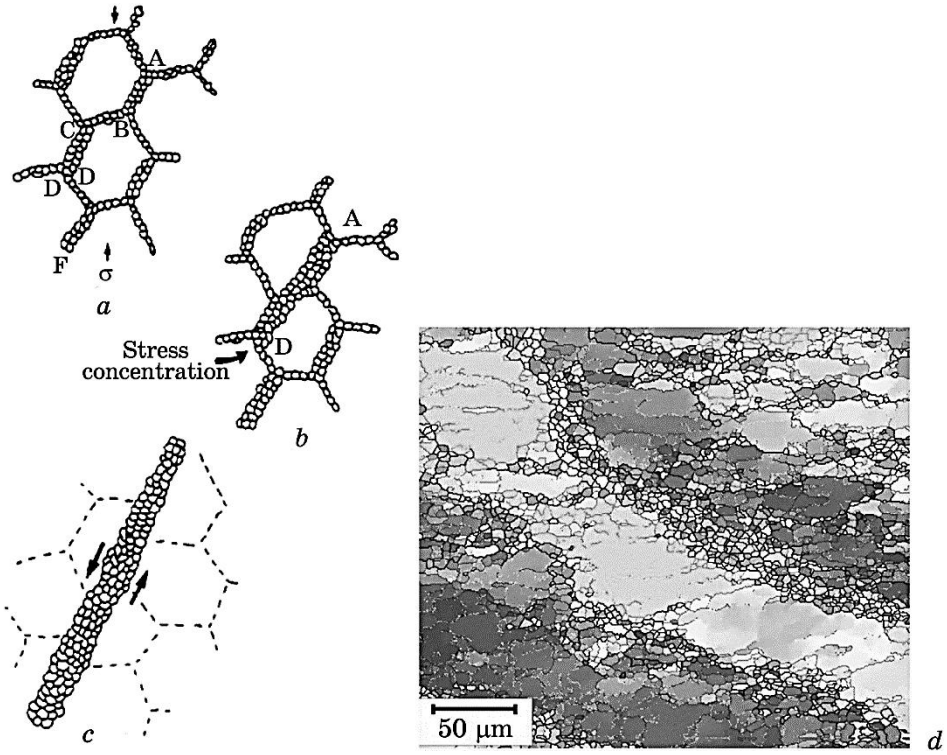

Fig. 5. Formation of a strip of small grains along the boundaries according to the mechanism shown in Fig. 4 [74] (*a*–*c*); EBSD maps of the grain structure of a magnesium alloy [69] (*d*).

ries of products of delocalization of defects that enter the boundary during the deformation process. These distortions increase as the degree of deformation increases (Fig. 6). When a certain critical degree of bending is reached, because of rotation of the central part, the centre and periphery are separated by a boundary. The constructed model well describes the flow of CDR in aluminium alloys. Figure 7 shows a TEM image of the crystal structure of the material, showing lattice distortion near the CA [76]. It is shown that the real deviation of the plane from the straight line can reach 5°.

CDR occurring in the presence of microshear bands (MSBs). The formation of MSBs during hot deformation is observed in images obtained using optical, scanning and transmission microscopy, as well as EBSD [64, 74, 77].

Numerous MSBs, forming in the grain body, lead to the appearance of a MSB network, creating misoriented fragments with their intersections (Figs. 8, 9) [77]. Further deformation leads to an intensive increase in the number of MSBs and the formation of LAGBs and HAGBs

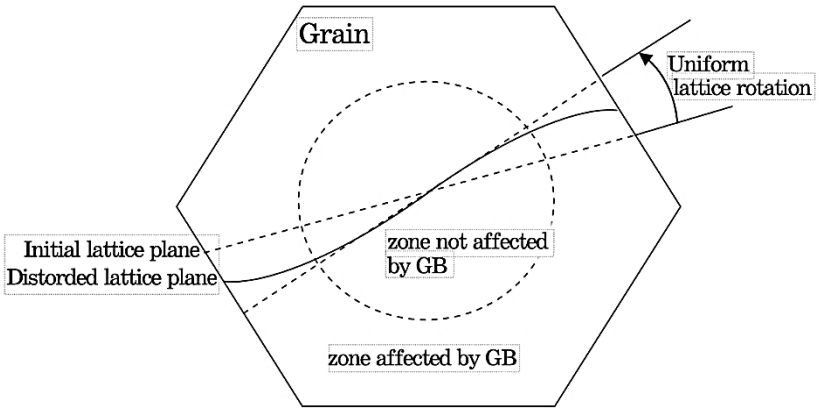

Fig. 6. Scheme of curvature of the crystallographic plane during grain rotation [75].

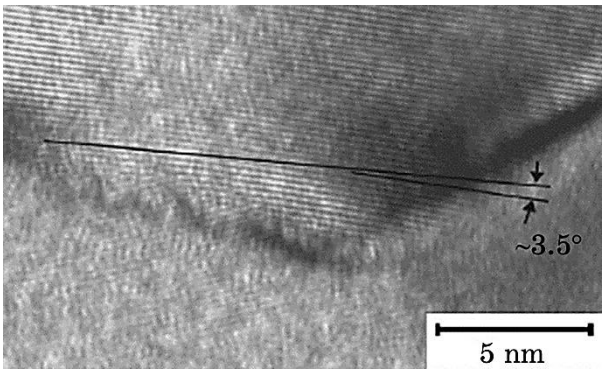

Fig. 7. Experimental confirmation of the basic assumption of the Tyth model [76].

between the fragments. Thus, the proportion of equiaxed grains of small size increases, gradually filling the entire volume.

It has been shown that a similar mechanism for the nucleation of small grains is observed, when the direction of deformation changes. ECAP can be considered the most striking example in this case.

4. GEOMETRIC DYNAMIC RECRYSTALLIZATION

The geometric dynamic recrystallization (GDR) process has been described in a wide range of metallic materials, including pure metals, solid-solution strengthened alloys, and particle-strengthening materials [78–81]. Moreover, although a number of authors combine GDR

with CDR, there are differences between these processes [71, 82].

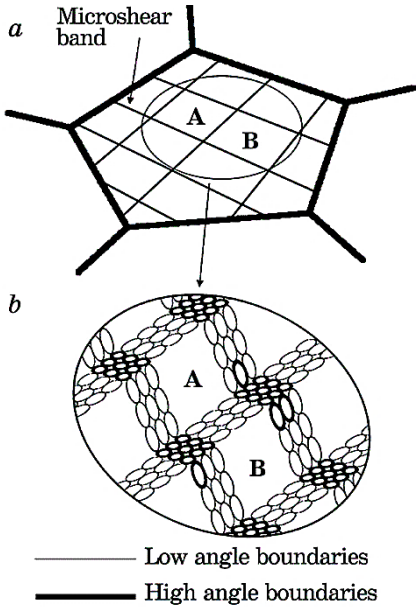

Fig. 8. Scheme of the formation of a fine-grained structure, when crossing the MSB [69].

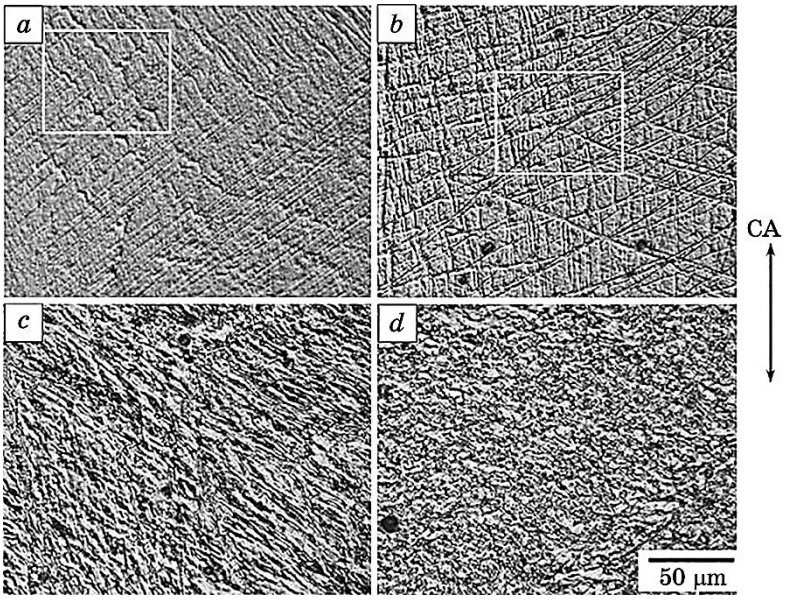

Fig. 9. Experimental observation of the formation of new small grains at the intersection of MSB [69].

Below, there are the main experimental characteristics of the GDR.

1. GDR is most often observed for materials with medium and high SFE, deformed at elevated temperatures with a low deformation rate. At low temperatures, the DB dominates, since the steps on the CA limit their mobility. At very high temperatures, grain boundaries are so mobile that hardening does not have time to generate new grains. Thus, to implement GDR, a certain temperature optimum is required [78].

2. Subgrains are formed after reaching a critical level of deformation and remain constant in size throughout the entire deformation process. The size of subgrains at the saturation stage decreases with increasing parameter 3-X [83].

3. The amount of misorientation of part of the subgrains at the saturation stage during GDR differs significantly from that observed in the case of CDR and remains constant at a level of about 2°. In the case of GDR, a bimodal distribution of grain misorientations is always observed [84].

4. During the GDR process, the original texture remains virtually unchanged. In some experiments, a slight softening of the texture is observed, which leads to a smoothing of the LPC peak [78].

GDR is described as the process of formation of equiaxed grains during hot deformation under the following conditions:

1. presence of a selected direction of deformation;
2. CA can migrate to form steps;
3. during the deformation process, grain thinning is observed in one or two directions;
4. bends on the *BAB* can interact, when the grain width reaches 2–3 subgrain sizes.

The above-mentioned GDR mechanism is based only on the idea of microstructure evolution depending on the initial grain size and the selected direction of stress application. In reality, there are also some other aspects that need to be taken into account.

Firstly, during deformation, bends should form on the grain boundaries, which cannot be taken into account, when modelling grains as spheres or cubes. Let us consider the process of bending formation. During hot deformation, subgrain boundaries first appear near the initial boundaries. Steps appear on both sides of the boundary in the process of local migrations of grain boundaries at the junctions with subgrain boundaries formed during DV. Since the grain thickness is not constant along the long axis, GDR does not occur simultaneously upon reaching a critical level of deformation. Some parts of the grain reach critical stress earlier and, in them, GDR begins first. Secondly, a high degree of deformation in the selected direction is required [84].

Although the mechanisms of GDR are mostly understood and have been experimentally discovered in many metals and alloys, attempts to

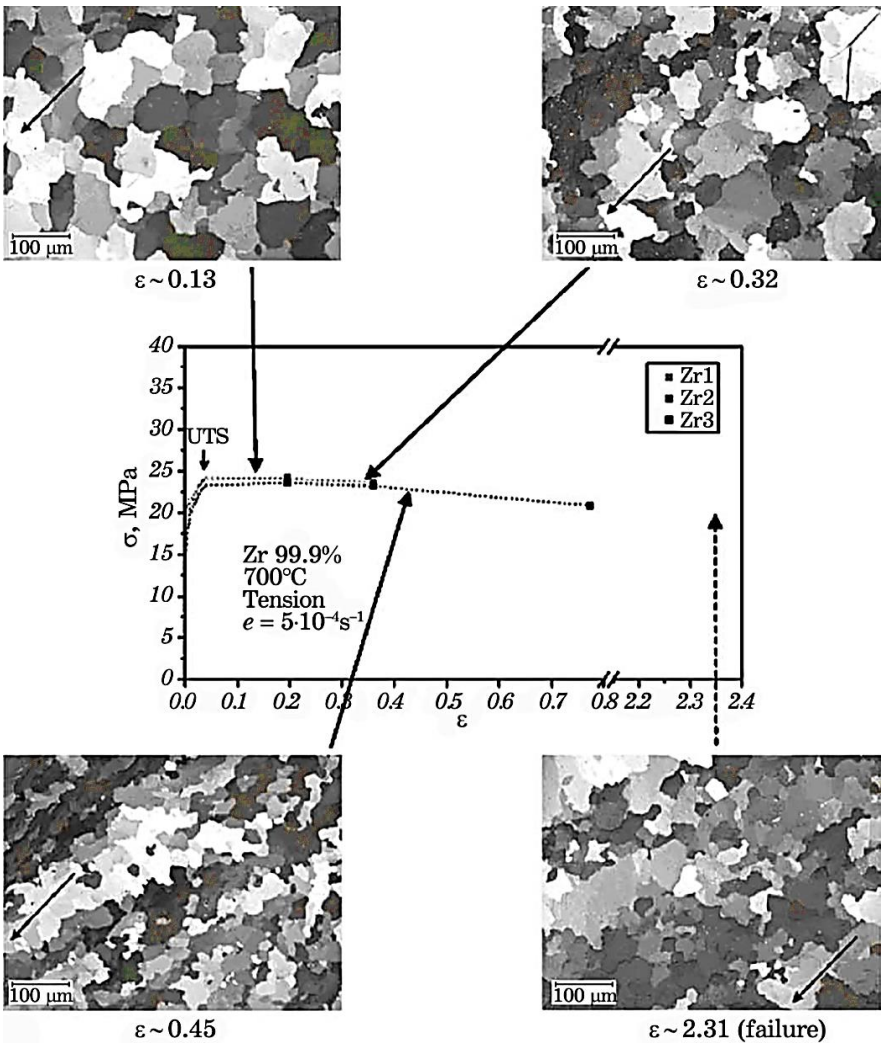

Fig. 10. Evolution of the α-Zr microstructure during rolling at 700°C [86].

construct a model of this process are based not on physical, but on geometric principles [82]. In general, these models predict microstructure evolution well.

Figure 10 shows snapshots of the microstructure evolving during the GDR process [86].

5. CONCLUSION

The results of studies of the influence of the structural state of grain

boundaries of SMC metals on the peculiarities of the return and recrystallization processes during annealing can be used to determine the optimal modes of equal-channel angular pressing and heat treatment of SMC metals. Optimal modes of production and processing of metals and alloys allow to ensure the formation of SMC structure with high thermal stability (high temperature of the beginning of recrystallization), low tendency to abnormal grain growth leading to the formation of inhomogeneous (heterogeneous) structure, high strength characteristics, *etc*.

REFERENCES

1. D. Setman, E. Schafler, E. Korznikova, and M. J. Zehetbauer, *Mater. Sci. Eng. A*, **493**: 116 (2008).
2. W. Q. Cao, C. F. Gu, E. V. Pereloma, and C. H. J. Davies, *Mater. Sci. Eng. A*, **492**: 74 (2008).
3. A. Volokitin, A. Naizabekov, I. Volokitina, and A. Kolesnikov, *J. Chem. Technol. Metall.*, **57**, Iss. 4: 809 (2022).
4. I. E. Volokitina, *Met. Sci. Heat Treat.*, **63**, Nos. 3–4: 163 (2021).
5. A. B. Naizabekov, S. N. Lezhnev, and I. E. Volokitina, *Met. Sci. Heat Treat.*, **57**, Nos. 5–6: 254 (2015).
6. A. Naizabekov, A. Arbuz, S. Lezhnev, E. Panin, and I. Volokitina, *Phys. Scr.*, **94**, No. 10: 105702 (2019).
7. I. E. Volokitina and A. V. Volokitin, *Metallurgist*, **67**: 232 (2023).
8. I. Volokitina, A. Bychkov, A. Volokitin, and A. Kolesnikov, *Metallogr., Microstruct., Anal.*, **12**: 564 (2023).
9. S. Lezhnev, I. Volokitina, and T. Koinov, *J. Chem. Technol. Metall.*, **49**, Iss. 6: 621 (2014).
10. I. Volokitina, *J. Chem. Technol. Metall.*, **55**, Iss. 2: 479 (2020).
11. A. Naizabekov, S. Lezhnev, E. Panin, A. Arbuz, T. Koinov, and I. Mazur, *J. Mater. Eng. Perform.*, **28**: 200 (2019).
12. B. Sapargaliyeva, A. Agabekova, G. Ulyeva, A. Yerzhanov, and P. Kozlov, *Case Studies in Construction Materials*, **18**: e02162 (2023).
13. R. Z. Valiev and I. V. Alexandrov, *Nanostrukturirovannyye Materialy, Polucheennyye Metodom Intensivnoy Plasticheskoy Deformatsii* [Nanostructured Materials Obtained by Severe Plastic Deformation] (Moskva: Logos: 2000) (in Russian).
14. R. Z. Valiev, A. V. Korznikov, and R. R. Mulyukov, *Fiz. Met. Metalloved.*, **76**, No. 4: 70 (1992) (in Russian).
15. K. Y. Mulyokov, G. F. Korznikova, R. Z. Abdulov, and R. Z. Valiev, *J. Magn. Magn. Mater.*, **89**: 207 (1990).
16. M. Latypova, V. Chigirinsky, and A. Kolesnikov, *Prog. Phys. Met.*, **24**, No. 1: 132 (2023).
17. N. Vasilyeva, R. Fediuk, and A. Kolesnikov, *Materials*, **15**: 3975 (2022).
18. I. E. Volokitina, *Met. Sci. Heat Treat.*, **62**: 253 (2020).
19. I. E. Volokitina, A. V. Volokitin, and E. A. Panin, *Prog. Phys. Met.*, **23**, No. 4: 684 (2022).
20. A. Naizabekov, A. Volokitin, and E. Panin, *J. Mater. Eng. Perform.*, **28**: 1762

(2019).
21. I. Volokitina, A. Volokitin, A. Denissova, Y. Kuatbay, and Y. Liseitsev, *Case Studies in Construction Materials*, **19**: e02346 (2023).
22. V. V. Chigirinsky and Y. S. Kresanov, *Metallofiz. Noveishie Tekhnol.*, **45**, No. 4: 467 (2023).
23. E. Panin, Z. Gelmanova, and Y. Liseitsev, *Case Studies in Construction Materials*, **19**: e02609 (2023).
24. N. Zhangabay, I. Baidilla, A. Tagybayev, Y. Anarbayev, and P. Kozlov, *Case Studies in Construction Materials*, **18**: e02161 (2023).
25. A. Nayzabekov and I. Volokitina, *Phys. Met. Metallogr.*, **120**: 177 (2019).
26. N. M. Amirkhanov, R. K. Islamgaliev, and R. Z. Valiev, *Phys. Met. Metallogr.*, **86**: 296 (1998).
27. M. Goto, S. Z. Han, T. Yakushiji, S. S. Kim, and C. Y. Lim, *Int. J. Fatigue*, **30**: 1333 (2008).
28. M. F. Ashby, C. Gandli, and D. M. R. Taplin, *Acta Metall.*, **27**: 699 (1979).
29. I.E. Volokitina, *Prog. Phys. Met.*, **24**, No. 3: 593 (2023).
30. I. Volokitina, A. Volokitin, and D. Kuis, *J. Chem. Technol. Metall.*, **56**: 643 (2021).
31. I. E. Volokitina and G. G. Kurapov, *Met. Sci. Heat Treat.*, **59**, Nos. 11–12: 786 (2018).
32. S. Lezhnev, E. Panin, and I. Volokitina, *Adv. Mat. Res.*, **814**: 68 (2013).
33. S. Lezhnev, A. Naizabekov, E. Panin, and I. Volokitina, *Procedia Eng.*, **81**: 1499 (2014).
34. T. G. Nieh, D. Wadsworth, and O. D. Sherby, *Superplasticity in Metals and Ceramics* (Cambridge: Cambridge Univ. Press: 1997).
35. V. N. Perevezentsev, V. V. Rybin, and V. N. Chuvil'deev, *Acta Metall. Mater.*, **40**: 887 (1992).
36. R. K. Islamgaliev, N. F. Yunusova, R. Z. Valiev, N. K. Tsenev, V. N. Perevezentsev, and T. G. Langdon, *Scr. Mater.*, **49**, Iss. 5: 467 (2003).
37. R. K. Islamgaliev, N. F. Yunusova, and R. Z. Valiev, *Nanostructures Materials by High-Pressure Revere Plastic Deformation* (Springer: 2006), p. 299–304.
38. S. H. Kang, Y. S. Lee, and J. H. Lee, *J. Mater. Process. Technol.*, **201**: 436 (2008).
39. A. V. Sergueeva, N. A. Mara, R. Z. Valiev, and A. K. Mukherjee, *Mater. Sci. Eng. A*, **410–411**: 413 (2005).
40. R. Z. Valiev and I. V. Aleksandrov, *Doklady Physics*, **46**: 633 (2001).
41. A. Yamashita, Z. Horita, and T. G. Langdon, *Mater. Sci. Eng. A*, **300**: 142 (2001).
42. H. K. Kim and W. J. Kim, *Mater. Sci. Eng. A*, **385**: 300 (2004).
43. Y. Wang, M. Chen, F. Zhou, and E. Ma, *Nature*, **419**: 912 (2002).
44. A. P. Zhilyaev, A. A. Gimazov, E. P. Soshnikova, A. Rezesz, and T. G. Langdon, *Mater. Sci. Eng. A*, **489**: 207 (2008).
45. E. Shafler and R. Pippan, *Mater. Sci. Eng. A*, **387–389**: 799 (2004).
46. H. Conrad and K. Jung, *Scr. Mater.*, **53**: 581 (2005).
47. M. A. Meyers, A. Mishra, and D. J. Benson, *Prog. Mater. Sci.*, **51**: 427 (2006).
48. V. M. Segal, *Mater. Sci. Eng. A*, **197**: 157 (1995).
49. V. Y. Gertsman, R. Birringer, R. Z. Valiev, and H. Gleiter, *Scr. Met. Mat.*, **30**: 229 (1994).
50. A. Goloborodko, O. Sitdikov, R. Kaibyshev, H. Miura, and T. Sakai, *Mater. Sci.*

Eng. A, **381**: 121 (2004).
51. Y. C. Chen, Y. Y. Huang, C. P. Chang, and P. W. Kao, *Acta Mater.*, **51**: 2005 (2003).
52. W. H. Huang, C. Y. Yu, P. W. Kao, and C. P. Chang, *Mater. Sci. Eng. A*, **356**: 321 (2004).
53. D. H. Shin, J. J. Pak, Y. K. Kim, K. T. Park, and Y. S. Kim, *Mater. Sci. Eng. A*, **325**: 31 (2002).
54. S. Lezhnev and A. Naizabekov, *J. Chem. Technol. Metall.*, **52**, No. 4: 626 (2017).
55. G. I. Raab, E. P. Soshnikova, and R. Z. Valiev, *Mater. Sci. Eng. A*, **387–389**: 674 (2004).
56. V. M. Segal, I. J. Beyerlein, C. N. Tome, V. N. Chuvil'deev, and V. I. Kopylov, *Fundamentals and Engineering of Severe Plastic Deformation* (New York: Nova Science Publishers: 2010).
57. V. N. Perevezentsev and G. F. Sarafanov, *Rev. Adv. Mater. Sci.*, **30**: 73 (2012).
58. S. V. Bobylev, M. Yu. Gutkin, and I. A. Ovid'ko, *Acta Mater.*, **52**: 3793 (2004).
59. A. Volokitin, I. Volokitina, and E. Panin, *Metallogr., Microstruct., Anal.*, **11**, No. 4: 673 (2022).
60. S. Lezhnev, A. Naizabekov, I. Volokitina, and A. Volokitin, *Procedia Eng.*, **81**: 1505 (2014).
61. I. E. Volokitina, *Met. Sci. Heat Treat.*, **61**: 234 (2019).
62. S. N. Lezhnev, I. E. Volokitina, and A. V. Volokitin, *Phys. Met. Metallogr.*, **118**, No. 11: 1167 (2017).
63. I. Volokitina, *J. Chem. Technol. Metall.*, **57**: 631 (2022).
64. T. Sakai, A. Belyakov, R. Kaibyshev, H. Miura, and J. J. Jonas, *Prog. Mater. Sci.*, **60**: 13 (2014).
65. S. Gourdet and F. Montheillet, *Mat. Sci. Eng.*, **283**, Iss. 1–2: 274 (2000).
66. A. Galiyev, R. Kaibyshev, and G. Gottstein, *Acta Mater.*, **49**, Iss. 7: 1199 (2001).
67. Y. Huang and F.J. Humphreys, *Acta Mater.*, **47**, Iss. 7: 2259 (1999).
68. A. Belyakov, K. Tsuzaki, H. Miura, and T. Sakai, *Acta Mater.*, **51**, Iss. 3: 847 (2003).
69. O. Sitdikov, T. Sakai, A. Goloborodko, H. Miura, and R. Kaibyshev, *Philos. Mag.*, **85**, No. 11: 1159 (2005).
70. W. Liu, D. Juul Jensen, and J. J. Morris, *Acta Mater.*, **49**: 3347 (2001).
71. K. Huang and R. E. Loge, *Mater. Des.*, **111**: 548 (2016).
72. A. Belyakov, T. Sakai, H. Miura, and K. Tsuzaki, *Philos. Mag. A*, **81**: 2629 (2001).
73. S. White, *Proc. R. Soc. A*, **283**: 69 (1976).
74. S. E. Ion, F. J. Humphreys, and S. H. White, *Acta Metall.*, **30**: 1909 (1982).
75. L. S. Tyth, Y. Estrin, R. Lapovok, and C. Gu, *Acta Mater.*, **58**, Iss. 5: 1782 (2010).
76. A. Belyakov, Y. Kimura, Y. Adachi, and K. Tsuzak, *Mater. Trans.*, **45**, Iss. 9: 2812 (2004).
77. T. Sakai, A. Belyakov, and H. Miura, *Metall. Mater. Trans. A*, **39**: 2206 (2008).
78. A. Gholinia, F. Humphreys, and P. Prangnell, *Acta Mater.*, **50**, Iss. 18: 4461 (2002).
79. I. E. Volokitina and A. V. Volokitin, *Phys. Met. Metallogr.*, **119**: 917 (2018).
80. G. Kurapov, E. Orlova, I. Volokitina, and A. Turdaliev, *J. Chem. Technol. Metall.*, **51**: 451 (2016).

81. A. V. Volokitin, I. E. Volokitina, and E. A. Panin, *Prog. Phys. Met.*, **23**, Iss. 3: 411 (2022).
82. L. E. Murr, C. S. Niou, J. C. Sanchez, and L. Zernow, *Scripta Met. et Mat.*, **32**: 31 (1995).
83. H. J. McQueen, O. Knustad, N. Ryum, and J. K. Solberg, *Scr. Metall.*, **19**: 73 (1985).
84. G. A. Henshall, M. E. Kassner, and H. J. McQueen, *Metall. Mater. Trans. A*, **23**: 881 (1992).
85. F. J. Humphreys, P. B. Prangnell, J. R. Bowen, A. Gholinia, and C. Harris, *Philos. Trans. R. Soc. A*, **357**, Iss. 1756: 1663 (1999).
86. M. E. Kassner and S. R. Barrabes, *Mater. Sci. Eng. A*, **410**: 152 (2010).

Metallophysics and Advanced Technologies
Металофіз. новітні технол.
Metallofiz. Noveishie Tekhnol.
2025, vol. 47, No. 1, pp. 103–123
https://doi.org/10.15407/mfint.47.01.0103
Reprints available directly from the publisher

PACS numbers: 61.46.Hk, 62.23.Pq, 65.80.-g, 68.35.Np, 81.05.-t, 82.35.Gh

Estimation of the Stress-Intensity Factor Value in the Presence of an Adhesive Defect for a Damaged Plate Repaired with a Composite Patch

A. Houari[*, **], K. Madani[**], M. Benyettou[**], N. Kaddouri[**], M. Belhouari[**], S. Amroune[***], B. Mohamad[****], B. Benamar[**], and A. Chellil[*]

[*]*Laboratory of Motor Dynamics and Vibroacoustics (LDMV), M'hamed Bougara University of Boumerdes, Boumerdes, Algeria*
[**]*Laboratory Mechanics of Structures and Solids (LMSS), DJILLALI LIABES University, Algeria*
[***]*Laboratory of Materials and Structural Mechanics (LMMS), M'sila University, Algeria*
[****]*Department of Petroleum Technology, Koya Technical Institute, Erbil Polytechnic University, IQ-44001 Erbil, Iraq*

Since the implementation of the process for repairing damage in aeronautical structures, the composite patch repair process continues to show its performance with respect to reducing the concentration of stresses in the vicinity of geometric discontinuities and, therefore, ensures a long lifespan of the repaired structure. Despite the advantages, which this process represents compared to conventional riveting, bolting and welding processes, this process still remains applicable for secondary structures. In fact, the exposure of the adhesive to temperature and humidity and the existence of flaws within the adhesive layer remain a major problem of its use. Indeed, during the implementation of this process, several defects are

Corresponding author: Kouider Madani
E-mail: kouider.madani@univ-sba.dz

Citation: A. Houari, K. Madani, M. Benyettou, N. Kaddouri, M. Belhouari, S. Amroune, B. Mohamad, B. Benamar, and A. Chellil, Estimation of the Stress-Intensity Factor Value in the Presence of an Adhesive Defect for a Damaged Plate Repaired with a Composite Patch, *Metallofiz. Noveishie Tekhnol.*, **47**, No. 1: 103–123 (2025). DOI: 10.15407/mfint.47.01.0103

likely to become integrated into the adhesive layer (cavities, cracks, air bubbles, *etc.*) during the preparation of the surface of the damaged plate; this can lead to inadequate load transfer from the adhesive to the patch. The analysis of the effect of the presence of this type of defect is important for the evaluation of the different constraints in the different substrates. Our work is part of this context; its aim is to employ the finite-elements' method to examine the mechanical response of a 2024-T3 aluminium plate, which has been damaged and repaired using a composite patch subjected to tensile stress in the existence of a bonding defect with a square shape. The study takes into consideration notch and crack interaction effect in the damaged plate, on the one hand, and the position of the bonding defect, on the other hand. Several factors are highlighted, namely, the crack length, the applied load and defect position. The investigation of the stress-intensity factor and the stresses within the assembly substrates illustrates their dependence on various parameters, particularly, the defect position of the bonding.

Key words: stress-intensity factor composite patch, von Mises stress, shear stress, peel stress, bonding defect.

З моменту впровадження процесу ремонту пошкоджень в авіяційних конструкціях процес композитної латки продовжує демонструвати свою ефективність щодо зменшення концентрації напружень поблизу геометричних нерівностей і, таким чином, забезпечує тривалий термін служби відремонтованої конструкції. Незважаючи на переваги, які цей процес має порівняно з традиційними процесами заклепування, болтового з'єднання та зварювання, він все ще залишається прийнятним для вторинних конструкцій. Насправді, вплив температури та вологости на клей, а також наявність дефектів у адгезійному шарі залишаються основними проблемами його використання. Дійсно, під час реалізації цього процесу існує ймовірність вбудовування у адгезійний шар декількох дефектів (порожнин, тріщин, бульбашок повітря тощо) під час підготовки поверхні пошкодженої пластини, що може привести до невідповідної передачі навантаження від адгезиву до латки. Аналіза впливу наявности такого типу дефектів є важливою для оцінки різних обмежень на різних підкладинках. Наша робота є частиною цього контексту; її метою є використання методу скінченних елементів для дослідження механічної реакції алюмінійової пластини 2024-T3, яку було пошкоджено та відремонтовано за допомогою композитної латки, що піддавалася розтягуванню за наявности дефекту зчеплення квадратної форми. Дослідження враховує ефект взаємодії надрізу та тріщини в пошкодженій пластині, з одного боку, і положення дефекту зчеплення, з іншого боку. Було виділено декілька чинників, а саме, довжину тріщини, прикладене навантаження та положення дефекту. Дослідження коефіцієнта інтенсивности напружень і напружень у складальних підкладинках ілюструє їхню залежність від різних параметрів, зокрема від положення дефекту зчеплення.

Ключові слова: коефіцієнт інтенсивности напружень, композитна латка, фон Мізесові напруження, напруження зсуву, напруження відша-

рування, дефект зчеплення.

(Received 28 April, 2024; in final version, 9 July, 2024)

1. INTRODUCTION

At present, all structures used in the various aeronautical and construction sectors present geometric discontinuities such as cracks, notches, delaminating and cavities, which are the cause of reduced structural life under mechanical or thermal stress. Once damage has been detected in the material, depending on its critical size, engineers must decide whether or not to repair the structure. Various solutions were presented, including the patch repair process, which offers several advantages over bolting, riveting and welding to improve the durability of the part. This method exhibits greater structural efficiency, with less structural damage than others. Several researchers have sought to develop a composite patch [1, 2] capable of transferring maximum stress from the damaged zone by optimizing its mechanical properties, shape, dimensions and above all the nature and volume fraction of the fibre, in order to provide high resistance to damaged structures, taking into account all the influencing parameters (mechanical load, humidity, temperature, *etc.*).

The patch repair technique, known for its effectiveness, offers several advantages over other techniques. Patching generally involves covering or reinforcing a damaged area with a similar or compatible material to restore its functionality and improve the life of the structure. The patch material minimally impacts static strength but significantly influences fatigue resistance [2]. The technique can be carried out by bolting, riveting or welding for metal alloys, but experimental, numerical and analytical studies have demonstrated the effectiveness of bonded patch repairs in composites for controlling crack propagation in thin plates [3]. Tsamasphyros *et al.* [4] conducted a study on composite patch repair using both analytical and numerical approaches. Wang *et al.* [5] investigated the analytical method for stepwise patch repair.

The most widely adopted repair method involves bonding a composite patch onto the damaged area. Technique in the aeronautics field and its use is becoming increasingly widespread. This technique consists of sticking a composite patch to the damaged region using an appropriate adhesive. The choice of repair method depends on the nature of the material to be repaired, the damage and its use [6]. Currently, we are seeking to develop a composite patch capable of transferring as much as possible the stresses of the damaged zone by optimizing its mechanical properties, shape, dimensions and especially the fibre's nature and volume fraction, in order to provide great resistance to damaged structures taking into account all influencing parameters (mechanical load, humidity, temperature, *etc.*). Several researchers [7–9]

have studied the composite patches effectiveness and have carried out various optimization analyses regarding composite patch design capable of transferring maximum stress to the damaged area. Further experimental investigations have been carried out to improve the performance of composite repair joints by optimizing their geometric parameters [10, 11]. Mohammed *et al.* [6] investigated experimentally and numerically the influence of different shapes of composite-bonded patches. The finite element method was employed to evaluate how various parameters of the repair process affect the overall performance of structures repaired using composite patches [12].

Furthermore, a cracked aluminium plate was subjected to a nonlinear study employing a hybrid repair technique, which involves bonding a composite patch and drilling holes in opening mode. This investigation was carried out using finite element analysis methods [13].

On the other hand, the optimization of the adhesive layer takes precedence over that of the composite material due to its superior efficiency, given its role as the weakest link in the structure owing to its inferior mechanical properties compared to those of the plate and the composite. For this, the choice of an adhesive must be suitable for assembling the patch and the plate. This adhesive joint must be characterized for good use in repair [14]. For example, Dai *et al.* [15] investigated how adhesive properties and composite patch configurations influence the repair process of damaged aluminium alloy plates. Kwon *et al.* [16] analysed the adhesive layer to decrease the strain-energy release rate while repairing the cracked plate on one side.

Currently, the challenge for inspection engineers is the detection of different defects in the adhesive layer where non-destructive means of detection are not available [5, 9].

Indeed, the resistance of joints in assemblies is affected by the presence of bonding defects which will result in poor load transfer and consequently present a challenge for maintenance engineers to propose methods allowing detection and/or repair. Identify these defects using the means available to detect whether the bonding surface is healthy or presents defects [7, 11].

Current research aims to analyse the stress level within the adhesive joint to determine the high stress concentrations magnitude due to the presence of these geometric discontinuities.

For this purpose, it is essential to understand, through experimental and numerical analyses, the influence of the presence of defects in the adhesive layer on the global behaviour of the assembled structures. Recent researchers [8, 10, 13] have highlighted in their numerical analysis by finite elements the presence of defects in the adhesive and were able to analyse their effect on the global response of the assembled structures [17, 18] or in the case of repairing damaged plates with composite patches [19]. Kaddouri *et al.* [20] analysed numerically,

using finite-elements' analysis, the fracture behaviour of a plate with damage in the form of a bonding defect, which was then repaired by a bonded composite patch where they studied the defect position and size effect. The size and shape of the bonding defect on the adhesive joint behaviour and consequently on the global response of an assembly was addressed by Heiderpour *et al.* [21], where it was shown that, if the defect size is important, it can lead to rapid damage to the structure.

Our work is part of this context and aims to determine the SIF in a 2024-T3 aluminium plate repaired with an epoxy carbon composite patch. The size effects of a crack emanating from a circular notch in the plate as well as the defect position of the bonding relative to the adhesive surface were taken into consideration to analyse the stress intensity factor. The level of von Mises and shear stresses in relation to the defect position were presented in this study.

2. MATERIALS AND MODELS

The analysis involves a damaged structure repaired using a composite patch. This structure contains a 2024-T3 aluminium plate measuring $125\times250\times2$ mm^3. The plate has a circular notch in the centre with a diameter of 6 mm (Fig. 1, *a*). A crack emanating from the notch will be considered in the study of variable length a (Fig. 1, *a*).

A composite patch will be applied to the damaged area of this plate for repair (Fig. 1, *b*). The length, width and thickness of the composite part are respectively $h_p = 80$ mm, $W_p = 80$ mm and $t_p = 2$ mm. This patch is presented in the form of a laminate of 16 layers whose stacking sequence is as follows $[0]_{16}$. This patch is bonded using Adekit A140 type adhesive with a thickness of $t_a = 0.2$ mm. The shape of the patch was

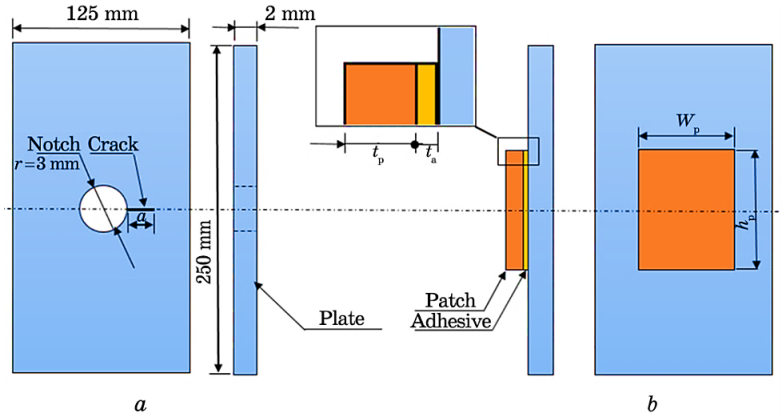

Fig. 1. Schematic representation of: aluminium 2024-T3 plate with crack emanating from notch (*a*), repaired plate with composite patch (*b*).

initially chosen square, as it is the most commonly used shape. The composite patch was simulated as unidirectional layer. This technique facilitates the incorporation of the real mechanical properties of each layer according to the fibres' directions, which is more realistic. The different mechanical properties necessary for the numerical model using the ABAQUS calculation code are derived from the tensile tests (Fig. 2) conducted on the different substrates [22].

From these curves, the different mechanical properties were presented in Table 1 and which are necessary for the numerical model.

The composite patch is based on high strength carbon fibre and an epoxy matrix. To introduce the patch mechanical properties, it was possible to experimentally determine the two different Young's moduli according to the longitudinal and transverse direction of the composite plate [23], but these two properties are not sufficient to successfully introduce the patch composite mechanical properties in the numerical analysis as being an orthotropic material, for this purpose both the carbon fibre and the epoxy matrix properties were introduced into the Cadec code designed especially for composites to determine the global properties of the patch based on the stacking sequence. The properties

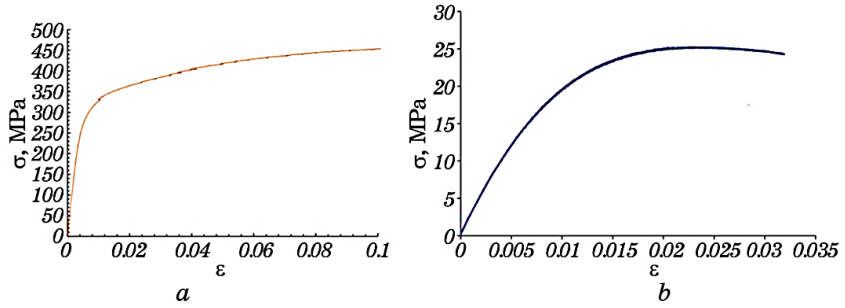

Fig. 2. Stress–strain curves for the 2024-T3 aluminium plate (*a*) and Adekit A140 adhesive (*b*).

TABLE 1. Aluminium plate and adhesive mechanical properties.

Parameter	Aluminium 2024-T3	Adhesive Adekit-A140
Young's modulus (E)	74400 MPa	2692 MPa
Tensile strength (R_m)	452 MPa	25
Yield strength ($R_{0.2}$)	230 MPa	14
Poisson's ratio (υ)	0.3	0.3
Shear modulus (G)	26000 MPa	1000
Elongation (A, %)	10	3.5

TABLE 2. Mechanical properties of the composite single layer oriented at zero degree.

Materials	$E1$ MPa	$E2$ MPa	$E3$ MPa	$\upsilon 12$	$\upsilon 13$	$\upsilon 23$	G12 MPa	G13 MPa	G23 MPa
Carbon/ Epoxy	128600	9766	9766	0.34	0.34	0.34	5252	4364	4364

determined by the Cadec code (essentially the two Young modules) were compared with those found experimentally where an error of 2.4% was found. The mechanical properties of the single-layer composite utilizing high strength carbon fibre are presented in Table 2.

3. ADHESIVE DEFECT

The strength of a composite patch repaired structure is significantly influenced by the adhesive's strength, which has the weakest mechanical properties compared to plate and composite. Indeed, the behaviour of the adhesive remains a complex subject without an exact solution. Indeed, adhesive failures can be influenced by operational and environmental factors during the application process such as cavities, air bubbles, cracks, impurities, *etc.* (Fig. 3). Additionally, poor surface preparation could be the primary cause of assembly failure.

The majority of studies in the realm of composite patch repair consider the adhesive to be a perfect third material where contact with the plate and with the patch is made over the entire surface of the damaged area, or in reality, it is necessary to consider the presence of defects in order to see their effect on the load transfer to the patch and consequent-

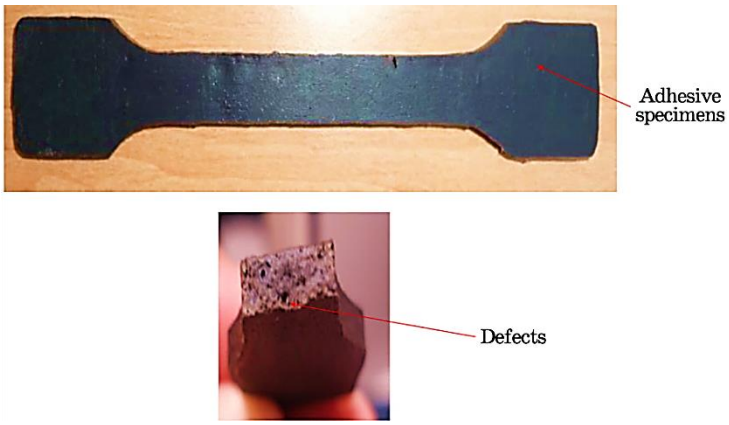

Fig. 3. Presence of defects during preparation.

ly on the repaired plate resistance. Our study is based in this context.

4. ANALYSIS METHODOLOGY

Our analysis (Fig. 4) concerns the plate, the composite patch and the adhesive, with consideration given to the defect position of the bonding (Fig. 3):

- for the plate, a comparison between repaired and non-repaired plates by determining the SIF at the crack tip;
- for the patch, determine peel stresses;
- for the adhesive, shear and von Mises stresses.

5. RESULTS

5.1. Mesh Selection

To achieve reliable results regarding to the damaged plate, the patch and the adhesive, it is necessary to choose an adequate mesh for the three substrates. The mesh was refined, particularly in the damaged area, and subsequently on the adhesive and the patch until stable stress values were attained, particularly at the notch level. Indeed, the von Mises stress variation analysis regarding the unrepaired plate mid-width (Fig. 5) show clearly that the mesh elements density has an influence in relation to the maximum value at the level of the notch where a variation of the value stress can reach 10%. However, far from the notch the density of mesh elements does not have a significant effect.

Likewise, the global plate response in terms of displacement load was analysed with changes in the mesh elements density (Fig. 6). The

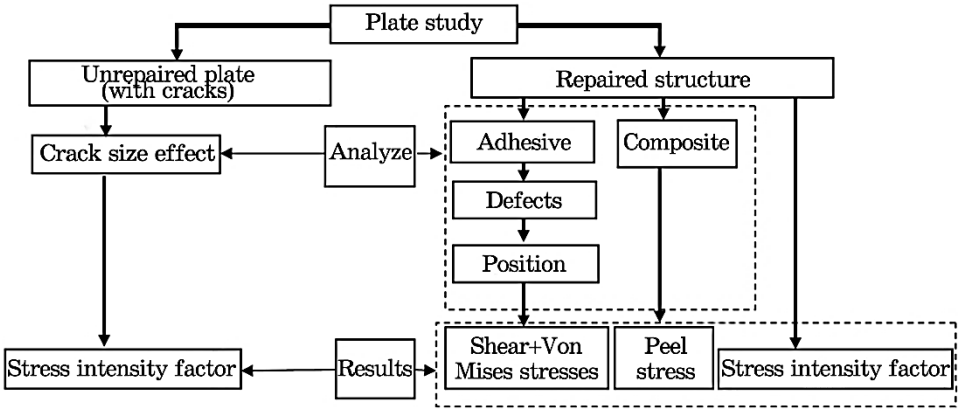

Fig. 4. Analysis methodology flowchart.

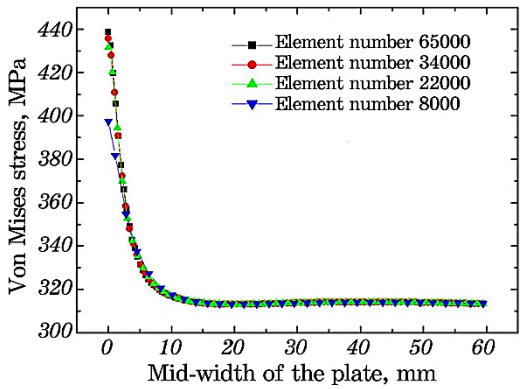

Fig. 5. Von Mises stress variation according to the unrepaired plate mid-width.

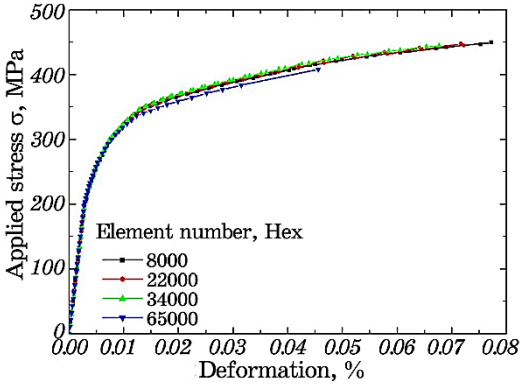

Fig. 6. Applied stress as a function of plate deformation for different numbers of mesh elements of type C3D8R.

obtained results show that the element density has no influence on the elastic part. On the other hand, mesh element density does have an influence on the plastic part, with a slight variation in stress and a deviation in plate deformation.

Finally, the type of mesh elements chosen is C3D8R, which is the most used for the mechanical analysis of structures. The density of mesh elements is varied in our study until it has a well-refined structure as shown in Fig. 4.

In the case of a notched plate with crack emanating from a notch, the damaged part of the plate has been refined more and more, as shown in Fig. 4, where the elements number varies as per to the crack size. At the notch level, refinement was done to a point where the circular shape appears clearly. Depending on the thickness of the structure, the

TABLE 3. The number of nodes and elements of unrepaired and repaired plate.

Crack length	Nodes/Elements	Semi-circular notch and crack	
		Unrepaired	Repaired
10 mm	Nodes	32022	50513
	Elements	20880	35280
30 mm	Nodes	39024	57515
	Elements	25426	39826

plate was meshed with 4 elements, while the adhesive layer has 2 elements, and the composite patch has 8 elements.

For the boundary conditions, a uniaxial loading was applied to the upper part of the plate with amplitude of $\sigma = 100$ MPa along the y-axis; the lower plate part is considered as embedded where the displacements and rotations are considered null.

5.2. Variation of K_I in Relation to Defect Position

To analyse how the presence of a bonding defect affects the fracture behaviour of the repaired structure, the presence of a square-shaped bonding defect with a surface area of 9 mm^2 was assumed at different locations on the adhesive surface (Fig. 8). A number of 14 defects positions were taken into account within the adhesive layer and given the symmetry we considered that the presence of the defect only on the upper part as shown in Fig. 8. For the analysis of the SIF at the crack tip, two cracks lengths (10 mm and 30 mm) emanating from the circular

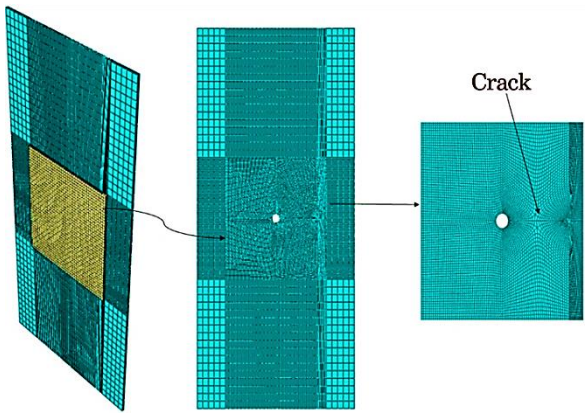

Fig. 7. Mesh details.

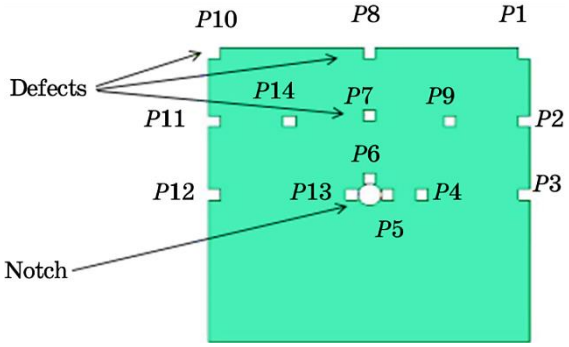

Fig. 8. Graphic representation of the different defect positions in the adhesive layer.

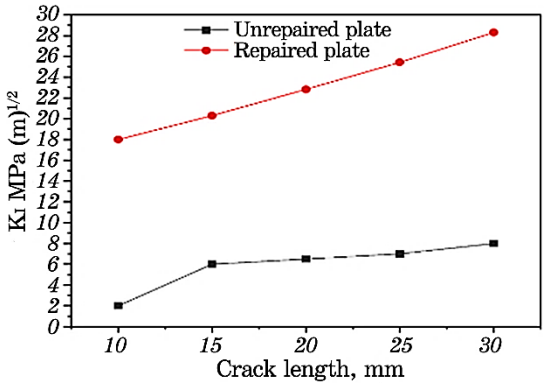

Fig. 9. The SIF variation as per of the crack length for a repaired and unrepaired plate.

notch were considered.

For each crack length, we varied the position of the defect according to the 14 possible cases. For defects 4 and 7, they are chosen so that their position will be in contact with the head of the crack. Defect 4 is located at the head of the 10 mm crack, while this same defect will be in position 7 for the size of the crack 30 mm.

5.2.1. Effect of the Repair Patch in the Absence of Adhesive Defect

In the first case, the analysis focused on evaluating the effect of the repair patch on the value of the SIF as a function of the crack length. The calculation of the SIF (K_I) as per of the crack length is presented in Fig. 9. It is clear in Fig. 9 that the composite patch absorbs the stresses in the damaged area via the adhesive used and minimizes the high

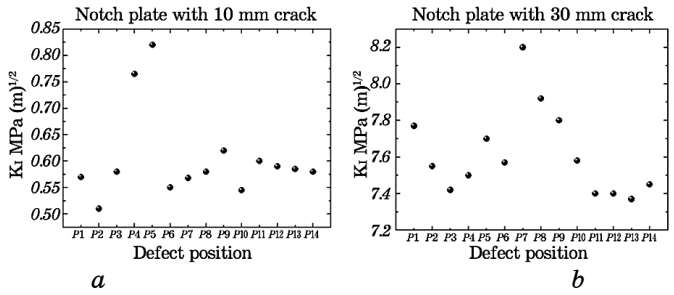

Fig. 10. SIF K_I variation as per of adhesive defect positions.

stress concentration at the crack and notch. The value of K_I at the crack tip augments with the increase in crack length and is reduced by almost 70% compared to the unrepaired plate.

5.2.2. Repaired Plate with Adhesive Defect

For this part of the study, the presence of defects at the 14 positions suggested in Fig. 5 was taken into account. We analysed the stress intensity factor value for two crack lengths ($a = 10$ mm and $a = 30$ mm). The first crack is located near the notch and far from the free edge of the patch, while the second crack is of significant length and situated near the defect, close to the free edge of the patch and the adhesive. The results of the SIF variation with respect to the different positions of the bonding defect are presented in Fig. 10.

For a crack length $a = 10$ mm, the SIF values are almost identical for the different defect positions. The lowest value is noted for defect position $P2$ and the highest value is for defect position $P5$ (Fig. 10, *a*). The stress intensity factor value for the case where the defect is in contact with the notch illustrates an increase of almost 60% compared to other positions. The defect position proximate to the notch and at the free edges ensures poor load transfer, leading to a high concentration of stresses.

For crack length (30 mm), the value of the SIF is very high compared to those of 10 mm of crack length. The lowest value is noted for defect position $P13$ and the highest value is for defect position $P7$. At these positions, the defect is at crack tip level, so load transfer to the patch is minimal, and the majority of stresses remain at crack level, resulting in a high SIF value in the plate (Fig. 10).

5.2.3. Shear Stress Level of the Adhesive (Notch Plate with 10 mm Crack) for Different Defect Positions

Analysing the variation of shear stress within the adhesive joint pro-

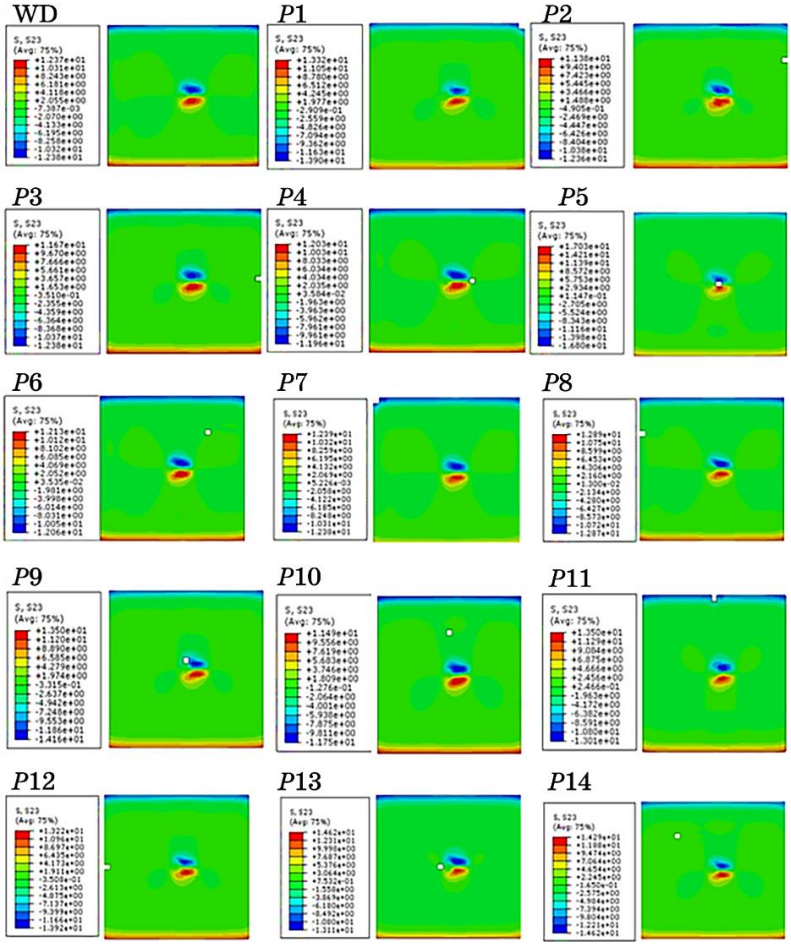

Fig. 11. Shear stress level in the adhesive joint as per of the position of the defect. (where WD: adhesive without defect, *P*: defect position in the adhesive).

vides a deeper understanding of the adhesive's role in load transfer and, consequently, in the failure behaviour of the repaired plate. For this analysis, the defect size of 9 mm^2, square in shape, was maintained at the 14 proposed positions (Fig. 11).

Figure 11 shows the analysis of the defect position effect on the level of shear stresses in the adhesive layer. The stress distribution clearly shows that the maximum shear stresses are concentrated at the two edges of the adhesive and in contact with the notch and the crack. In most cases of defect positions, the adhesive has a central inactive zone only a small area which is in contact with the notch and crack. Defects, which are far from areas of high stress concentration, do not disrupt the stress distribution in the adhesive layer. The shear stress value is generally

maximal in the presence of the bonding defect except in the case where the defect is situated far from areas of high concentration of stresses.

5.2.4. Von Mises Stress Levels in the Adhesive for Different Defect Positions with a 10 mm Crack in the Plate

The adhesive in a damaged and repaired structure is subjected to various stresses. Therefore, it is also important to analyse the equivalent stress to understand, if the adhesive is operating in the elastic or plastic domain.

Figure 12 illustrates the analysis of the effect of the bonding defect position on the value of the von Mises stress in the adhesive. It is ob-

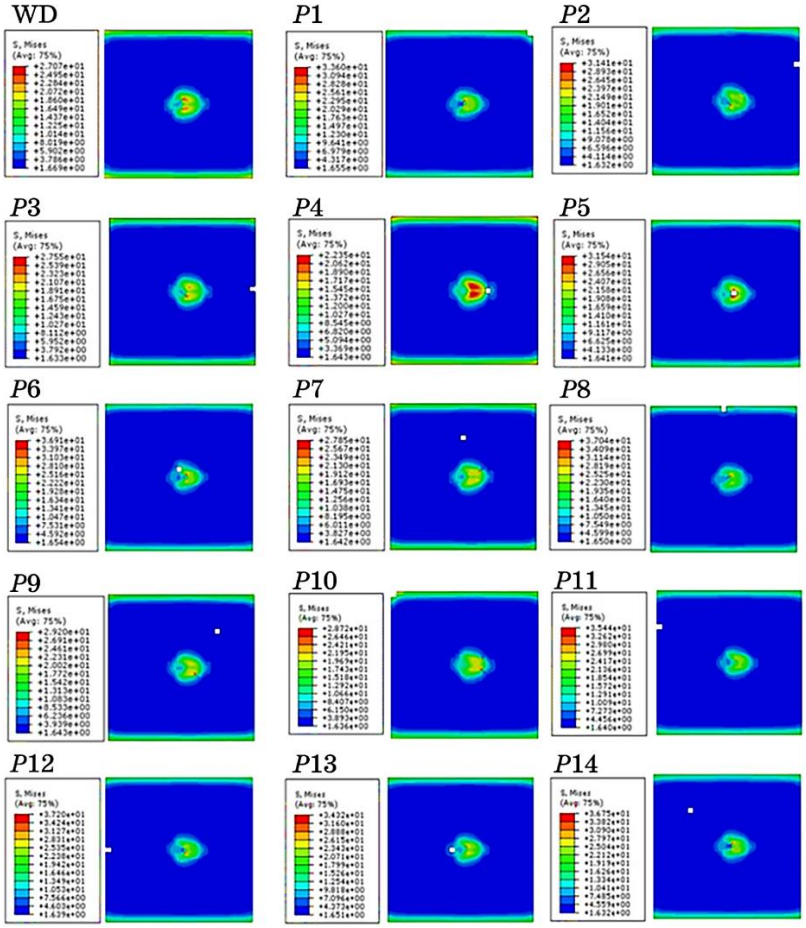

Fig. 12. Von Mises stress levels in the adhesive for different defect positions defect (notched plate with crack length $a = 10$ mm).

served that for this minimum crack length of 10 mm, the defect position significantly influences the von Mises stress value and, consequently, the adhesive joint strength.

The presence of a crack emanating from a notch causes a significant stress concentration within the plate, consequently increasing the load transfer to the patch significantly, inducing the adhesive to absorb a large amount of this load. Without a bonding defect, the von Mises stress exceeds its rupture limit by a significant margin, indicating that the adhesive under this loading condition may experience delamination.

The presence of the bonding defect increases the von Mises stress value, and this difference based on the defect position. It is observed that position 8 of the defect significantly affects the von Mises stress value, as this position is in contact with both the notch and the crack.

5.2.5. Maximum Von Mises Stress and Shear Stress Level in the Adhesive for Different Defect Positions with 10 mm Crack in the Plate

Based on the results presented in Figs. 11 and 12 regarding the stress level in the adhesive joint, an attempt was made to group the maximum von Mises values and shear stresses for each defect position. Figure 13 illustrates the maximum von Mises and shear stresses variation as per the defect position. It is observed that when the adhesive defect is located proximate the crack or notch, the stress concentration is higher and the shear stress value is therefore greater on the crack side and when the defect is situated on the free edge of the adhesive.

For this crack size, most defect positions in the adhesive layer result

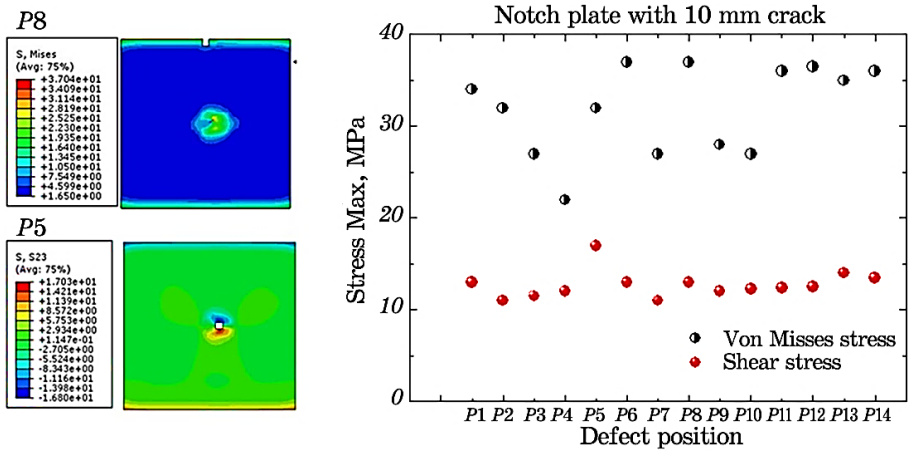

Fig. 13. Maximum von Mises stress and shear stress variation as per of bond defect position.

in a significant increase in the von Mises stress, which can greatly exceed the failure stress value of the adhesive.

5.2.6. Peel Stress Levels in the Composite Patch for Different Defect Positions with a 10 mm Crack in the Plate

Figure 14 shows the value of the peeling stress in the patch, which varies according to the defect position. These peeling stresses are concentrated at the level of contact with the crack, the notch and at the two edges of the patch. For this crack length and considering the significant the plate size, the composite patch is not subjected to significant

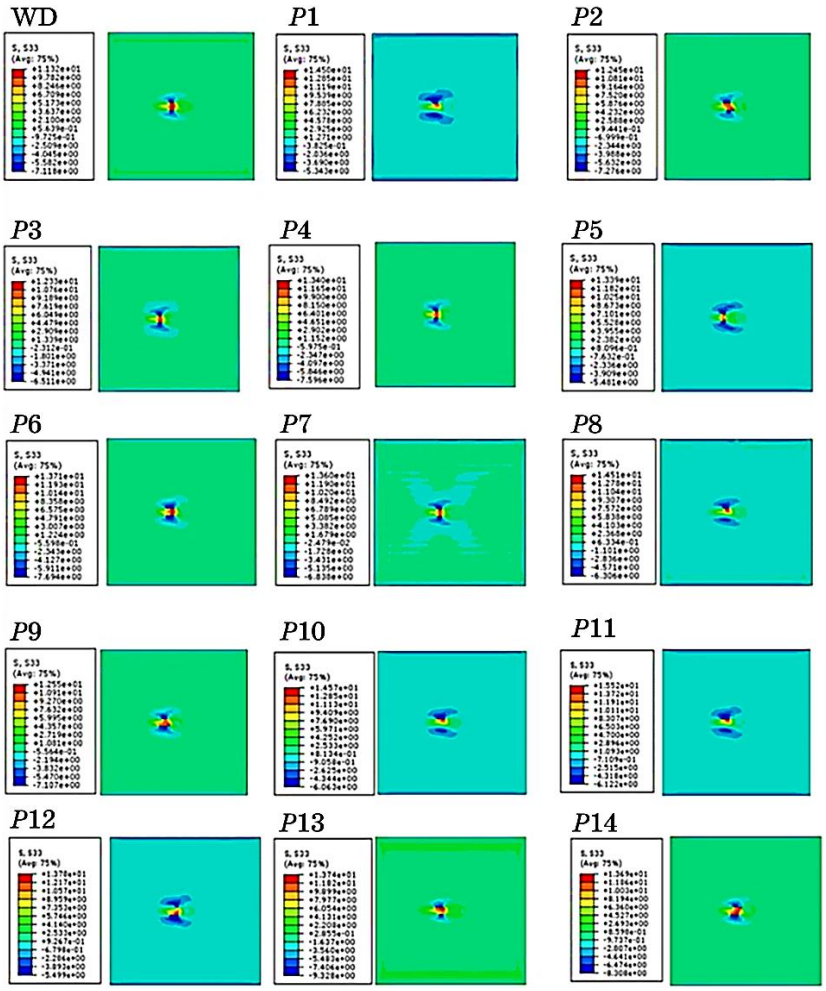

Fig. 14. Peeling stress level in the patch as per of defect position.

peel stress. The presence of a bonding defect only minimally disturbs the peel stress value in the patch, given its minimal size.

5.2.7. Shear Stress Levels in the Adhesive for Different Defect Positions with a 30 mm Crack in the Plate

As the crack size augment, the adhesive becomes highly stressed, and the shear stress value becomes higher. Figure 15 illustrates the shear stress level in the adhesive as per of defect position for a crack length of 30 mm, where it varies according to the position of the defect in the adhesive layer.

For this significant crack length, and considering the small defect

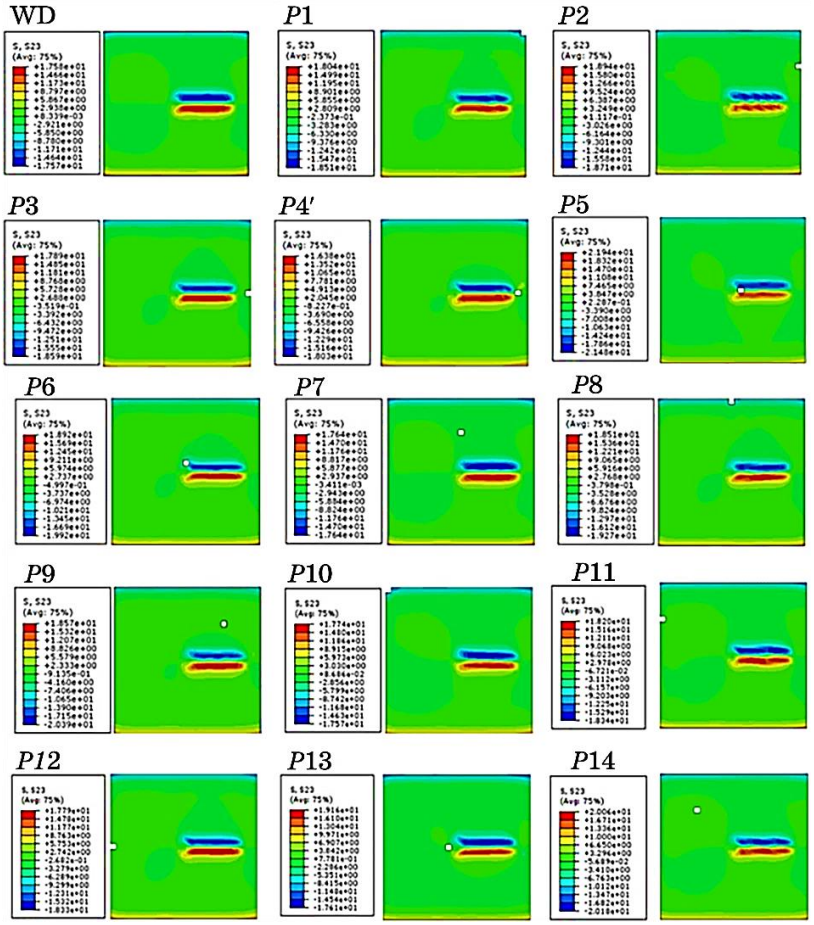

Fig. 15. Shear stress level in the adhesive for different defect positions (notched plate with crack length $a = 30$ mm).

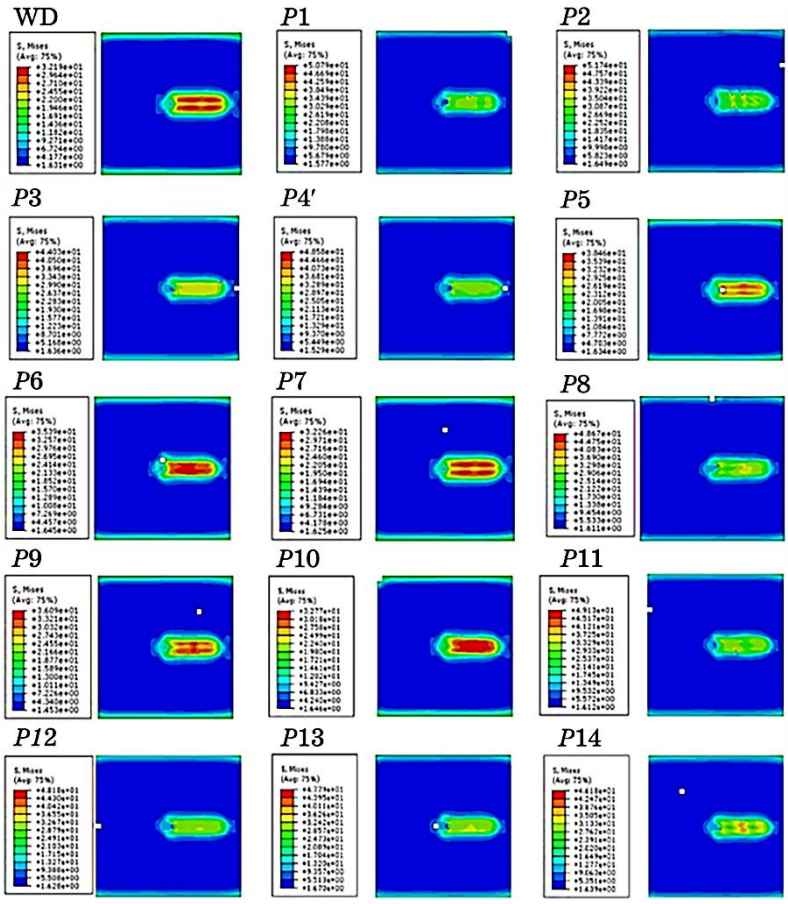

Fig. 16. Von Mises stresses level in the adhesive for different defect positions (crack emanating from notch of length $a = 30$ mm)

size, the majority of shear stresses are concentrated at the contact point with the crack. Even the adhesive edges are not heavily stressed.

5.2.8. Von Mises Stress Levels in the Adhesive for Different Defect Positions with a 30 mm Crack in the Plate

For this 30 mm crack length at plate level, Figure 16 shows the von Mises stress values are very high for any defect position. Relative to all defect positions, the von Mises stress value is well above the adhesive failure stress. Similarly, to shear stress, the von Mises stresses are concentrated in proximate to the crack.

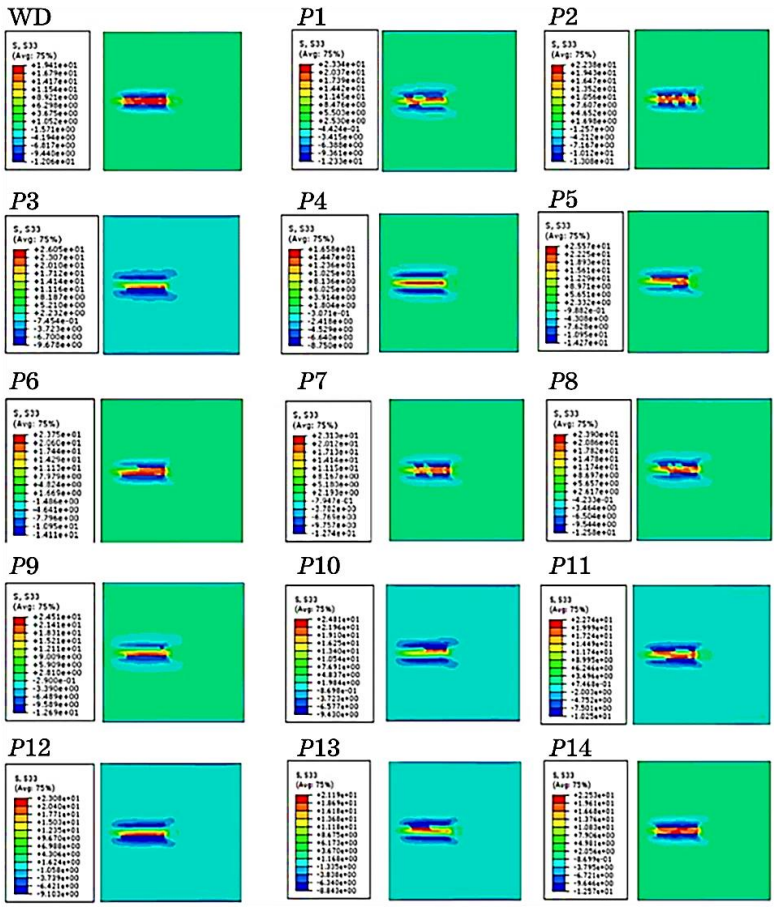

Fig. 17. Peeling stress level in the patch as per of defect positions.

5.2.9. Peel Stress Levels in the Patch for Different Defect Positions with a 30 mm Crack in the Plate

In Figure 17, it is evident that the peeling stress concentration is always in the zone where the crack is located in the plate.

5.2.10. Maximum Von Mises Stress and Shear Stress Variation as per of Bonding Defect Position for Different Defect Positions with 30 mm Crack in the Plate

Figure 18 shows the maximum von Mises stress and shear stress variation in the adhesive layer as a function of different bonding defect posi-

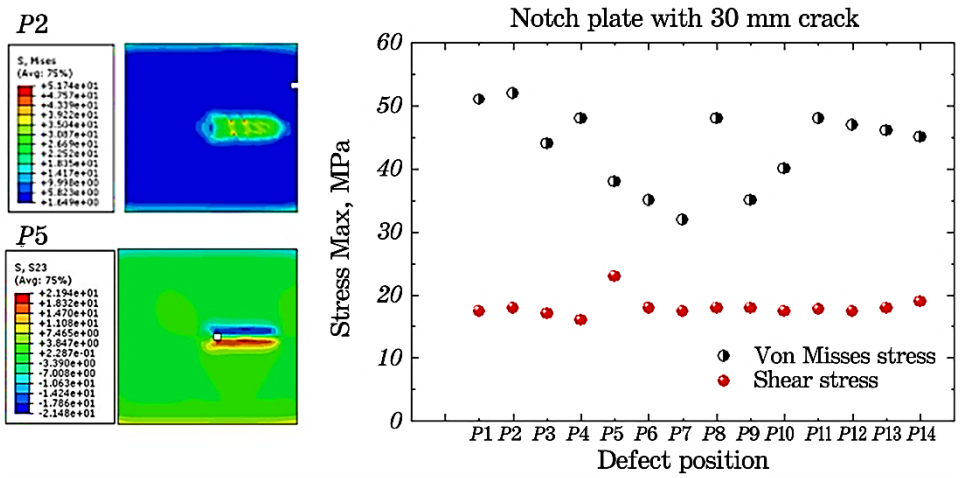

Fig. 18. Maximum von Mises and shear stresses' variation in the adhesive layer as per of bond defect position.

tions. The highest shear stress value is noted in the case where the defect is situated at position (*P*5). On the other hand, the zone of high von Mises stress concentration is noted at crack level, and increases if the defect is located approximately this zone and at the free edge level (*P*2).

6. CONCLUSION

The work presented in this study aims to investigate the impact of the presence of a square shape defect according to different positions in the adhesive layer. The study involves considering the determination of the stress intensity factor in the plate, the von Mises and shear stresses in the adhesive joint and peel stresses in the composite patch. Based on the presented results, the following conclusions can be drawn.

The presence of a crack emanating from a notch generates more stress concentration in the plate and therefore its repair by the composite patch bonding process is important.

Patch repair augment the plate strength and reduces the stress concentration at the notch and crack. The SIF value decreases by more than 50% for the case of the repaired plate.

The presence of a defect in the adhesive layer, even in minimum size, influences the value of the shear stress and stress placed in the adhesive joint and consequently on the load transfer to the patch so that the value of the intensity factor stress increases considerably depending on the position of the defect. For a minimum crack size, the presence of the defect slightly influences the stress values in the adhesive joint. However, if the crack size in the plate is large, the presence of the

bonding defect generates a considerable variation in the contents in the adhesive joint and consequently high SIF values.

If the defect in the adhesive layer occurs near the notch, the crack or at the free edge, there is a high shear and von stress value and poor load transfer to the patch.

REFERENCES

1. C. M. Machado, D. Silva, C. Vidal, B. Soares, and J. P. Teixeira, *The International Journal of Advanced Manufacturing Technology*, **112**: 3389 (2021).
2. P. Cheng, X.-J. Gong, S. Aivazzadeh, and X. Xiao, *Polym. Test.*, **34**: 146 (2014).
3. *Biographies* (Eds. A. A. Baker, L. R. F. Rose, and R. Jones). *Advances in the Bonded Composite Repair of Metallic Aircraft Structure* (Elsevier Science Ltd: 2002), p. v–vi.
4. G. Tsamasphyros, G. Kanderakis, D. Karalekas, D. Rapti, E. Gdoutos, D. Zacharopoulos, and Z. Marioli-Riga, *Fatigue Fract. Eng. Mater. Struct.*, **24**: 631 (2001).
5. S. Wang, Z. Xie, and X. Li, *Mech. Adv. Mater. Struct.*, **28**: 938 (2021).
6. S. Mohammadi, M. Yousefi, and M. Khazaei, *J. Reinf. Plast. Compos.*, **40**: 3 (2021).
7. K. Madani, S. C. Djebbar, N. Kaddouri, M. El Ajrami, and M. Belhouari, *Frattura ed Integrita Strutturale*, **16**: 304 (2022).
8. C. Duong, *Composites. Pt. A*, **40**: 1320 (2009).
9. X.-J. Gong, P. Cheng, S. Aivazzadeh, and X. Xiao, *Compos. Struct.*, **123**: 292 (2015).
10. T. Breitzman, E. Iarve, B. Cook, G. Schoeppner, and R. Lipton, *Composites. Pt. A*, **40**: 1921 (2009).
11. S. Coelho, P. Reis, J. Ferreira, and A. Pereira, *Compos. Struct.*, **168**: 259 (2017).
12. X. Liu, J. Wu, J. Xi, and Z. Yu, *Materials*, **12**: 1655 (2019).
13. W. N. Bouzitouna, W. Oudad, M. Belhamiani, D. E. Belhadri, and L. Zouambi, *Frattura ed Integrita Strutturale*, **14**: 256 (2020).
14. S. M. Khan and M. Essaheb, *Mater. Today: Proc.*, **4**: 9020 (2017).
15. J. Dai, P. Zhao, H. Su, and Y. Wang, *Materials*, **13**: 2740 (2020).
16. Y. Kwon and B. Hall, *Compos. Struct.*, **119**: 727 (2015).
17. M. Elhannani, K. Madani, E. Legrand, S. Touzain, and X. Feaugas, *Aerosp. Sci. Technol.*, **62**: 122 (2017).
18. A. Benchiha and K. Madani, *Structural Engineering and Mechanics*, **53**, Iss. 5: 1017 (2015).
19. A. Benchiha, K. Madani, S. Touzain, X. Feaugas, and M. Ratwani, *Steel Compos. Struct.*, **20**: 951 (2016).
20. N. Kaddouri, M. Kouider, M. B. Amine, and X. Feaugas, *Frattura ed Integrita Strutturale*, **13**: 331 (2019).
21. F. Heidarpour, M. Farahani, and P. Ghabezi, *Int. J. Adhes. Adhes.*, **80**: 128 (2018).
22. K. Madani, S. Touzain, X. Feaugas, S. Cohendouz, and M. Ratwani, *Comput. Mater. Sci.*, **48**: 83 (2010).